

HABILITATION A DIRIGER DES RECHERCHES

Préparée devant
L'Institut National des Sciences Appliquées de Lyon
et l'Université Claude Bernard Lyon 1

The role of length scales in material failure

Présentée par
Gergely MOLNAR
Docteur en 2014

Spécialité: MÉCANIQUE

Soutenue le 05/03/2025 devant la Commission d'examen :

Rapporteurs : Samuel FOREST - Mines Paris PSL CNRS 
David RODNEY - Université Claude Bernard Lyon 1
Jean-François MOLINARI - École Polytechnique Fédérale de Lausanne
Examinatrice : Laura DE LORENZIS - ETH Zürich
Examineurs : Nicolas MOËS - Université Catholique de Louvain 
Anthony GRAVOUIL - INSA Lyon

LABORATOIRE DE MÉCANIQUE DES CONTACTS ET DES STRUCTURES
LAMCoS UMR 5259 INSA-CNRS

Acknowledgments

I would like to express my deepest gratitude to several people who have been instrumental throughout this journey. First and foremost, I want to thank my major collaborators — Aurélien Doitrand, Anthony Gravouil, Etienne Barthel, and Julien Réthoré — for their inspiration and insightful discussions. My heartfelt appreciation goes to all my co-authors, particularly Marie-Christine Baietto, Nicolas Tardif, Rafael Estevez, Dominique Leguillon, Nawfal Blal, Christine Martinet, and János Török, from whom I have learned so much, both scientifically and personally. I am also grateful to my industrial partners, CEA, IRSN, and NEG, and particularly to Gustavo Alberto Rosales Sosa, for their invaluable support and collaboration throughout this journey.

I would also like to extend my sincere gratitude to the reviewers and jury members who took the time to evaluate my work. Their valuable feedback and constructive criticism have significantly contributed to the refinement and improvement of this research.

I am also deeply grateful to my Ph.D. students and postdoctoral researchers, especially Ethel Djeumen, Adrian Jacon, and Elie Eid, whose hard work and dedication were crucial in realizing this project.

I would like to thank CNRS Ingénierie and Section 9, my employers, for providing the framework that allowed me to dedicate my time to research. My colleagues at LaMCoS have been a constant source of support and friendship, and I am particularly thankful to Carine Bruscella and Isabelle Comby, whose efficiency and handling of administrative tasks made my work much smoother.

My postdoctoral supervisors — Anne Tanguy, Patrick Ganster, Guillaume Kermouche, Anthony Gravouil, Laurent Orgéas, David Rodney, and Julien Réthoré — deserve my sincere thanks for their confidence in me to complete the tasks at hand. A special acknowledgment goes to Imre Bojtár, my Ph.D. supervisor, for his teachings and for instilling in me a love for mechanics.

Lastly, I want to thank my family — Máté, Szingó, Gyapi, Semnoz and Folti – for their unwavering presence and love throughout this journey.

Lyon, 02/12/2024.

Preface

As a child, I was always fascinated by how computer games could create immersive, believable physical environments — remarkable even 25 years ago. I dreamt of developing my own software capable of describing the world, offering a deeper understanding of my surroundings. It turns out that game developers and movie animators [Bergou *et al.* 2010] use models similar to those employed by engineers; however, they empirically adjust material parameters to craft the magical worlds that captivated me as a child. This curiosity inspired me to pursue a career in engineering, with the goal of understanding the world around me and using that knowledge to create something new.

After graduating, while working at a structural engineering firm, I realized that no official European design standard existed for structural glazing. This observation sparked my decision to pursue academic research, leading me to dedicate my Ph.D. thesis to the failure of glass at the macroscopic scale. I was fortunate to participate in the COST Action TU0905, an initiative aimed at developing a pre-standard for these elegant structures [Feldmann *et al.* 2023].

My work on glass continued into my postdoctoral research, where I shifted focus from the continuum to the atomic scale, then to micron-scale experiments, and finally, back to macroscopic fracture. Around the early 2010s, the now-popular phase-field method was in its early stages. Recognizing its versatility in capturing various phenomena, including the yield criterion I developed at the atomic scale, I began exploring this technique. However, I quickly identified a significant gap in understanding concerning the regularization length — a crucial parameter that sets phase-field methods apart from other approaches to fracture modeling.

The manuscript begins with a brief literature review on length scales in fracture in chapter 1. Following this, chapter 2 examines the measurable effects of the regularization length. While the diffuse description was initially introduced to simplify numerical solutions, I argue in this thesis that it holds a necessary physical basis in many cases. This chapter covers tensile, in-plane, and antiplane shear fracture models, emphasizing the non-linear scaling effects introduced by the regularization length. The chapter concludes by underscoring the importance of regularization in dynamic fracture and demonstrating the technique’s flexibility in modeling other physical phenomena.

In chapter 3, I explore various length scales in silicate glasses, aiming to determine when a discrete material can be considered continuous. This section covers elasticity and plasticity — fields I studied during my postdoctoral research — before moving on to shear band formation and fracture, topics I continued to investigate as a CNRS researcher. The chapter concludes with a theory based on densification that unites these diverse phenomena.

Finally, chapter 4 delves into the mechanics of failure in architected materials. It demonstrates how Cosserat theory is essential for describing the behavior of lattice structures, a subject I explored during my years as a postdoc in Nantes. The chapter explains how to calculate the elastic Cosserat constants for arbitrary lattice structures, how to compute the toughness of these structures, and how to optimize macroscopic geometries to improve overall rigidity.

Looking ahead, the goal is to consolidate the knowledge I have gained over the past 10 years into a comprehensive, robust methodology for designing new, tailored mechanical metamaterials — a vision I first had as a teenager.

Motivation

My research focuses on understanding the mechanisms underlying material and structural failures, such as plasticity, damage, and fracture, across various spatial and temporal scales. The goal is to develop innovative material architectures that address the increasing demand for energy efficiency across industries, including aviation, transport, energy storage, or defense.

My research is structured around three primary axes: (i) modeling and experimental investigation of crack propagation at the macroscopic scale, (ii) multi-scale analysis of the microscopic mechanisms that contribute to the toughness and resilience of materials, and (iii) development of optimization techniques for designing fracture-resistant metamaterials.

From a young age, I have been fascinated by how simulations can predict real-world phenomena and enhance our understanding of reality. This passion has driven me to devote significant effort toward developing efficient and robust methods for 2D and 3D crack propagation simulations, utilizing hybrid discrete and finite element methods, as well as diffuse damage models such as the phase-field technique.

As a co-project leader, I have managed both academic projects (*e.g.*, ANR e-WARNINGS, ANR GaLAaD) and industrial collaborations (with IRSN, CEA), focusing on the implementation and refinement of the phase-field technique. This work has addressed complex topics such as early detection of acoustic waves emitted during fatigue fractures and oxygen-induced alloy embrittlement in nuclear safety. This development has led to the publication of a series of highly regarded articles [Molnár & Gravouil 2017, Molnár *et al.* 2020b, Molnár *et al.* 2022, Eid *et al.* 2023], with the first phase-field paper [Molnár & Gravouil 2017] receiving approximately 400 independent citations since its publication in 2017, including nearly 100 citations in 2023 alone.

This success has drawn numerous PhD students and postdoctoral researchers to LaMCoS, eager to explore the intricacies of this technique. Consequently, LaMCoS has emerged as a leading institution in the development and application of phase-field methods, recognized both nationally and internationally. For instance, Ethel Djeumen [Djeumen *et al.* 2022] extended the original phase-field code to account for oxidation and phase changes, providing insights into how materials become more brittle and lose ductility. In parallel, Baptiste Pillet applied the phase-field technique to model hyperelastic fracture in biological materials, while Adrien Jaccon implemented acceleration methods (both spatial and temporal) to model fatigue fracture.

Moreover, our research addresses not only applied problems but also fundamental physical principles, such as fracture toughness. Notably, our comparative studies of finite fracture mechanics and phase-field approaches [Molnár *et al.* 2020a, Molnár *et al.* 2024] have revealed that the diffusion length scale is not simply a numerical parameter but an enriching addition to traditional fracture mechanics frameworks. This finding provides a deeper understanding of fracture phenomena and reinforces the physical validity of diffuse damage models as robust, reality-based approaches.

In parallel, we have critically examined the fundamental concepts of the coupled criterion, including the initial dynamic jump. This line of inquiry has been explored in a series of articles since [Doitrand *et al.* 2022, Doitrand *et al.* 2023b, Doitrand *et al.* 2023a].

Engaging with multiple research communities enables me to bridge established knowledge across disciplines. For instance, my expertise in atomic-scale simulations has led to the development of a physically inspired failure criterion for silicate glasses [Molnár *et al.* 2016d, Molnár *et al.* 2016b, Molnár *et al.* 2017a], facilitating collaborations with experimental physicists (through projects like ANR GaLAaD and ANR RATES) and the international glass industry, including NEG Japan.

Atomic-scale simulations allow us to explore various compositions and conditions—such as high pressures, temperatures, and loading rates—that are challenging to replicate experimentally but are encountered in real-world material applications. These simulations provide insight into the fundamental mechanisms driving plasticity [Molnár *et al.* 2017a], fracture, and memory effects [Deschamps *et al.* 2022], paving the way for more refined material development.

The third research axis focuses on utilizing insights gained from both continuum and discrete scales to design materials with enhanced fracture resistance. I lead the development of robust optimization techniques [Molnár & Blal 2023] that leverage enriched mechanical descriptions (*e.g.*, Cosserat continuum) to create more resilient structural components.

For instance, in collaboration with Denis Machon and Nawfal Blal at Sherbrooke University in Canada, we are working on the design of silicon-based anodes for sustainable battery architectures [Saidi *et al.* 2023]. Silicon, a high-capacity and eco-friendly alternative to current technologies, faces challenges due to its fragility. Tom Guisard’s research centers on optimizing the nanoscale pore structure of batteries to enhance their durability during charging cycles—a critical factor currently limiting the widespread adoption of this technology. By refining the pore architecture, his work aims to develop materials that are more resistant to fracture, thereby extending battery lifespan and reliability. This optimization framework holds promise for a variety of applications, as it seeks to create material architectures that not only improve fracture resistance but also reduce structural weight, contributing to more efficient and robust energy storage solutions.

Contents

1	Nonlinear Scaling in Fracture:	
	A Brief Review	1
1.1	Context	2
1.2	State-of-the-art	4
1.3	Open questions	9
1.4	Thesis statement	10
2	Lengths in Fracture at the Continuum Scale	13
2.1	Motivation	14
2.2	Irwin's length in finite fracture mechanics	14
2.3	Phase-field regularization length scale	16
2.3.1	Phase-field principles	16
2.3.2	Energy decomposition	18
2.3.3	Damage irreversibility	19
2.3.4	Homogeneous solution	20
2.4	Length scales in fracture	21
2.4.1	Tensile opening in an infinite plane	22
2.4.2	In-plane shear fracture	25
2.4.3	Antiplane echelon cracking	26
2.4.4	Connection between the methods	29
2.5	Dynamic fracture	29
2.6	Oxidation induced fracture	31
2.7	Concluding remarks	33
3	Strength and Toughness of Silicate Glasses	35
3.1	Motivation	36
3.2	Elasticity	36
3.3	Densification	37
3.4	Ductile behavior	39
3.4.1	Yield criterion	40
3.4.2	Plastic events	42
3.4.3	Shear bands	44
3.5	Fracture	47
3.5.1	Regularization length	49
3.5.2	Surface free energy and toughness	50
3.5.3	Comparison between methods	51
3.6	Concluding remarks	52
4	Architected Materials	53
4.1	Motivation	54
4.2	Elasticity of beam lattices	54
4.2.1	Micro-macro kinetics	56
4.2.2	Periodic boundary conditions	57
4.2.3	Constitutive response	58
4.2.4	Cosserat length	58
4.3	Fracture in architected materials	58

4.3.1	Fracture in beam lattices	59
4.3.2	Equivalent fracture toughness	61
4.3.3	Experimental validation	64
4.4	Topology optimization of beam lattices	66
4.5	Concluding remarks	69
5	Conclusion and Perspectives	71
	Appendices	77
A	Methods	79
A.1	Coupled criterion	79
A.1.1	Working example	79
A.1.2	Error estimation	80
A.2	Atomic scale simulation	82
A.2.1	Potential function	82
A.2.2	Structural verification	83
A.2.3	Error estimation	84
A.3	Coarse-graining	85
A.3.1	Local quantities	85
A.3.2	Error estimation	86
B	Parallel projects	89
B.1	Elasto-plastic response of cellulose nanofibrils	90
B.2	Lithium penetration in a silicon-based batteries	91
B.3	Heat conductivity of bulk metallic glasses	91
C	Curriculum vitae	93
D	List of publication	99
	Bibliography	103

Nonlinear Scaling in Fracture: A Brief Review

The chapter offers a comprehensive overview of nonlinear scaling in fracture mechanics, focusing on the intricacies of material failure, with particular emphasis on brittle fracture. It explores the challenges of accurately predicting failure, which arise from factors such as atomic-scale interactions, material defects, and localized stress concentrations. Key theories are reviewed, including Griffith's energy-based criterion and Irwin's stress intensity factor, both of which are essential for understanding crack initiation and propagation. The discussion extends to nonlinear scaling laws and their relevance to size effects in materials, supported by experimental findings that provide critical insights. The chapter concludes by underscoring the importance of comprehending size-dependent failure mechanisms, particularly as new materials and cutting-edge manufacturing techniques push the boundaries of traditional fracture mechanics models.

Associated publications

- [Molnár *et al.* 2025] G. Molnár, A. Doitrand, R. Estevez and A. Gravouil, A Review of Characteristic Lengths in the Coupled Criterion Framework and Advanced Fracture Models, *Comptes Rendus. Mécanique*, 353, pp. 91-111, 2025.

Contents

1.1	Context	2
1.2	State-of-the-art	4
1.3	Open questions	9
1.4	Thesis statement	10

1.1 Context

In engineering materials, failure represents the critical state at which a material can no longer perform its intended function, making it a pivotal factor in design considerations. Engineers, scientists, and practitioners have long sought to understand the root causes of material failure to prevent it. However, due to the complexity of failure mechanisms, significant safety factors are incorporated into design practices. These safety margins are essential not only because applied loads are often statistically estimated, but also because the precise resistance of materials remains uncertain.

Understanding material failure is crucial for both ecological and economic reasons. Overestimating the size of structural elements leads to excessive resource consumption, waste, and environmental impact. In contrast, using lightweight, durable materials can significantly reduce energy use and emissions, especially in sectors like transportation. Economically, weight reduction lowers costs related to fuel, materials, and maintenance. A deeper understanding of material failure would enable more efficient material use, extend product lifespans, and minimize waste, ultimately benefiting both the environment and the economy.

Among the various modes of failure, brittle failure is one of the most widely recognized. It occurs when a material suddenly loses its structural integrity and can no longer bear the applied load. Brittle failure is typically characterized by a rapid loss of tensile strength and rigidity, leading to fracture without significant prior deformation.

Another key mode of failure is ductile failure, commonly seen in metallic materials. In this case, the material retains its elastic stiffness but reaches a point where it can no longer increase its load-bearing capacity, resulting in yielding under stress. Interestingly, even materials traditionally considered brittle, such as glass, can exhibit microscopic plasticity under certain conditions.

Beyond brittle and ductile failures, other modes also play crucial roles in material performance. Buckling occurs under compressive loads, causing a structural component to lose stability. Creep failure, on the other hand, happens when a material undergoes progressive deformation over time under constant stress. Fatigue failure is the result of repeated local deformations, which gradually weaken the material and reduce its resistance.

It is also essential to recognize that failure often results from a combination of these modes, underscoring the complex behavior of engineering materials under varying conditions.

One of the simplest ways to conceptualize material failure is by visualizing a pe-

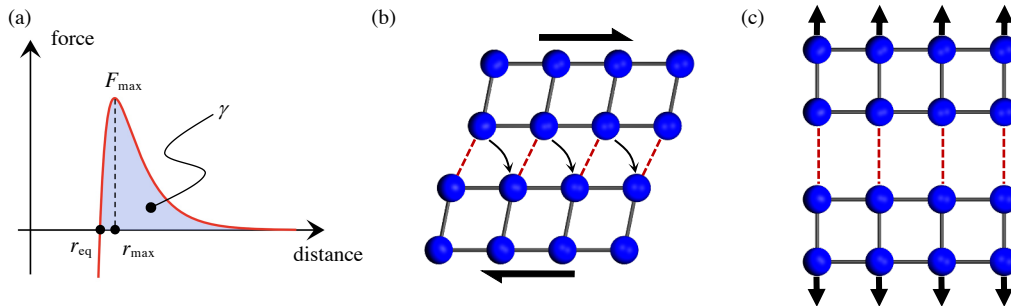


Figure 1.1: (a) Interatomic force as a function of distance between atoms. With blue, the bonding energy is highlighted. (b) Simple shear deformation showing an elementary shear band. (c) Failure under tensile loading. Red dashed lines show "broken" bonds.

riodic atomic lattice subjected to either simple shear deformation or tensile extension. A fundamental principle governing this behavior is the interaction between atoms [Janssen *et al.* 2004], where the force between atomic particles is a function of their separation distance, as illustrated in Fig. 1.1a. The figure presents a simplified atomic interaction function: at the equilibrium distance, r_{eq} , the force between atoms is zero, indicating a stable configuration. When atoms are either pulled apart or compressed, tensile or compressive forces emerge. The slope of the force-distance curve defines the material's elementary stiffness. As atoms are separated further, the force increases to a peak value, representing the elementary strength of the atomic bond. This gradual change in force was first theorized by van der Waals [der Waals 1873], for which he was awarded the Nobel Prize in 1910. This maximum force can provide an estimate of the macroscopic strength of a perfect crystalline material. Unlike in granular materials, atomic bonds can "break" and reform without an energy penalty, but each bond breakage releases energy, which is dissipated as heat, sound, or even light.

As depicted in Fig. 1.1b, in a perfect crystalline structure subjected to increasing shear deformation, atomic bonds break when a certain threshold is surpassed. Depending on the type of bond (covalent, ionic, metallic, etc.), further deformation may allow the upper layer of atoms to find new neighbors – provided they do not exceed the maximum separation distance, r_{max} – and form new bonds. This enables the structure to retain some resistance to further deformation, with only a portion of the stored elastic energy being released. The maximum shear stress observed in this process is commonly referred to as the yield strength. In reality, however, this behavior is complicated by elementary defects known as dislocations, which introduce additional complexities into the material's response.

In contrast, under tensile stress, as shown in Fig. 1.1c, when the distance between atoms exceeds r_{max} , bonds begin to break, and the atoms fail to find new partners to form bonds. As a result, all the stored elastic energy in the material is released, and the tensile stress within the remaining structure gradually drops to zero, leading to brittle failure.

While this idealized periodic lattice offers useful insights, it is a significant simplification, as real materials rarely exhibit perfectly homogeneous or flawless microstructures. The interaction of different atomic species, their arrangements, and the presence of defects within these networks play critical roles in determining the macroscopic strength and behavior of the material.

Defects affect the response of structures not only at the atomic-scale but also at the macroscopic level. To illustrate the effect of macroscopic defects, consider a simple engi-

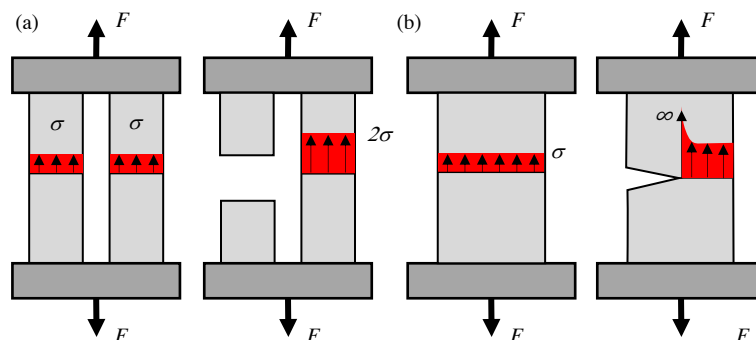


Figure 1.2: Illustration of the fracture mechanics challenge: (a) Stress redistribution in a homogeneous material; (b) Stress concentration near a defect.

neering example: a column (shown in Fig. 1.2) stretched between two infinitely rigid grips. If the structure consists of two identical elements and one side is cut, the tensile stress in the remaining element doubles. However, if the structure is a single continuous element and is cut halfway through, the resulting stress peak becomes theoretically infinite. Despite the loaded cross-sections being of the same size in both cases, the mechanical response is dramatically different. In the latter scenario, these incisions are referred to as cracks. The stress singularity associated with cracks renders traditional mechanics inadequate for solving this problem. While comparing applied stresses to material strength can predict failure in a perfect structure, a different approach is necessary in the presence of defects.

The first viable solution to address such issues was proposed by Griffith [Griffith 1921], who replaced the stress-based criterion with an energetic approach, suggesting that the problem could be analyzed through stability considerations. Griffith proposed that the formation of a crack surface requires a specific amount of elastic energy to be released from the material, conceptualizing the area under the force-distance curve (as shown in Fig. 1.1a) as a material parameter. This led to the introduction of the energy release rate, which represents the energy difference between two singular stress states, remaining non-singular during crack propagation. Griffith defined the critical energy release rate, also known as fracture toughness, as the key metric for predicting crack growth.

The advantage of this approach is its ability to handle sharp defects without relying on singular stress comparisons. While traditional stress-based methods are sufficient to determine the structural integrity of a defect-free material, Griffith's energy-based approach is essential when cracks or defects are present. Over time, this model has proven effective in predicting crack propagation for materials with sufficiently large defects.

However, most engineering structures are not designed with pre-existing macroscopic cracks. In materials without such defects, Griffith's theory would suggest an unrealistic infinite load-bearing capacity. As a result, engineering design standards still rely predominantly on stress-based criteria.

Nonetheless, as early as 1958, experiments shown by Irwin [Irwin 1958] demonstrated that when the sample size is small, the material behaves as the stress-based criterion predicts. Yet, as the sample size increases or a measurable crack appears, Griffith's theory becomes applicable. Between these two extremes lies a nonlinear region, characterized by a specific length scale where both methods fail to provide accurate predictions – a region where most manufacturing defects exist.

Over the last 10 years of my work I focused on techniques and examples where nonlinear effects play a significant role, offering guidelines for tackling this complex issue. In this manuscript, I suggest techniques how this critical length scale can be estimated in real-world materials and propose methods to exploit this scale effectively in the design of new architected materials.

1.2 State-of-the-art

The first empirical observations of the size effect date back to Leonardo da Vinci [da Vinci 1504, Williams 1957], who noticed that shorter cable segments were stronger than longer ones, though he did not provide a practical explanation for this phenomenon. It was Galileo Galilei who later formulated the correct scaling laws for materials under tension and bending [Galilei 1638], emphasizing how size effects limit the structural integrity of large natural and man-made structures. Centuries later, as iron and steel became more widely used, concerns about brittle fracture grew, prompting early material failure testing [Kirkaldy 1864]. Around the same time, Mariotte [Mariotte 1886], through extensive ex-

perimentation, suggested that the size effect observed by da Vinci was likely due to internal faults, concluding that larger structural elements have a higher probability of containing weak spots, thus reducing their overall strength.

Despite these early insights, little progress was made on the topic until Griffith's groundbreaking work in 1921 [Griffith 1921]. Griffith shifted the focus from a stress-based comparison to an energetic criterion, demonstrating that the resistance of glass could increase tenfold by considering the energy release rate. His work laid the foundation for a new branch of mechanics, essentially providing a theoretical explanation for Galilei's and Mariotte's experimental results.

At the same time, alongside the development of fracture mechanics, researchers began exploring statistical theories to explain the power-law scaling observed in experiments. Peirce [Peirce 1926] developed the weakest-link model for chains, drawing on the extreme value statistics introduced by Tippett [Tippett 1925]. The statistical treatment of size effects reached a milestone with Weibull [Weibull 1939b, Weibull 1939a], who introduced the Weibull distribution to model the probability of material failure based on the tail of low-strength values. This distribution became fundamental in describing the power-law relationship between material strength and failure probability, particularly in materials with microscopic flaws or microcracks [Freudenthal 1946]. It has since been applied to various materials, such as metals and ceramics [Kittl & Díaz 1990], addressing phenomena like fatigue embrittlement, cleavage toughness, and fracture toughness variability [Evans 1978, Beremin *et al.* 1983, Lei *et al.* 1998]. While this statistical approach is widely accepted and used, in this manuscript, we will focus on a physically based deterministic approach. Nevertheless, the combination of both statistical and deterministic methods can be effectively utilized when necessary, providing a more comprehensive understanding of material failure across different scales.

The non-linear scaling law, first documented by Irwin in the 1950s [Irwin 1958], was initially overlooked or considered a statistical anomaly. Motivated by the observation that large concrete structures (such as dams, reactor containments, and bridges) behave differently from small laboratory specimens, Bažant conducted a series of experiments [Bažant 1984]. He eventually published his theoretical explanation in 1986, describing a non-linear scaling law in fracture mechanics [Bažant *et al.* 1986]. Bažant emphasized the need for non-linear analysis to account for the significant size effects observed in various engineering structures. This phenomenon has since become critical for the design of large-scale composite structures such as ship hulls, bulkheads, decks, masts, and structural fuselage panels, as well as in fields like geotechnical and arctic engineering. For example, evaluating fault slip stability in the Earth's crust involves scale transitions that span multiple orders of magnitude.

Bažant [Bažant 1999] further showed that fracture resistance in many materials deviates from the power-law predictions of linear elastic fracture mechanics, especially when the initial flaw size is smaller than a critical value. In such cases, stress-based criteria should be applied. The existence of this critical length scale has since been demonstrated in various materials, including ceramics [Kimoto *et al.* 1985, Usami *et al.* 1986, Leguillon *et al.* 2018, Martin *et al.* 2018], polymers [Doitrand & Sapora 2020, Sapora *et al.* 2018], silica glass [Luo *et al.* 2016], silicon carbide [Bažant & Kazemi 1990], fiber composite laminates [Bažant *et al.* 1996], wood [Aicher 2010], concrete, rock [Shah & Swartz 1987], and even sea ice [Dempsey *et al.* 1999]. However, experimental observation of this critical scale is challenging, as it requires testing specimens across multiple size ranges.

The transition length scale is often compared to the size of the fracture process zone (FPZ), a region around a crack tip where complex, nonlinear deformation occurs. The FPZ, characterized by a transition from elastic to inelastic behavior, plays a critical role

in fracture mechanics. In the 1950s, Irwin [Irwin 1948] and Orowan [Orowan 1949] used X-ray measurements to demonstrate that even in brittle materials, there is evidence of regularization along crack surfaces. They independently concluded that the true critical energy release rate should be several orders of magnitude larger than Griffith's original proposal. Later, Barenblatt [Barenblatt 1959] and Dugdale [Dugdale 1960] theorized that material near the crack yields, and this local cohesive traction limits the otherwise infinite stress peak.

Since then, numerous experimental techniques [Labuz *et al.* 1983, Chengyong *et al.* 1990, Denarie *et al.* 2001, Du *et al.* 1990, Guo *et al.* 1993, Yu & Kobayashi 1994, Zang *et al.* 2000, Otsuka & Date 2000, Zietlow & Labuz 1998, Labuz *et al.* 1987, Cotterell 2002] have been developed to measure the size and shape [Neimitz & Aifantis 1987] of the FPZ in brittle materials. These studies commonly assume that the FPZ is a damaged region around the crack tip linked to irreversible microstructural changes. The FPZ has been observed in materials such as concrete [Cedolin *et al.* 1983], granite [Labuz *et al.* 1983], natural faults [Vermilye & Scholz 1998], wood [Yu *et al.* 2019], model materials [Haidar *et al.* 2005], and silica glass [Rountree *et al.* 2010]. A comprehensive review of the FPZ can be found in the thesis of Brooks [Brooks 2013]. Today, digital image correlation [Réthoré & Estevez 2013] is the primary technique used to quantify the FPZ, although other methods exist for transparent materials like polycarbonate [Cortet *et al.* 2005] or for X-ray measurement in concrete [Otsuka & Date 2000].

While the non-linear scaling law is widely accepted, its underlying cause remains a topic of active debate. This is particularly important given the rise of advanced manufacturing techniques that allow the creation of architected materials with structural elements smaller than the critical length scale of bulk materials, resulting in exceptionally strong overall responses [Schaedler *et al.* 2011].

The first estimation of the nonlinear transition length scale was introduced by Irwin [Irwin 1958], who proposed a correlation between the critical energy release rate, Young's modulus, and tensile strength. Although this was a rudimentary estimation, it captured the essence of the nonlinear problem and provided a lower bound for the applicability of fracture mechanics. This work also introduced a new metric for toughness: the stress intensity factor [Irwin 1957].

Later, Taylor [Taylor 2008] revisited the concept of a critical length scale with the development of the Theory of Critical Distances (TCD), a method designed to predict failure in materials with stress concentrators like notches or cracks. TCD introduced a characteristic distance over which the stress field around a defect influences the material's resistance to fracture. This approach has proven useful for predicting material failure when well-defined stress concentrators are present and has been widely adopted to understand fracture and fatigue behavior in components with complex geometries.

However, the critical distance in TCD was found to be more of a geometric parameter than a true material constant. Additionally, TCD does not effectively account for nonlinear effects in cases where small cracks or defects are present, especially when the sample size is smaller than the critical distance itself.

At this stage, only Bažant's nonlinear scaling function had successfully matched experimental observations, but it required the calibration of several parameters through expensive and complex testing. A significant advancement came with the introduction of Finite Fracture Mechanics (FFM) by Leguillon [Leguillon 2002], which was inspired by Barenblatt's cohesive zone model [Barenblatt 1962].

FFM introduced a dual criterion for predicting crack initiation, combining both energy- and stress-based criteria. According to this theory, both the energy required for crack

growth and the stress at the crack tip must be satisfied to predict failure; neither criterion alone is sufficient. By meeting both conditions, a characteristic length scale emerges that depends on geometry and loading conditions, aligning well with experimental data.

The strength of FFM lies in its reliance on two well-established material parameters: fracture toughness (or the critical energy release rate) and tensile strength. This approach has been successfully applied to a broad range of problems, including the failure of ceramics [Martin *et al.* 2018, Leguillon *et al.* 2018], composites [Martin *et al.* 2012, Doitrand *et al.* 2017, García *et al.* 2018], notched specimens [Leguillon *et al.* 2007, Cornetti *et al.* 2013], and bi-material interfaces [Mantič 2009, Stein *et al.* 2015, Doitrand & Leguillon 2018c]. A comprehensive review of these applications can be found in Ref. [Weißgraber *et al.* 2016].

Recent developments have extended the theory to three-dimensional cases [García *et al.* 2016, Yosibash & Mittelman 2016, Doitrand & Leguillon 2018a, Doitrand & Leguillon 2018d], nonlinear materials [Leguillon & Yosibash 2017, Rosendahl *et al.* 2019, Li *et al.* 2019, Doitrand & Sabora 2020], 3D-printed polymers [Xu & Leguillon. 2019], fatigue limit predictions [Liu *et al.* 2020], and integration with peridynamics [Zhang & Qiao 2018], further enhancing the utility and accuracy of FFM in predicting fracture behavior across various materials and conditions.

While theoretical models provide a solid foundation for understanding crack initiation and propagation, applying them to real-world problems often requires numerical methods to address the complexities of material behavior, geometries, and loading conditions. At the smallest scales currently accessible through computational resources, molecular dynamics (MD) simulations [Rountree *et al.* 2010] offer valuable insights into crack propagation by using interatomic potentials and detailed atomic structures, thus avoiding the need for additional numerical parameters. Recent studies [Aghababaei *et al.* 2016, Aghababaei *et al.* 2017] have advanced our understanding of finite-size effects, revealing a critical transition in wear mechanisms at the atomic scale. Specifically, atomistic simulations show that when asperity contact junctions surpass a critical size, fracture-induced debris formation occurs, while smaller junctions result in a gradual smoothing through plastic deformation. This non-linear behavior highlights the crucial role of length scale in determining whether fracture or plastic smoothing dominates. However, a key limitation of MD simulations remains their confinement to small simulation box sizes, which are often much smaller than the physical distances required to fully separate crack surfaces, leading to finite-size effects that can compromise the result's accuracy.

Discrete element methods (DEM) [Fakhimi & Wan 2016] provide an alternative by modeling interactions between macroscopic particles through empirical functions, capturing microscopic structural changes. Similarly, meshfree methods such as smoothed-particle hydrodynamics [Caleyron *et al.* 2012] and peridynamics [Bobaru *et al.* 2016] offer an internal length scale parameter that introduces spatial and temporal regularization, much like phase-field methods.

At the continuum scale, the extended finite element method (X-FEM) builds on the stress intensity factor by incorporating a unified fracture toughness. This approach uses a series of corrective functions to account for stress regularization [Jan 2016]. In cohesive zone models (CZM), the crack tip extends into the process zone, where cohesive tractions resist crack opening. Surface traction is modeled as a function of the opening displacement, simulating the failure process in three stages: (i) initiation at a critical traction value, (ii) thickening, and (iii) local crack nucleation at a critical opening, with the latter introducing an intrinsic length scale. This approach, pioneered by Barenblatt [Barenblatt 1959, Barenblatt 1962] and [Dugdale 1960], was first incorporated into finite

element analysis by Hillerborg [Hillerborg *et al.* 1976] in civil engineering and later revisited by Needleman [Needleman 1987, Needleman 1990] using micromechanics principles.

One limitation of CZM is the need for a predefined crack path, requiring assumptions about crack trajectories (*e.g.*, normal to maximum principal stress directions or along grain boundaries). While advancements allow cohesive elements to be inserted dynamically during simulations [Camacho & Ortiz 1996, Ortiz & Pandolfi 1999, Remmers *et al.* 2003], the finite element mesh can still restrict the emerging crack path. Nevertheless, CZM was the first method to explicitly consider the size of the FPZ, making it possible to capture both stable and unstable crack growth realistically.

Smearred approaches, such as the thick level set (TLS) [Moës *et al.* 2011] and gradient damage models [Bourdin *et al.* 2000, Miehe *et al.* 2010a], offer potential alternatives. These models diffuse the crack into the solid volume using an internal length scale. In the TLS method, fracture topology is determined based on geometrical considerations, whereas in the phase-field approach, an additional gradient flow equation is solved.

Both the TLS and phase-field methods are rooted in the theory of Continuum Damage Mechanics (CDM) [Lemaitre 1984]. The theory provides a framework for understanding how micro-level damage, such as micro-cracks or voids, affects the macroscopic mechanical properties of materials. The field was established by Kachanov [Kachanov 1958], who introduced the concept of a damage variable to quantify the degradation of materials based on the density and distribution of micro-defects. The core of CDM involves constitutive models that describe the stress-strain relationship in damaged materials and include damage evolution equations derived from thermodynamic principles to predict the progression of micro-defects to macroscopic failure. While classical CDM effectively models uniform damage, it struggles with discontinuities like cracks, leading to the development of gradient damage models [Pijaudier-Cabot & Bažant 1987, Benallal *et al.* 1991, de Borst *et al.* 1996, Peerlings *et al.* 1996, Peerlings *et al.* 1998]. These models introduce a regularization term that smooths the damage over a finite region, enhancing the ability to simulate complex failure phenomena such as brittle fracture [de Borst 2002] and localized damage [Geers *et al.* 1998]. The community has even suggested techniques to measure the characteristic length of these nonlocal continuum [Bažant & Pijaudier-Cabot 1989].

The phase-field approach was originally based on the criterion proposed by Griffith [Griffith 1921, Griffith 1924]. This stationary approach was reformulated by Francfort & Marigo [Francfort & Marigo 1998], who updated Griffith's local energy criterion into a global energy minimization framework. Despite the elegance of this reformulation, a challenge remained in modeling fracture as a surface domain within a volume. Bourdin [Bourdin *et al.* 2000], inspired by the Mumford & Shah [Mumford & Shah 1989] functional, solved this issue by introducing the crack density function, building on the Ambrosio & Tortorelli [Ambrosio & Tortorelli 1990] elliptic regularization function. Essentially, the crack density function was introduced by Miehe *et al.* [Miehe *et al.* 2010a] with an internal length scale (l_c), describing the transition towards the limiting case represented by a Griffith-like fracture. Since its introduction, the phase-field method has gained significant popularity, and numerous extensions have been proposed.

These advances in computational methods provide robust tools for simulating fracture behavior across scales, integrating theoretical insights with numerical simulations to address increasingly complex material and structural challenges. For a detailed comparison between numerical methods and mechanical theories, the interested reader is referred to the recent review paper [Molnár *et al.* 2025].

1.3 Open questions

Despite the significant advances in fracture mechanics over the past century, several fundamental questions remain unresolved. As the field continues to evolve, understanding crack initiation and propagation across multiple scales – from the atomic to the macroscopic level – presents ongoing challenges. The recent development of architected mechanical metamaterials, which exhibit unique fracture behaviors due to their tailored microstructures, adds further complexity to this domain. Below are some of the key open questions in failure mechanics, focusing on macro-scale fracture criteria, atomic-scale origins of failure, and the challenges posed by architected materials.

Toughness or strength? One of the central challenges in macro-scale fracture mechanics is determining when to apply stress-based versus toughness-based criteria for predicting material failure [Leguillon 2002]. Stress-based criteria are generally used for small flaws or defects, where failure occurs at a critical stress level. In contrast, toughness-based criteria are used for larger defects or cracks, where energy required for crack propagation becomes the dominant factor. However, the transition between these regimes is poorly understood, especially for complex loading conditions and materials with heterogeneous properties. Further research is needed to define the critical conditions or dimensions where one criterion becomes more appropriate than the other.

Does a unique regularization length exist? A fundamental question at the macro-scale involves the regularization length (l_c) in phase-field models of fracture. This parameter is introduced to facilitate variational techniques in solving complex fracture problems [Bourdin *et al.* 2000]. However, it remains unclear whether l_c is a numerical artifact or a true material property. Can l_c be physically measured or experimentally validated, or is it merely a conceptual tool for simplifying the problem?

Is there a correlation between l_c and known physical quantities? Additionally, a question that has persisted since Irwin’s early work [Irwin 1958] is if l_c is a real physical quantity, how it correlates with other material properties, such as fracture toughness, failure strength, or yield strength. Understanding these relationships is crucial for effectively using phase-field models to predict fracture behavior.

Can l_c be measured experimentally? If l_c is indeed a material property, the development of experimental techniques to measure it becomes crucial [Réthoré & Estevez 2013]. Additionally, understanding how l_c interacts with other dissipative phenomena, such as plasticity, is vital for applying this length scale in practical contexts.

What is the atomic-scale origin of failure? At the atomic scale, the origins of material failure are still not fully understood. While atomic-scale simulations, particularly in metallic glasses [Schuh & Lund 2003], have shed light on the yield criterion, it is unclear whether these techniques can be extended to more complex materials, such as silicate glasses. Identifying the atomic-scale mechanisms that drive failure could fundamentally reshape how we predict and prevent material degradation.

Can atomic-scale simulations predict the failure of materials with complex microstructures? A key challenge is whether atomic-scale simulations can predict macroscopic failure behaviors, particularly in materials with complex microstructures. Can con-

cepts like toughness, typically considered a nonlocal property, be accurately derived from atomic simulations? Developing a quantitative, predictive understanding of how atomic-scale features influence macroscopic fracture behavior could greatly enhance material design.

Can atomic-scale results be upscaled? Another major challenge is bridging the gap between atomic-scale simulations and experimentally validated macroscopic properties [Kermouche *et al.* 2008]. How can atomic-scale data be upscaled to predict real-world material behavior? Are there multi-scale modeling frameworks or homogenization techniques that can bridge these scales? Ensuring the accuracy and applicability of these models through experimental validation is key to making atomic-scale insights practically useful.

Can the toughness be defined for a given material architecture? Mechanical metamaterials introduce additional complexities to fracture mechanics. These materials often exhibit fracture behaviors distinct from conventional materials due to their unique microstructures. A critical question is whether it is possible to define an effective toughness for a given material architecture that holds at the macroscopic scale [Fleck *et al.* 2010]. Can this toughness be homogenized, or is it inherently dependent on the microstructure and loading conditions? Research is needed to develop homogenization techniques that account for the interplay between geometry, material properties, and fracture behavior.

Can the toughness be defined by knowing the material's elementary strength? For architected materials, which derive their properties from microstructures, can the overall toughness be predicted by analyzing a representative elementary unit cell? If so, what conditions or assumptions are necessary for this approach to be valid? Understanding whether macroscopic fracture properties can be derived from microscale analysis will be critical for the design and optimization of metamaterials.

How to optimize mechanical metamaterials? The optimization of architected materials poses significant challenges, given the vast design space and the complex interplay between material properties, geometry, and loading conditions. Current optimization methods [Watts *et al.* 2019] may not adequately capture these intricate interactions. Developing more effective optimization strategies that consider these factors could guide the design of materials with tailored fracture properties, ultimately leading to stronger and more resilient materials.

These open questions highlight the need for continued research in fracture mechanics, spanning multiple scales from atomic simulations to macroscopic observations. Resolving these issues will not only deepen our understanding of material failure but also enhance our ability to design innovative materials and structures that are both stronger and more resilient.

1.4 Thesis statement

This manuscript explores the intricate role of length scales in fracture mechanics, focusing on how material failure manifests across multiple scales, from the microscopic to the macroscopic. It aims to bridge the gap between theoretical models and practical applications by employing advanced methods such as phase-field techniques and atomic-scale simulations to analyze various fracture modes. By examining both mechanical and physical factors that influence failure, this research seeks to develop a deeper understanding of how inter-

nal length scales impact crack propagation, toughness, and strength in different materials. The study not only advances the field of fracture mechanics but also contributes to the optimization of architected materials and structural systems. Through the integration of coupled-criteria and phase-field models, it provides valuable insights for more accurately predicting material failure, with important implications for designing more resilient and efficient structures across diverse engineering applications.

Lengths in Fracture at the Continuum Scale

The chapter examines the significance of internal length scales in fracture, focusing on Irwin's length in finite fracture mechanics and phase-field regularization. By comparing the phase-field method with the coupled criterion, the chapter illustrates how these length scales affect crack initiation, propagation, and material strength in tensile, shear, and antiplane fracture modes. Dynamic fracture simulations underscore the importance of regularization in accurately capturing crack speed and branching.

Associated publications

- [G. Molnár](#), A. Doitrand, R. Estevez, A. Gravouil, *Toughness or strength? Regularization in phase-field fracture explained by the coupled criterion*, Theoretical and Applied Fracture Mechanics, 109, 102736, 2020.
- [G. Molnár](#), A. Doitrand, A. Jacon, B. Prabel, A. Gravouil, *Thermodynamically consistent linear-gradient damage model in Abaqus*, Engineering Fracture Mechanics, 266, 108390, 2022.
- E. Eid, A. Gravouil, [G. Molnár](#), *Influence of rate-dependent damage phase-field on the limiting crack-tip velocity in dynamic fracture*, Engineering Fracture Mechanics, 292, 109620, 2023.
- [G. Molnár](#), A. Doitrand, V. Lazarus, *Phase-field simulation and coupled criterion link echelon cracks to internal length in antiplane shear*, Journal of the Mechanics and Physics of Solids, 188, 105675, 2024.

Contents

2.1	Motivation	14
2.2	Irwin's length in finite fracture mechanics	14
2.3	Phase-field regularization length scale	16
2.3.1	Phase-field principles	16
2.3.2	Energy decomposition	18
2.3.3	Damage irreversibility	19
2.3.4	Homogeneous solution	20
2.4	Length scales in fracture	21
2.4.1	Tensile opening in an infinite plane	22
2.4.2	In-plane shear fracture	25
2.4.3	Antiplane echelon cracking	26
2.4.4	Connection between the methods	29
2.5	Dynamic fracture	29
2.6	Oxidation induced fracture	31
2.7	Concluding remarks	33

2.1 Motivation

Initially, the parameter l_c was introduced to aid numerical methods in solving fracture problems and to eliminate the mesh dependency of crack paths. However, [Pham & Marigo 2010a, Pham & Marigo 2010b] postulated that l_c should be separately identified, as it represents the material's internal length scale – a concept further explored in works such as [Freddi & Royer-Carfagni 2010, Pham *et al.* 2011, Piero 2013]. More recently, several studies have calibrated l_c to match the maximum load at failure observed in experiments [Nguyen *et al.* 2016c, Tanné *et al.* 2018, Kumar *et al.* 2020]. Researchers like Nguyen *et al.* [Nguyen *et al.* 2016b, Nguyen *et al.* 2016a] have even employed microtomography to identify the extent of micro-damage regions surrounding discrete cracks. Subsequent works [Zhang *et al.* 2017, Tanné *et al.* 2018, Kumar *et al.* 2020, Kumar & Lopez-Pamies 2020] demonstrated that the variational formulation of fracture mechanics can effectively bridge stress-based and toughness-based criteria. This approach allows phase-field methods to regularize the infinite critical load at infinitesimal crack lengths, as defined by the Griffith criterion, successfully reproducing size effects that have been observed experimentally for decades [Bažant 1997, Issa *et al.* 2000, Chudnovsky 2014].

While these seminal studies established that l_c is essential for accurately calculating critical loads in the presence of cracks, they primarily used the homogeneous solution in unidirectional tension to correlate l_c with the material's intrinsic strength [Tanné *et al.* 2018]. However, they did not extend their analysis to provide a simple mechanical theory that explains the transition and size effects.

This chapter aims to provide a more nuanced understanding of the elementary mechanisms introduced by the phase-field approximation. It draws a comparison between the variational phase-field approach and the coupled criterion [Leguillon 2002], one of the first theories to offer an elegant and straightforward explanation of the well-known size effect. This comparison is crucial, as the mechanism underlying phase-field simulations has not been fully explored yet.

Our goal is to deepen this comparison and evaluate the similarities between the phase-field method and the coupled criterion in terms of critical loads, crack topology, and initiation spacing in both unstable and stable crack initiation scenarios across the three fracture modes [Irwin 1958, McClintock & Irwin 1965]. This analysis sheds light on how the length scale parameter l_c influences the mechanical behavior of materials, thereby advancing our understanding of its role in phase-field models.

2.2 Irwin's length in finite fracture mechanics

The coupled criterion is an elegant tool used in finite fracture mechanics to model the effect of a length scale on crack initiation and propagation. This approach combines an energy condition with a stress-based comparison. For a crack to initiate or propagate, both criteria must be satisfied at the same increment length under the same loading condition.

The energy release rate (G) is determined through a balance between the states before and after the crack jump. In most cases, phononic dissipation is neglected, and quasi-static conditions are assumed. Two options are commonly used to calculate the energy release rate.

The first is called the incremental value, where G is considered constant during initiation and propagation:

$$G_{\text{inc}}(a_0 + \Delta a, P) = - \frac{\Psi_{\text{int}}(a_0 + \Delta a, P) - \Psi_{\text{int}}(a_0, P) - \Delta W_{\text{ext}}(F, u)}{\Delta a} \geq g_c, \quad (2.1)$$

where G_{inc} is the incremental energy release rate, Ψ_{int} is the elastic strain energy, ΔW_{ext} is the external work, and P represents the applied displacements (u) or external forces (F) on the boundaries. It reverts to the Griffith definition of the energy release rate when the incremental crack length tends towards $\Delta a \rightarrow 0$. Here, a_0 is the initial crack length, and Δa is the unknown crack increment.

The second approach assumes that the energy release rate varies during propagation. Consequently, the differential energy release rate G can be defined as:

$$\begin{aligned} G(a_0 + \Delta a/2, P) &= -\frac{\partial \Psi(a_0 + \Delta a/2, P)}{\partial a} \\ &\approx -\frac{\Psi_{\text{int}}(a_0 + \Delta a, P) - \Psi_{\text{int}}(a_0, P) - \Delta W_{\text{ext}}(F, u)}{\Delta a} \geq g_c. \end{aligned} \quad (2.2)$$

In practice, the incremental approach is used to determine the initiation state, and the differential quantity is used to determine where the crack potentially stops [Leguillon 2002]. When $\Delta a \rightarrow 0$, the incremental value converges to the differential G .

The second requirement for propagation is given by the stress criterion. We assume that the elastic stress around the crack tip along the expected crack path (described by its curvilinear abscissa s) exceeds the material's tensile strength:

$$\sigma_t(a + s, P) \geq \sigma_c, \forall 0 \leq s \leq \Delta a, \quad (2.3)$$

where σ_t is the tangential stress perpendicular to the crack's opening direction, and σ_c is the material's tensile strength.

For stable initiation, both the energy and stress functions decrease monotonously with crack advancement, making the energy release rate determine the initiation state. However, for unstable initiation, the energy criterion is an increasing function, while the stress criterion is a decreasing one. As a result, the energy criterion provides a minimum crack length, setting a lower bound where the condition is satisfied, while the stress criterion provides a maximum distance, setting an upper bound for admissible initiation crack lengths.

To satisfy both criteria simultaneously, the load is increased so that the initiation length predicted by the energy criterion decreases until it matches the value given by the stress criterion. A key conclusion of the coupled criterion is that a finite crack length Δa is created abruptly at initiation to satisfy both the strength and energy requirements. Consequently, the coupled criterion allows the determination of the critical load P_c at which the crack initiates:

$$P_c = \min \left[P, \exists \Delta a, \min \left(\frac{G_{\text{inc}}(a_0 + \Delta a, P)}{g_c}, \frac{\sigma(a_0 + \Delta a, P)}{\sigma_c} \right) \geq 1 \right], \quad (2.4)$$

as well as the admissible initiation lengths Δa_c :

$$\Delta a_c = \left[\Delta a, \min \left(\frac{G_{\text{inc}}(a_0 + \Delta a, P_c)}{g_c}, \frac{\sigma(a_0 + \Delta a, P_c)}{\sigma_c} \right) \geq 1 \right]. \quad (2.5)$$

In practice, both the energy release rate and the stress fields can be obtained analytically or through finite element methods. Under the assumption of small deformations in a linear elastic framework, only one elastic calculation is needed to compute the stress condition, whereas calculating the energy criterion requires multiple elastic calculations with varying crack lengths. An example is provided in Appendix A.1.

The introduction of the stress criterion reveals the emergence of a characteristic length, such as arrest length or characteristic crack spacing [Faria Ricardo *et al.* 2020]. This

length is often linked to Irwin’s length [Leguillon & Yosibash 2003, Martin *et al.* 2018, Molnár *et al.* 2024], which is one of the simplest ways to introduce a length scale in fracture mechanics. Irwin’s length relates Young’s modulus (E), fracture toughness, and tensile strength using the following formula [Irwin 1958]:

$$l_{\text{mat}} = \frac{Eg_c}{\sigma_c^2}. \quad (2.6)$$

Interested readers are referred to the original paper on the coupled criterion [Leguillon 2002] or a recent review [Doitrand *et al.* 2024] for more detailed information on its theory and history.

2.3 Phase-field regularization length scale

The fundamental concept underlying phase-field models for fracture is to approximate the crack discontinuity using a smeared damage field (d). Typically, a single length scale parameter (l_c) is introduced to govern the extent of damage penetration within the material. The most basic phase-field model balances elastic energy with diffused fracture energy to determine the energetically favorable crack front. Various versions of the model exist, but they share common inputs: fracture toughness g_c and the regularization length l_c .

Originally, the damage diffusion and l_c were introduced to regularize the discrete crack problem posed by linear elastic fracture mechanics, making it solvable through variational methods. However, it quickly became evident that this enrichment enabled the phase-field technique to model a wide range of fracture phenomena that were previously inaccessible to other numerical methods, while still reverting to Griffith’s theory when l_c approaches 0. This provides a unified framework that connects the widely used stress/strength-based approach with classical fracture mechanics.

2.3.1 Phase-field principles

Bourdin *et al.* [Bourdin *et al.* 2000, Bourdin *et al.* 2008] introduced the currently widely used theory for modeling fracture using variational methods. This theory is fundamentally based on the concept of damage mechanics [Kachanov 1958] and the regularization of discontinuities with a continuous field [Ginzburg & Landau 1950, Cahn & Hilliard 1958]. The new approach replaced the discrete fracture surface, as originally formulated by Griffith [Griffith 1921, Griffith 1924], within the variational framework proposed by Francfort & Marigo [Francfort & Marigo 1998]. Instead of a discrete crack surface, a continuous damage density function was employed. This transformation of the original minimization problem involved the use of the Mumford and Shah functional [Mumford & Shah 1989], a specific case within the broader Ambrosio and Tortorelli elliptic regularization framework [Ambrosio & Tortorelli 1990].

The phase-field fracture model is based on a diffuse representation of localized discontinuities, where the crack surface is approximated using a damage variable (d) that ranges from 0 to 1. A value of 0 represents an undamaged domain, while a value of 1 indicates a fully formed crack where the material has lost all resistance and stiffness. This approach allows for a gradual transition from an intact material to a fully fractured state, enabling the simulation of crack initiation and propagation without explicit crack tracking.

The evolution of damage in phase-field models is governed by a system of partial differential equations, typically coupled with the material’s mechanical behavior – initially, linear elasticity. As damage progresses, it influences the material’s mechanical response, leading to the initiation and propagation of cracks. Fundamentally, the energy of the solid

body, as represented in eq. (2.7), is minimized. The accumulation of elastic energy drives the formation of damage and the subsequent opening of cracks.

This section presents the underlying mathematical and physical framework of the phase-field approach for modeling regularized brittle fracture. The different energy contributions from individual phenomena are described, followed by an explanation of the staggered solution for solving the weakly coupled problems. Additionally, a bound constraint optimization scheme is introduced to enforce damage irreversibility. Finally, key implementation details are provided.

The energy functional for the complete two-field problem is represented by the following Lagrangian function:

$$\mathcal{L} = W_{\text{ext}}(\mathbf{u}) - \Psi(\mathbf{u}, d), \quad (2.7)$$

where $\Psi(\mathbf{u}, d)$ represents the internal energy, containing the elastic energy (Ψ_{el}) and fracture energy contributions (Ψ_{d}):

$$\Psi(\mathbf{u}, d) = \Psi_{\text{el}}(\mathbf{u}, d) + \Psi_{\text{d}}(d). \quad (2.8)$$

$W_{\text{ext}}(\mathbf{u})$ represents the external work:

$$W_{\text{ext}} = \int_{\Omega} \bar{\boldsymbol{\gamma}} \cdot \mathbf{u} dV + \int_{\partial\Omega} \bar{\mathbf{t}} \cdot \mathbf{u} dA, \quad (2.9)$$

where $\bar{\boldsymbol{\gamma}}$ and $\bar{\mathbf{t}}$ are the prescribed volume and boundary forces, respectively, as shown in Fig. 2.1b.

All internal energy components depend on either the phase-field variable (d) or the displacement field (\mathbf{u}) and its spatial derivatives.

The total energy used up in crack formation is expressed as:

$$\Psi_{\text{d}}(d) = \Gamma g_c = \int_{\Gamma} g_c d\Gamma \approx \int_{\Omega} g_c \gamma_{\Gamma}(d, \nabla d) d\Omega, \quad (2.10)$$

where Γ is the size of the discrete crack surface, g_c is Griffith's [Griffith 1921] critical energy release rate, and γ_{Γ} is the crack surface density:

$$\gamma_{\Gamma}(d, \nabla d) = \frac{1}{c_{\omega} l_c} \left[\omega(d) + l_c^2 |\nabla d|^2 \right]. \quad (2.11)$$

In the literature, various crack representations exist. The geometric function (ω) largely controls the topology of the phase-field solution. The most widely used models are the AT1 [Pham *et al.* 2011] and AT2 [Bourdin *et al.* 2000, Miehe *et al.* 2010a] representations. In the AT1 approach, $\omega(d) = d$, while for AT2, $\omega(d) = d^2$. Additionally, Wu [Wu 2018] proposed a mixed representation that yields cohesive zone model-like behavior.

The total integral over the simulation domain of the crack surface density function should yield the theoretical value of the discrete representation. Depending on the model, γ_{Γ} is normalized by the constant c_{ω} :

$$c_{\omega} = 4 \int_0^1 \sqrt{\omega(s)} ds, \quad (2.12)$$

with $c_{\omega} = 8/3$ for AT1 and $c_{\omega} = 2$ for AT2 models. Fig. 2.1a illustrates the basic concept of diffuse damage models with the 1D analytical solutions for AT1 and AT2 representations.

The advantage of AT1 compared to AT2 is that it has an elastic threshold before failure, whereas in AT2 models, damage appears at any loading level. However, AT1 models require special treatment to enforce positive damage values and ensure damage irreversibility.

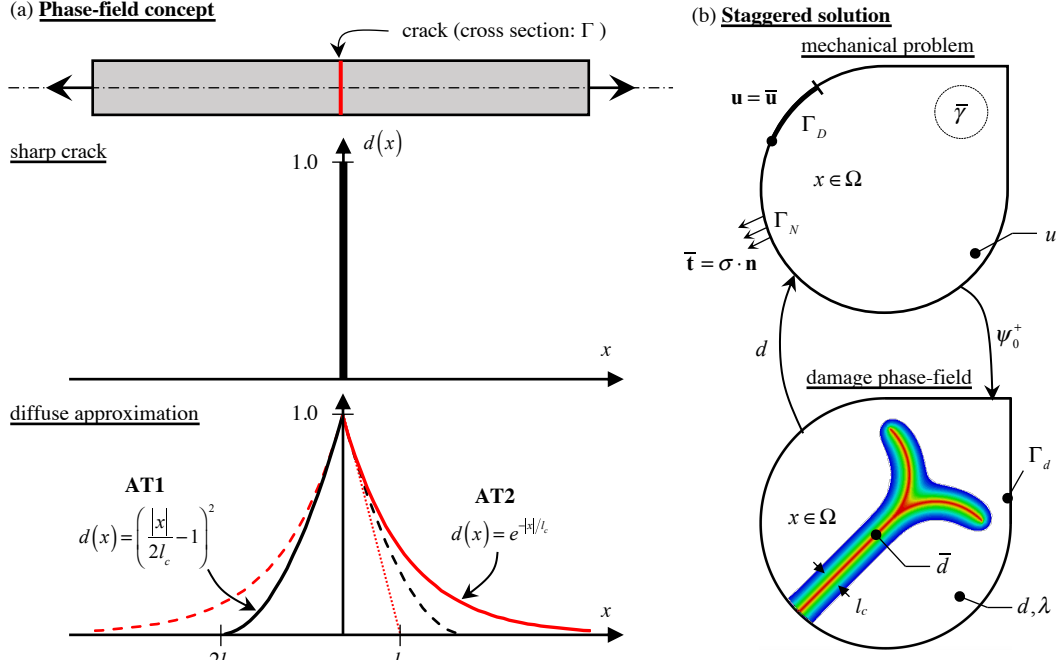


Figure 2.1: (a) 1D bar with a crack in the middle and a cross section Γ . Below is the damage field with a sharp crack at $x = 0$ and the diffuse representation with models AT1 (black) and AT2 (red) with the length scale parameter l_c . (b) Schematic illustration of the staggered solution used to solve the coupled mechanical and fracture problem.

2.3.2 Energy decomposition

The principal idea of damage mechanics is that damage reduces the elastic strain energy, thereby weakening the material's resistance and stiffness. As a result, the elastic strain energy contribution can be expressed as follows:

$$\Psi_{el}(\mathbf{u}, d) = \int_{\Omega} \psi(\mathbf{u}, d) d\Omega, \quad (2.13)$$

where ψ is the strain energy density. To avoid fracturing under compression, ψ is split into two parts:

$$\psi(\mathbf{u}, d) = g(d) \psi_0^+(\boldsymbol{\varepsilon}(\mathbf{u})) + \psi_0^-(\boldsymbol{\varepsilon}(\mathbf{u})), \quad (2.14)$$

where $g(d)$ is the energy degradation function. The simplest and most commonly used function is:

$$g(d) = (1 - d)^2 + k, \quad (2.15)$$

with k being a small number (10^{-12}) that conditions the solution. This function must satisfy several basic conditions: (i) it is 0 at $d = 0$ and 1 at $d = 1$, (ii) it is continuous and monotonic in this range, and (iii) its derivative is 0 at $d = 0$.

The subscripts in eq. (2.14) refer to the tensile (+) and compressive (−) energies. The degradation function is applied only to the tensile part to avoid crack opening under compression, ensuring that compression does not contribute to the crack-driving force.

As highlighted previously [Molnár *et al.* 2020b], this technique suffers from a critical numerical issue, usually addressed by introducing a small perturbation: when two eigenvalues out of three are equal, the solution becomes singular. One might assume that this only occurs in rare cases, but common examples such as uniaxial or equibiaxial configurations fall into this category. This paper details how we updated [Molnár *et al.* 2022] the original spectral decomposition technique to provide a more robust and faster solution.

To stabilize the solution, we first expressed the complete stiffness tensor in the principal directions and then rotated it back to the original reference system:

$$\mathbf{C} = \mathbf{T}_\sigma^{-1} \hat{\mathbf{C}} \mathbf{T}_\varepsilon. \quad (2.16)$$

Here, $\hat{\mathbf{C}}$ is the stiffness matrix in the principal directions, while \mathbf{T}_ε and \mathbf{T}_σ are rotation matrices in Voigt notation, compiled from the original basis of the strain tensor.

The stiffness matrix in the principal directions can be written as a block matrix:

$$\hat{\mathbf{C}} = \begin{bmatrix} \mathbf{L} & \mathbf{0} \\ \mathbf{0} & \mathbf{S} \end{bmatrix}, \quad (2.17)$$

where \mathbf{L} is the well-known 3x3 matrix [Bernard *et al.* 2012] deduced from the potential energy:

$$\mathbf{L} = \frac{\partial^2 \psi}{\partial \hat{\boldsymbol{\varepsilon}}^2}, \quad (2.18)$$

with $\hat{\boldsymbol{\varepsilon}}$ referring to principal strains. As there is no shear strain in the principal directions, the shear term \mathbf{S} is often omitted from descriptions, but it can be obtained via numerical experimentation. We found that for all stable cases ($\varepsilon_1 \neq \varepsilon_2 \neq \varepsilon_3$), this block reduces to a 3-component diagonal matrix where damage affects the shear stiffness components through a linear combination of the corresponding in-plane principal strain values.

2.3.3 Damage irreversibility

Various methods have been proposed to resolve the coupled mechanical and fracture problem [Chaboche *et al.* 2001, Lorentz & Benallal 2005, Miehe *et al.* 2010a, Wick 2017, Wu & Huang 2020]. In the present implementation, the weakly coupled equations are solved in a staggered manner [Miehe *et al.* 2010b, Molnár & Gravouil 2017]. When searching for the mechanical solution, the damage variable is kept constant. The results presented in this document were obtained either by creating custom finite elements using the commercial finite element software Abaqus/Standard [ABAQUS 2011], or by utilizing in-house MATLAB subroutines.

One of the standard approaches for enforcing the irreversibility constraint ($\dot{d} \geq 0$) in AT2 models is to replace the crack-driving function (elastic tensile strain energy) with a history field [Miehe *et al.* 2010b]. This history variable corresponds to the maximum elastic energy over the full temporal history. Although there is no formal proof that this approximation fully enforces the irreversibility of the damage, it is widely used due to its simplicity. In our previous implementations [Molnár & Gravouil 2017, Molnár *et al.* 2020b, Jacon *et al.* 2023], we also employed Miehe's technique. However, it should be noted that if the gradient term in eq. (2.11) increases, d must decrease for a constant \mathcal{H} , which locally violates the irreversibility condition.

Various methods have been developed to enforce damage irreversibility in phase-field models of fracture. One such approach is the penalty method [Gerasimov & De Lorenzis 2016], which introduces an additional term into the total energy

functional to penalize any violation of the irreversibility constraint. This method prevents damage from decreasing by making any healing energetically prohibitive. However, the choice of the penalty coefficient is critical, as an inappropriate value can lead to numerical instability. In contrast, the projected successive over-relaxation method [Mangasarian 1977], framed as a symmetric linear complementarity problem [Marengo *et al.* 2021], offers a more direct enforcement of irreversibility. By explicitly projecting the phase-field increments onto non-negative values during each iteration, the method ensures that damage always increases or remains constant, resulting in improved computational efficiency and stability compared to the penalty method.

For the results presented herein, we enforced a positive damage increment using Lagrange multipliers. Wheeler *et al.* [Wheeler *et al.* 2014] recently proposed an augmented Lagrangian method to solve the bound-constrained optimization of the phase-field problem. This approach was later applied to approximate cracks under dynamic and cohesive fracture conditions [Geelen *et al.* 2019]. However, due to limitations in the Abaqus/UEL framework, such as the lack of access to global residual and stiffness arrays, we employed the computationally more expensive Lagrange multiplier technique [Lu *et al.* 2020].

To introduce the Lagrange multipliers, the original Lagrangian equation was modified as follows:

$$\mathcal{L} = W_{\text{ext}}(\mathbf{u}) - \Psi(\mathbf{u}, d) + \sum_{j=\{\mathbf{d}_n > \mathbf{d}_{n+1}\}} \lambda_j f_j(d), \quad (2.19)$$

where the functions f_j contain the inequalities that enforce the lower bound of the nodal damage values:

$$f(d_{n+1}) = -d_{n+1} + d_n \leq 0. \quad (2.20)$$

In eq. (2.19), the index j denotes the active constraints (where $d_n > d_{n+1}$), and λ_j are the Lagrange multipliers.

Further details about the mathematical theory of the phase-field formulation can be found in our recent papers [Molnár & Gravouil 2017, Molnár *et al.* 2020b, Molnár *et al.* 2022].

2.3.4 Homogeneous solution

The simplest way to analyze the phenomenological effect of g_c and l_c is by calculating the homogeneous solution of eq. (2.7). When the gradient term is neglected in eq. (2.11), the solution simplifies, allowing the damage to be expressed directly as a function of the elastic strain energy. The most common result is the stress-strain curve under uniaxial tension, as shown in Fig. 2.2a. However, the maximum achievable stress during deformation is influenced by the ratio of the principal stresses.

The tensile strength (σ_c) of a material is defined as the maximum tensile stress (σ_1) it can withstand before failure. When the gradient term is neglected, the homogeneous solution for the tensile strength in the case of an AT2 representation can be derived from the material parameters as follows: $\sigma_c = \sqrt{\frac{27Cg_c}{256l_c}}$ for unidirectional extension, where $C = \frac{E(1-\nu)}{(1+\nu)(1-2\nu)}$, with E as Young's modulus and ν as Poisson's ratio. This relationship can be generalized as:

$$\sigma^c \doteq \sigma_1^{\max} = \eta \left(\nu, \frac{\sigma_2}{\sigma_1}, \frac{\sigma_3}{\sigma_1} \right) \cdot \sqrt{\frac{Eg_c}{l_c}}, \quad (2.21)$$

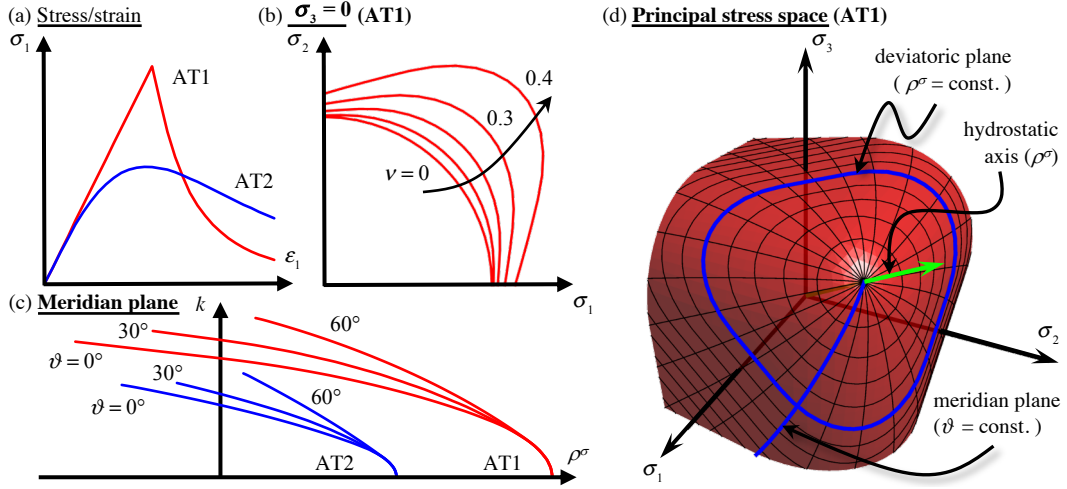


Figure 2.2: Homogeneous solution for problem AT1 and AT2: (a) First principal stress as a function of the first principal strain; (b) meridian slices for different Lode angles; (c) AT1 model for in-plane stress conditions and different values of Poisson’s ratio; (d) failure surfaces in the space of principal stresses.

where the function η accounts for the effects of the stress state and Poisson’s ratio. Moreover, atomic-scale simulations have shown [Molnár *et al.* 2016b] that the response of brittle materials (*e.g.*, silica) under tension may depend not only on the hydrostatic stress state but also on the Lode angle (the angle of the deviatoric plane). Therefore, the material’s resistance should be described with a three-dimensional failure or yield surface.

Fig. 2.2d shows the failure surface in the space of all three principal stresses for the AT1 and AT2 models with identical phase-field parameters. Fig. 2.2b and (c) depict the maximum surface under plane stress conditions ($\sigma_3 = 0$) and slices of the meridian planes (constant Lode angle). The plotted surfaces resemble a Rankine criterion [Rankine 1857] with rounded corners. Indeed, when $\nu = 0$, the phase-field solution approximates a Rankine-type surface with circularly rounded edges in the tensile domains.

Since the AT2 model lacks an elastic threshold, it consistently shows lower strength compared to the AT1 formulation. Furthermore, the tensile meridians are weaker than their compressive counterparts.

The algorithm to calculate the maximum stress as a function of Poisson’s ratio and the principal stress state is available as a Supplementary File in Ref. [Molnár *et al.* 2022]. The homogeneous solution can provide an initial estimate for l_c based on the measured material strength [Molnár *et al.* 2020a].

2.4 Length scales in fracture

Even though Irwin initially cautioned the community about the limitations imposed by Griffith’s original theory and his stress intensity factor [Irwin 1958], the stress intensity factor became synonymous with toughness measurement in engineering materials. Irwin demonstrated among the first that when the size of the sample is sufficiently small, the normalized resistance (and thus the strength) of the material is independent of the characteristic size. However, as the diameter of the sample exceeds a certain threshold, the

average stress at failure significantly decreases. He therefore defined two regions: the first, where the size of the defect or sample is small, and the second, where the setup is suited to fracture mechanics and, consequently, the use of the stress intensity factor. His original figure is reproduced in Fig. 2.3a. Irwin also classified crack types based on the applied loading. In the context of linear elastic fracture mechanics, loading near a preexisting crack can be decomposed into three modes: mode I, corresponding to tensile opening; mode II, corresponding to in-plane shear; and mode III, corresponding to antiplane shear [Irwin 1958, McClintock & Irwin 1965].

For example, when in-plane shear is applied, the original crack front bifurcates, and a new crack forms at a specific angle. It is noted that this angle depends on the geometry and material being loaded [Richard *et al.* 2014] and has been observed to vary between $63 - 71^\circ$. The experimental observation in Fig. 2.3b, taken from glass, is reproduced from Ref. [Erdogan & Sih 1963].

The most complex case occurs when a mother crack is subjected to shear perpendicular to its original direction. Instead of simply propagating horizontally, the original crack fragments into facets, known as daughter cracks. These newly formed cracks interact and eventually form the macroscopically observed fracture pattern. An example of this phenomenon is demonstrated in Fig. 2.3c using a gelatinous solid, caramel flan. It is important to note that this behavior has been observed in various other materials as well.

In summary, linear elastic fracture mechanics explains only a limited portion of the physical phenomena observed in nature, and its limitations should be properly understood to avoid misuse in practice. Therefore, this chapter is dedicated to the three elementary fracture modes, which will be analyzed through the lens of the phase-field technique and the coupled criterion. Here, we present only the key results. For modeling details, we refer to our previous papers [Molnár *et al.* 2020a, Molnár *et al.* 2024].

2.4.1 Tensile opening in an infinite plane

Perhaps the simplest way to demonstrate the size effect in fracture mechanics is by analyzing an infinite homogeneous plane subjected to uniform tensile stress applied at infinity. A single straight crack of length $2a_0$ is positioned in the center. The advantage of this elementary case is that both the stress field and the energy release rate are available analytically.

Coupled criterion. For the coupled criterion, the stress on the x axis ($y = 0$) measured from the crack tip can be calculated using the following equation [Sun & Jin 2012]:

$$\sigma_y(x) = \frac{\sigma_y^0(x + a_0)}{\sqrt{x(x + 2a_0)}}, \quad (2.22)$$

where σ_y^0 is the tensile stress acting on the solid body at infinity.

The energy-based criterion states that a crack advances when the released potential energy from the creation of a unit crack surface exceeds a material's critical energy release rate, as postulated by Griffith. This critical energy release rate is a material constant unique to each material. The criterion is written as a stability condition for unit thickness:

$$\frac{d}{da}(\Psi_d - \Psi) = 0, \quad (2.23)$$

where Ψ is the additional elastic strain energy induced by the stress concentration around a pre-existing crack:

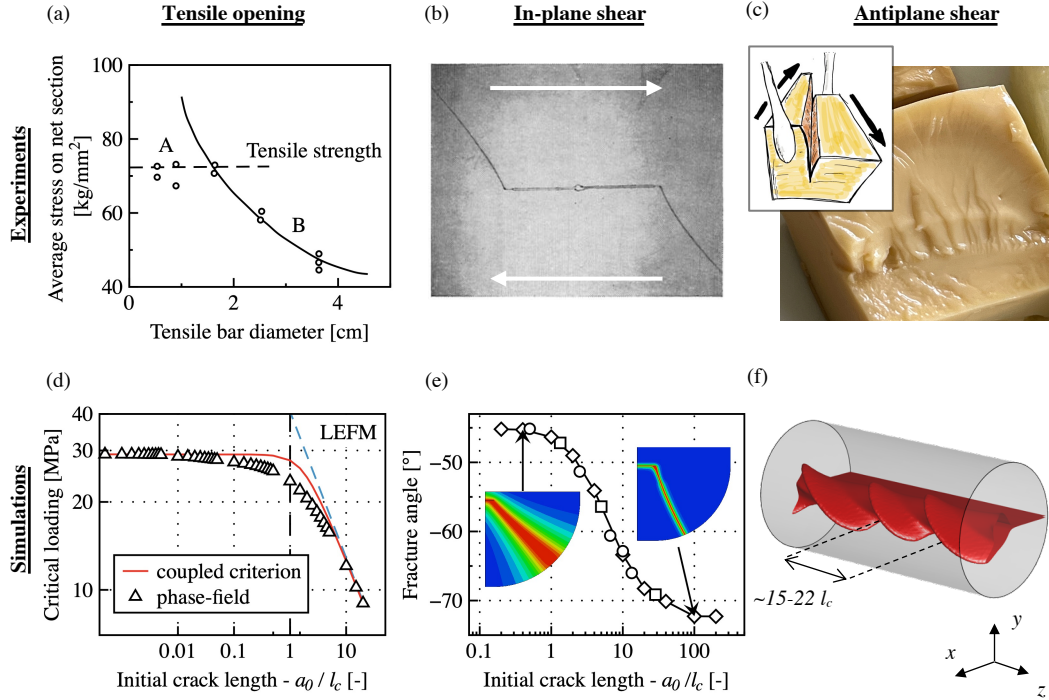


Figure 2.3: Elementary modes of fracture. First row presents experimental results: (a) size effect in tensile samples [Irwin 1958]; (b) crack deviation in shear [Erdogan & Sih 1963]; and (c) echelon cracking in solids (experiment done in collaboration with Aurélien Doitrand on a caramel flan). Second row present simulation results: (d) critical tensile loading as a function of the initial crack length with both method; (e) initiation angle in in-plane shear as a function of the initial crack length with the phase-field method; (f) echelon crack formation in pure antiplane shear conditions.

$$\Psi = \frac{\pi(a_0 + \Delta a)^2}{8\mu} (\kappa + 1) (\sigma_y^0)^2, \quad (2.24)$$

and W is the fracture energy consumed by the crack's creation:

$$\Psi_d = 2g_c (a_0 + \Delta a). \quad (2.25)$$

In eq. (2.24), μ is the shear modulus, and $\kappa = 3 - 4\nu$ for the plane strain case. Eq. (2.23) can be rewritten to yield the differential energy release rate:

$$G = \frac{\pi(a_0 + \Delta a)}{8\mu} (\kappa + 1) (\sigma_y^0)^2 = g_c. \quad (2.26)$$

The incremental energy release rate can be calculated by averaging G over Δa or recalculating the difference between two distinct states, giving the following:

$$G_{\text{inc}} = \frac{\pi(a_0 + \Delta a/2)}{8\mu} (\kappa + 1) (\sigma_y^0)^2 = g_c. \quad (2.27)$$

This equation highlights a few important points. First, when $a_0 + \Delta a = 0$, meaning no crack is present, the energy release rate is zero. Thus, the load applied at infinity can

be infinitely large, independent of the fracture toughness. Second, when reformulated, the critical loading as a function of the initial crack length follows a hyperbolic square root function, consistent with linear elastic fracture mechanics.

By equating the critical distance from the incremental energy release rate with the critical distance where the stress criterion is satisfied, we can express the loading required for crack propagation. It is worth noting that the critical load depends not only on the material's strength and fracture toughness but also on the geometry (initial crack length). Thus, the size effect can be captured with this formulation. The critical loading for a given set of E , g_c , and σ_c is shown in Fig. 2.3d (red solid line). It can be observed that for sufficiently large cracks, the coupled criterion results converge with predictions from linear elastic fracture mechanics. For small cracks, the values converge to a single strength value, demonstrating a smooth transition between behaviors without the need for plasticity.

Phase-field. To model the same problem using the phase-field approach, a $\hat{d} = 1$ Dirichlet boundary condition was prescribed on the initial crack. This phase-field value is necessary because creating a crack requires more energy than propagating an existing damage field [Klinsmann *et al.* 2015, Sargado *et al.* 2018, Tanné *et al.* 2018].

The results obtained using the finite element method and the phase-field method were influenced by both spatial and temporal discretization. Thus, a convergence study was conducted to minimize numerical errors.

The time step was automatically controlled, with the local potential energy increment constrained by the following condition:

$$d\psi_0^+ \leq \xi \cdot \frac{g_c}{c_\omega l_c}, \quad (2.28)$$

where ψ_0^+ is the elastic (undamaged) strain energy used in staggered schemes [Molnár *et al.* 2022], and ξ is a scalar multiplier set to 50%.

Fig. 2.3d presents a similar size effect as observed with the coupled criterion, showing critical stresses as a function of the initial crack length. The phase-field method successfully reproduced the same size effect observed experimentally. Furthermore, deviations from linear elastic fracture mechanics (LEFM) occur when the initial crack size approaches or becomes smaller than l_c .

The results in Fig. 2.3d are significant because they demonstrate that introducing crack diffusion (via the length scale l_c) does not undermine Griffith's original description but rather adds a powerful tool for capturing real-life physical phenomena. While the choice of phase-field representation affects model behavior, it is essential to recognize that l_c carries a real mechanical meaning.

Multiple simulations were performed with $a = 0$ in the phase-field calculation to determine the correlation between tensile strength and the length scale. In this case, the initial damage field was prescribed only at a single node. As previously explained, the critical initiation stress corresponds to the material's strength, enabling a direct comparison for various length scales in the phase-field method. The critical stress results are shown as a function of l_c in Fig. 2.4a, along with the homogeneous solution from eq. (2.21) for uniaxial tension (with principal stress ratios $\sigma_2/\sigma_1 = 0$, $\sigma_3/\sigma_1 = 0$, and $\nu = 0.37$). A clear correlation between the two quantities can be observed. As l_c decreases, tensile strength increases and tends toward infinity, which is consistent with Griffith's original solution, as the critical loading tends to infinity when $a \rightarrow 0$.

2.4.2 In-plane shear fracture

After assessing the critical stress for the two methods as a function of the initial crack length, this section focuses on the crack's topology, specifically the branching angle. For in-plane shear fracture, predicting the initiation angle remains an unresolved question. Many theories have been proposed, based on maximum tangential stress [Erdogan & Sih 1963], strain energy density [Sih 1974], energy release rate [Wu 1978, Hayashi & Nemat-Nasser 1981], and stress intensity factors [Leblond 1989, Amestoy & Leblond 1992]. Some of these models successfully reproduce specific experiments [Erdogan & Sih 1963], but none provide a universal law valid for all materials [Ayatollahi & Aliha 2009, Richard *et al.* 2014].

We hypothesize that variations in initiation come from differences in regularization length, particularly the ratio of strength to toughness. Therefore, we set out to analyze the initiation using both the coupled criterion and the phase-field method to establish a correlation based on these parameters.

Coupled criterion. Unfortunately, no analytical solutions are available to test the coupled criterion for mode II fracture. Only certain aspects of the stress and energy fields are known. The elastic stress field around the initial crack tip is described in various textbooks [Broek 1982, Sun & Jin 2012], while the energy release rate is available only for the case where $\theta = 0$.

To address this, we followed the modeling strategy below: first, finite element calculations were performed with varying crack lengths in different directions ($-90^\circ \leq \theta \leq 0$), and then the global energy difference was calculated for each crack increment. Finally, empirical functions were fitted to the results.

We identified that the critical stress defined by the Griffith criterion for pure shear fracture is:

$$\tau_{xy}^{0,c} = \sqrt{\frac{8\mu g_c}{f_c a_0 \pi (\kappa + 1)}}, \quad (2.29)$$

where $f_c = 1.504$ corresponds to the local extremum (saddle point) in the direction $\theta = -75.74^\circ$. The boundary shear stresses (τ_{xy}^0) acted on the sides at infinity, and the initiation angle θ was measured from the horizontal axis. These results correspond well with previous analytical solutions [Wu 1978].

For mode I, the crack path is assumed to be known. However, for mode II fracture, both the critical shear stress and the initiation angle are unknown. Unlike mode I, where only the critical stress and initiation length are required, mode II requires determining the spatial intersection of two curves: one where the stress criterion is satisfied and the other where the energy criterion is met.

As a result, we found that the crack could initiate in multiple directions, with the propagation angle depending on the material and geometry, ranging between $\theta = -45^\circ$ and -75.74° . This observation aligns well with the experimental results of Richard *et al.* [Richard *et al.* 2014].

Phase-field. To test the hypothesis established using the coupled criterion, phase-field calculations were conducted.

Due to the diffused nature of the crack, determining its exact path at re-initiation was challenging. Therefore, to extract the initiation angle, we identified the local maxima of the damage field at a distance larger than l_c . These positions were then fitted with a third-order polynomial, which was extrapolated to the crack lips.

This section focuses on the crack topology rather than the critical stress, as the case with $a_0 = 0$ is equivalent to the geometry presented in the first section, but with a different σ_2/σ_1 ratio. Only the limit cases were compared. We found that for small cracks, the homogeneous solutions matched well with the critical values obtained from the phase-field model. In the case of larger a_0 , the results closely matched Griffith's solution (eq. 2.29).

Compared with tensile strength, the advantage of the length scale parameter is that it introduces an internal size. Fig. 2.3e shows the initiation angle as a function of the dimensionless initial crack length, a_0/l_c . This indicates that both crack initiation and propagation depend only on the ratio of the original crack length to l_c , which corresponds well with the energy landscape defined by the coupled criterion.

For large a_0 , the crack initiates at an angle around $\sim -73^\circ$, consistent with the values obtained using the coupled criterion. On the other hand, for large l_c values, the crack inclination is -45° , which agrees with both theoretical and coupled criterion perspectives.

For a given initial crack length, the inclination angle is sensitive to the chosen σ_c values. To establish the correlation between l_c and σ_c based on the initiation angle, a_0 was varied. First, we determined a range of a_0 for a given σ_c , where the initiation angle lay between -61° and -46° . We then subdivided the obtained a_0 interval and calculated θ_c . Each initiation angle was interpolated between the phase-field results to obtain a normalized length scale. Finally, this value was multiplied by the initial crack length to determine l_c as a function of σ_c and θ_c .

Fig. 2.4a shows the correlation between l_c and σ_c . It can be observed that the topological correlation agrees with the homogeneous solution (based on critical stress).

2.4.3 Antiplane echelon cracking

The quantitative understanding of fracture under antiplane shear (mode III) is relatively obscure compared to modes I and II, primarily due to the complexity and 3D nature of the crack propagation pattern. While propagation in modes I and II generally occurs smoothly and can be addressed using a 2D elasticity problem, mode III loading often results in the fragmentation of the crack into numerous facets with complex 3D shapes [Sommer 1969, Knauss 1970, Lazarus *et al.* 2008, Pham & Ravi-Chandar 2014], making accurate prediction of its morphology challenging.

The first well-controlled experiments demonstrating crack facet segmentation were conducted by [Sommer 1969] using glass. Around the same time, [Knauss 1970] and later [Palaniswamy & Knauss 1978] showed the formation of semi-penny-shaped cracks under pure mode III conditions. Since the 1970s, researchers have demonstrated that the appearance of daughter cracks is independent of the material, occurring during tectonic plate movement [Pollard *et al.* 1982, Cox & Scholz 1988], mountain orogeny [Younes & Engelder 1999], and in materials such as polymers [Hull 1994, Lazarus *et al.* 2008, Lin *et al.* 2010, Chen *et al.* 2015], gels [Ronsin *et al.* 2014], gypsum, and even cheese [Goldstein & Osipenko 2012].

The mode III problem can be addressed at two scales. At the macroscopic scale, crack propagation is governed by the principle of local symmetry or the maximum energy release rate criterion [Amestoy & Leblond 1992], meaning that in mixed mode I+III, the crack propagates globally in a horizontal direction [Sommer 1969]. In bending experiments, mode II changes sign across the front, causing opposite tilt angles so that the front appears to rotate progressively until it aligns perpendicularly to the bending direction [Lazarus *et al.* 2008].

On the microscopic scale, however, the crack tip undergoes fragmentation into facets due to local mode III opening. These facets initiate at an angle to the main crack and

gradually coalesce during propagation, creating a jagged macroscopic surface. While the macroscopic problem is relatively straightforward to model [Gravouil *et al.* 2002, Citarella & Buchholz 2008, Wu & Huang 2020, Molnár *et al.* 2022], the phenomenon at the micro-scale is more complex. Therefore, this chapter focuses specifically on the micro-scale initiation of facets under pure mode III loading.

Consider a planar crack with a straight crack front within an infinite linear elastic medium characterized by Young's modulus (E), Poisson's ratio (ν), and critical fracture energy (g_c). Our objective is to study crack propagation under increasing mode III loading, denoted as K_{III} , applied uniformly along the crack front.

Coupled criterion. The main challenge in implementing the coupled criterion is identifying an appropriate parameter space that describes the crack opening while satisfying both the energy and stress criteria.

As suggested by previous studies [Leguillon 2014, Doitrand & Leguillon 2018b], the crack path can be determined by analyzing stress isocontours around the main crack in the absence of segments, establishing a lower bound for surface opening. To calculate the tensile stress at a specific point in space, we used the analytic, singular solution for an elastic body with a large crack, where $r \ll a_0$ (with a_0 as the initial crack length) [Westergaard 1939]:

$$\sigma_\theta(r, \theta, \phi) = \frac{K_{\text{III}}}{\sqrt{2\pi r}} \cos\left(\frac{\theta}{2}\right) \sin(2\nu), \quad (2.30)$$

where the stress is described in polar coordinates, with r as the distance from the crack tip, θ as the angle in the crack plane, and ν as the inclination angle.

Cracks form in regions where $\sigma_\theta \geq \sigma_c$. This region can be represented as an isosurface that outlines where crack opening is possible. For simplicity, we assume the instantaneous formation of a planar crack, defining a two-dimensional surface within this isosurface by intersecting it at $\nu = 45^\circ$, where tensile stress is maximal. The surface area is expressed in dimensionless form as:

$$\frac{K_{\text{III}}}{\sigma_c \sqrt[4]{\Delta S}} = f(\nu), \quad (2.31)$$

where $f(\nu = 45^\circ) \approx 2.207$. This shape is qualitatively similar to experimental observations [Pham & Ravi-Chandar 2016] and phase-field simulations, making it a reasonable choice.

This crack shape allows us to characterize the crack opening using two variables: (i) the surface area of the crack (ΔS) and (ii) the distance between crack segments (Λ).

For mode III loading, the stress field is already known, but the incremental energy release rate for crack opening must be determined as a function of the crack parameters (ΔS , Λ). A series of finite element calculations were performed to compute the potential energy for increasing crack opening ΔS . We found that the normalized incremental energy release rate as a function of normalized crack surface area ($\Delta S/\Lambda^2$) has a local maximum, with the position ($\Delta \tilde{S}_{\text{max}}$) and amplitude (\tilde{G}_{max}) depending on Poisson's ratio.

The goal is to determine the characteristic initiation distance between facets (Λ). Since \tilde{G}_{max} is independent of the initiation distance, we can use it to calculate the critical load for a given Poisson's ratio. The energy release rate at facet initiation is:

$$G = \frac{K_{\text{III}}^2(1+\nu)}{E} \tilde{G}_{\text{max}}(\nu). \quad (2.32)$$

By equating G to the material's fracture toughness g_c , we find the critical load:

$$K_{\text{III}}^{\text{cr}} = \sqrt{\frac{Eg_{\text{mat}}}{\tilde{G}_{\text{max}}(\nu)(1+\nu)}}. \quad (2.33)$$

Substituting this critical load into eq. (2.31) yields the surface area where the stress criterion for initiation is satisfied, $\Delta S_{\sigma}^{\text{cr}}$, and where $\sigma_{\theta} \geq \sigma_c$. Using the position of $\Delta \tilde{S}_{\text{max}}$, we can calculate the characteristic facet distance:

$$\Lambda = \sqrt{\frac{\Delta S_{\sigma}^{\text{cr}}}{\Delta \tilde{S}_{\text{max}}(\nu)}}. \quad (2.34)$$

This establishes a correlation where E , g_{mat} , σ_c , and ν are the key variables. From this, l_{mat} (as in eq. 2.6) can be extracted, yielding the following relation for pure antiplane shear:

$$\frac{\Lambda}{l_{\text{mat}}} = \frac{1}{(1+\nu)\tilde{G}_{\text{max}}(\nu)f^2\sqrt{\Delta \tilde{S}_{\text{max}}(\nu)}}. \quad (2.35)$$

Here, \tilde{G}_{max} and $\Delta \tilde{S}_{\text{max}}$ are dimensionless constants influenced by Poisson's ratio, and f links the loading and σ_c to the newly opened surface (see eq. 2.31). These findings suggest that the characteristic facet initiation distance is tied to the material's intrinsic length and influenced by Poisson's ratio.

Phase-field. In the phase-field model, we simulated a planar crack inside a cylinder with large enough dimensions to approximate an infinite medium. Pure mode III displacement boundary conditions were applied to the cylinder's mantle, with periodicity enforced in the out-of-plane direction.

The problem was solved using a staggered approach, with load steps controlled by an elastic energy increment scheme. A parametric study was conducted to examine the effect of load step size on crack pattern convergence. Eight-node hexahedral elements were used, with element size matching a critical length scale. Although the critical load was affected by mesh coarseness, the crack pattern remained consistent.

As noted by [Pham & Ravi-Chandar 2017], facet initiation under antiplane shear does not occur without a perturbation in the model. To resolve this, we introduced a 3D Gaussian random field [Lang & Potthoff 2011, Dietrich & Newsam 1997] to spatially alter the material's critical fracture toughness (g_c).

Fig. 2.3f shows the damage isosurface for $d = 0.8$ at the start of propagation. Initially, a homogeneous damage zone appeared around the crack tip, exhibiting self-similarity in the z direction. As the load increased, daughter cracks began to form at a characteristic distance. These cracks extended in a fin-like shape, curving back and reconnecting with the main crack front, forming a recurring pattern similar to [Leblond *et al.* 2011].

Our results showed that the initiation distance between neighboring facets is proportional to the phase-field regularization length scale and a function of Poisson's ratio. Comparing the two methods yielded initiation distances consistent with experimental measurements from [Knauss 1970].

The numerical experiments presented here are novel in that they showcase facet initiation in a nearly pristine sample, without any significant defects or perturbations influencing the crack pattern. This suggests that the crack pattern is physically significant, and its statistical properties are independent of the perturbations used. The existence of facets implies the need for regularization because, for a vanishing l_c , the facet distance also reduces to zero. Thus, the experimental presence of facets suggests the existence of a regularization length scale.

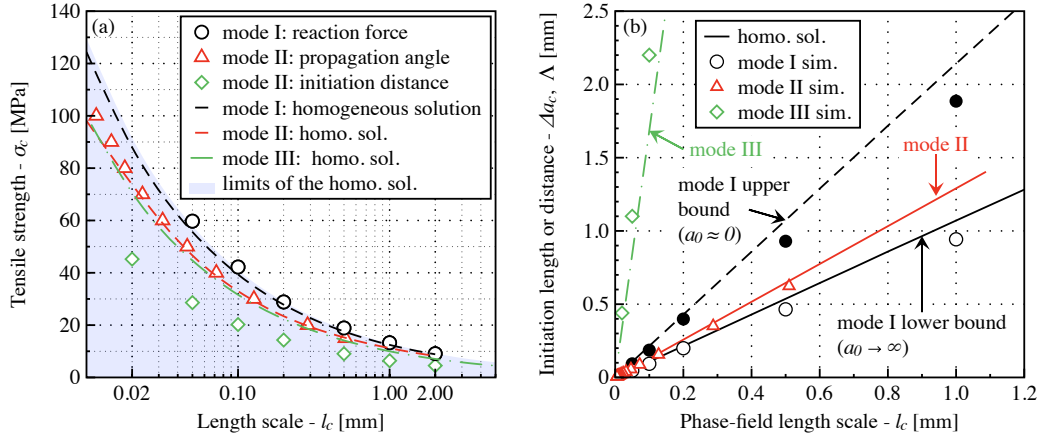


Figure 2.4: (a) Summarized correlations between the tensile strength (σ_c) and the internal length scale (l_c). The blue shade represents the accessible space based on the homogeneous solution. (b) Correlation between l_c and the initiation lengths and characteristic distances.

2.4.4 Connection between the methods

The correlations obtained from all three cases are summarized in Fig. 2.4. Generally, the correlation is clear: with a lower l_c , the strength (σ_c) increases. However, this relationship cannot be described by a single master curve; instead, it should be interpreted as a failure surface. Based on the envelope shown in Fig. 2.2, it varies within the range depicted by the blue shade in Fig. 2.4.

While distance does not explicitly appear as a material parameter in the coupled criterion, the initiation length is crucial in determining where both criteria are simultaneously satisfied. To calculate Δa_c for each l_c value, the following procedure was used: (i) first, the correlation between l_c and σ_c was established, as shown in Fig. 2.4a; (ii) then, the identified σ_c was used in the coupled criterion to compute Δa_c . Generalizing this relationship, the correlation between l_c and Δa_c is plotted in Fig. 2.4b. The black solid and dashed lines show the correlation for tensile opening mode based on the homogeneous solution, while the hollow and solid circles represent the actual phase-field simulations.

Similarly to mode I, results for both in-plane and antiplane shear are depicted using red triangles and green diamonds, respectively. Remarkably, all correlations are perfectly linear. Although geometry affects the quantitative values, we hypothesize that the actual initiation length (and thus the assumed process zone size and shape) is geometry-dependent. This implies that l_c serves as an intermediate quantity between Irwin's intrinsic length and the actual process zone size. While l_c accounts for the local stress state, it cannot fully capture the influence of macroscopic geometry.

2.5 Dynamic fracture

Previously, it was shown that without a regularization technique, multiple physical phenomena cannot be modeled in fracture. Interestingly, this is also true for dynamic fracture. When a crack is subjected to a stress wave large enough to initiate the crack, it typically accelerates and branches at a specific maximal velocity. It was long theorized that this limiting velocity is the Rayleigh wave speed (c_R) [Freund & Freund 1998]. Indeed, without

regularization, in an elastic, linear material, the energy release rate reduces to zero when the crack propagates at c_R [Doitrand *et al.* 2022]. However, experimental observations, such as in tempered glass [Molnár *et al.* 2016a], show that the critical propagation speed is much lower, approximately 50-60% of c_R . Interestingly, the phase-field technique reproduces this observation without additional adjustments, and independently of the choice of g_c or l_c [Molnár 2024].

In particular, a study reported [Bleyer *et al.* 2017] that the limiting velocity for materials such as PMMA is around $0.68c_R$ under certain loading conditions. Before reaching this velocity, the crack experiences a velocity-toughening mechanism, where the apparent fracture energy increases significantly as the crack velocity rises. This increase in fracture energy is associated with instabilities, including microbranching, which leads to surface roughening [Bleyer & Molinari 2017]. These instabilities ultimately act as a barrier, preventing the crack from reaching the Rayleigh wave speed. The findings underscore that the crack velocity is not solely determined by material properties but also by the specific loading and boundary conditions.

To model dynamic crack propagation, we added [Molnár *et al.* 2020b] the kinetic energy of the solid into the in eq. (2.7):

$$\mathcal{L} = D(\dot{\mathbf{u}}) - \Psi(\mathbf{u}, d), \quad (2.36)$$

where $D(\dot{\mathbf{u}})$ is the kinetic energy:

$$D(\dot{\mathbf{u}}) = \frac{1}{2} \int_{\Omega} \dot{\mathbf{u}}^T \dot{\mathbf{u}} \rho d\Omega. \quad (2.37)$$

In eq. (2.37), $\dot{\mathbf{u}}$ represents the nodal velocities, while ρ is the mass density. For these dynamic cases, we used the implicit Hilber–Hughes–Taylor (HHT) time integration scheme [Hilber *et al.* 1977, Molnár *et al.* 2020b, Molnár *et al.* 2022].

To demonstrate the efficiency of the implemented technique, a Kalthoff and Winkler-inspired [Kalthoff & Winkler 1988] geometry was used. The original geometry was modified by halving the sample’s height and impacting the sample on the entire upper domain. The specimen’s geometry is depicted in Fig. 2.5a. For the elastic phase-field calculation, the material properties of polymethyl methacrylate (PMMA, an amorphous, brittle polymer) were set to $E = 5.5$ GPa, $\nu = 0.3$, $\rho = 1180$ kg/m³, $l_c = 0.4$ mm, and $g_c = 600$ J/m² in an AT1 model. The impactor’s velocity was set according to DIC measurements. Further simulation details were the same as in our recent work [Molnár *et al.* 2022].

The experimental results presented in this document were recorded by Rian Seghir and Julien Réthoré at École Centrale de Nantes (unpublished results) using a rotating mirror high-speed camera.

Fig. 2.5a also shows the crack path (with $d > 0.95$) in the undeformed configuration. It can be seen that the simulation results match almost perfectly with the experimental measurements, not only in the initiation angle but also in the position of the branching. We recently reported similar results for the full Kalthoff experiment [Molnár *et al.* 2022], but without the experimental velocity profile, which is now available and shown in Fig. 2.5b next to the curve obtained from simulations. The correspondence is very good, and both initiation, propagation, and branching are well captured using a simple elastic phase-field calculation.

The ability of the phase-field model to capture the maximum crack propagation velocity was recently attributed to the fact that the elastic stiffness of the material is degraded in the process zone around the crack tip. As a result, the Rayleigh wave speed in the localized zone is lower than in the undamaged material. Ji *et al.* [Ji *et al.* 2022] demonstrated, by

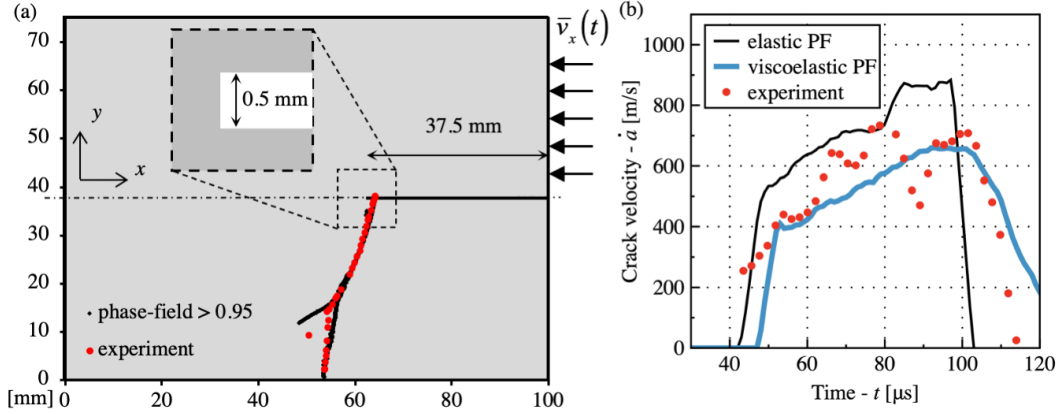


Figure 2.5: Dynamic fracture on demi-Kalthoff sample. (a) Geometry and crack paths. (b) Crack velocity as a function of time.

using different energy degradation functions and process zone shapes, that the maximum crack velocity correlates well with the average stiffness of the process zone in front of the propagating crack.

In reality, PMMA is a viscoelastic material with a static Young's modulus of 3 GPa, which increases to 5.5-6 GPa at high strain rates [Seghir & Pierron 2018]. Thus, if the static modulus is used, the crack velocity exceeds the linear elastic limit posed by c_R . A similar phenomenon was observed in polyurethane experiments [Corre *et al.* 2021]. Therefore, to study dynamic crack propagation in viscoelastic materials, we added a viscoelastic contribution to the potential energy in eq. (2.36):

$$\Psi(\mathbf{u}, d) = \Psi_{el}(\mathbf{u}, d) + \Psi_d(d) + \int_{\Omega} \int_{-\infty}^t \boldsymbol{\sigma}_v(\dot{\boldsymbol{\epsilon}}_v, d) : \dot{\boldsymbol{\epsilon}}_v d\tau dV, \quad (2.38)$$

where $\boldsymbol{\sigma}_v$ and $\dot{\boldsymbol{\epsilon}}_v$ are the viscous stress and strain rate tensors, respectively. The stress components are obtained as $\boldsymbol{\sigma}_v = g(d)\boldsymbol{\eta}\dot{\boldsymbol{\epsilon}}_v$, with $\boldsymbol{\eta}$ containing the stiffness components associated with viscous deformations. For further discussion on the material model and phase-field implementation, we refer to references [Luo *et al.* 2020, Eid *et al.* 2023].

With the viscoelastic formulation, using a static stiffness of $E = 3$ GPa and $\eta = 0.055$ MPa·s for both hydrostatic and deviatoric viscoelastic coefficients, the limiting velocity was accurately recovered, as shown in Fig. 2.5b. The parameters were identified using a Finite Element Model Update scheme on the elastic wave propagation until $t = 40$ μ s.

Furthermore, we found, similarly to Ji *et al.* [Ji *et al.* 2022], that the average tangent modulus in the process zone (the l_c -sized zone around the crack tip) increases at high crack opening rates. This allows the elastic wave, and thus the crack, to propagate faster and branch at a higher velocity [Eid *et al.* 2023].

2.6 Oxidation induced fracture

One of the main advantages of the phase-field technique is its versatility in modeling various physical phenomena. If the energy of a problem can be formulated, and the coupling

between different physics can be established, the variational framework inherently handles the numerical solution.

Interestingly, the phase-field method was not originally developed to model fracture but to describe diffuse interfaces [Cahn & Hilliard 1958]. In this chapter, we demonstrate how we used this method to study crack initiation in zirconium alloys under oxygen diffusion and subsequent phase change (oxidation) in nuclear fuel cladding. This study was motivated by the potential loss-of-coolant accident, which can occur at high temperatures and pressures. In this hypothetical accident scenario in pressurized water reactors, the water evaporates, exposing the cladding to large amounts of oxygen. The only solution to avoid catastrophe is to insert graphite rods to halt the nuclear reaction. However, due to the high internal pressures in the fuel chamber, the cladding deforms in a ductile manner and bloats, leaving no space for the moderators to penetrate the system. Finally, the oxidized outer layer of the cladding becomes brittle and fractures, exposing the environment to dangerous radiation. Thus, in the work of Ethel Djeumen [Djeumen 2022, Djeumen *et al.* 2022], a multi-physics platform was developed to study the elementary mechanisms behind the brittle-ductile transition in zirconium alloys.

The energy functional in eq. (2.7) was enriched by including the energy contribution of the coupled diffusion and phase transformation problem:

$$\mathcal{L} = W_{\text{ext}}(\mathbf{u}, d) - \Psi_{el}(\mathbf{u}, d, \vartheta) + \Psi_{ch}(c, \vartheta), \quad (2.39)$$

where $\Psi_{ch}(c, \vartheta)$ represents the chemical energy, with c and ϑ being two new degrees of freedom: the oxygen concentration and the order parameter. The order parameter represents whether the material is in a metallic or oxidized phase. The chemical contribution can be further divided into chemical free energy [Kim *et al.* 1998] and interface energy contributions:

$$\Psi_{ch}(\vartheta, \nabla\vartheta) = \int_{\Omega} \left[H g_{ch}(\vartheta) + \frac{\alpha}{2} |\nabla\vartheta|^2 \right] d\Omega. \quad (2.40)$$

The structure is similar to the phase-field fracture formulation. Here, H represents the height of the energy barrier, accounting for the free energy penalty of the interface, and α is the coefficient of the gradient term related to the interface energy. The geometric function g_{ch} is a double-well potential [Raabe *et al.* 2004], analogous to $\omega(d)$ in eq. (2.11).

The interface energy and interface thickness can be deduced from H and α [Kim *et al.* 1998, K. Ammar & Forest 2009] as:

$$\begin{aligned} g_{\vartheta} &= \frac{\sqrt{\alpha H}}{3\sqrt{2}}, \\ l_{\vartheta} &= \ln\left(\frac{1-\zeta}{\zeta}\right) \sqrt{\frac{2\alpha}{H}}, \end{aligned} \quad (2.41)$$

assuming the interface region ranges from $\vartheta = 1$ to $\vartheta = 1 - \zeta$, where $\zeta = 0.05$ was chosen for this study.

Furthermore, the potential energy in eq. (2.39) was modified to account for changes in material properties due to phase transformation. Both elastic and fracture properties were altered using a third-order homogenization function [Wang *et al.* 1993]. Additionally, viscoplastic energy dissipation was included to account for creep effects based on Norton's law. The coupling between the different physics was established based on both literature and in-house experiments conducted during the thesis. Using this newly implemented method, we successfully described the brittle-ductile transition observed in experiments [Leistikow & Schanz 1987]. An example is depicted in Fig. 2.6a. The model represents a slice of the cladding cylinder perpendicular to its main axis, with periodic boundary

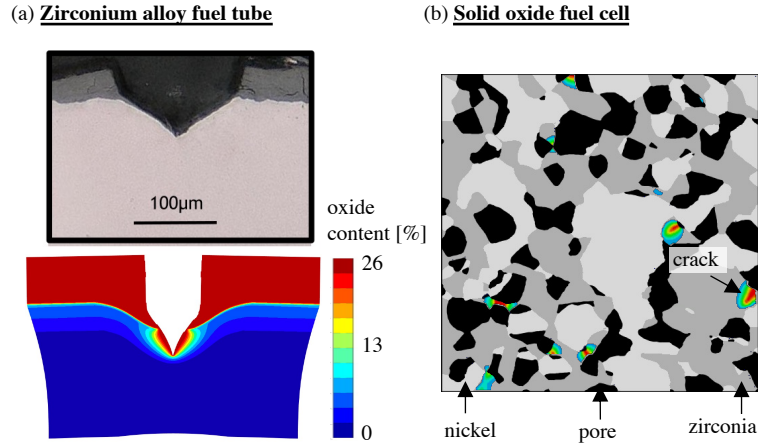


Figure 2.6: (a) Fracture in zirconium alloy fuel cladding. The top image shows experimental observations, while the bottom shows the coupled multi-physics phase-field simulations. The colors represent oxygen concentration at the fractured state. (b) Fracture in solid oxide fuel cells due to volume expansion during oxidation.

conditions applied in both normal and tangential directions. The oxide layer propagates from the top, while the internal pressure (applied at the bottom) gradually opens the crack due to creep relaxation in the metal. As the metal oxidizes and becomes brittle, the crack advances. This model provides professionals in the nuclear industry with a unique tool to understand the limitations of their designs and the extent of potential damage under given pressure and oxidation conditions.

This technique is currently being developed to model fracture in solid oxide fuel cells (SOFCs) [Rorato *et al.* 2023], as shown in Fig. 2.6b. SOFCs are composed of a complex structure of zirconium alloy, nickel, and pores. Repeated charging and discharging of the battery causes oxygen to enter the pores, and nickel atoms diffuse to the surface, forming nickel oxide. This oxidized nickel has a significantly larger macroscopic volume than the metal, exerting substantial deformation on the relatively fragile zirconium, which results in the fracture of the battery structure. This behavior is demonstrated in Fig. 2.6b, where the red areas indicate the fractured regions. The multi-physics platform developed here is relatively easy to calibrate and can be applied to various problems, offering great scientific and industrial potential.

2.7 Concluding remarks

This chapter has explored the critical role of length scales in fracture mechanics, with a particular focus on the interplay between material properties, crack initiation, and propagation. By revisiting Irwin's length in finite fracture mechanics and applying it alongside the phase-field regularization approach, we have demonstrated that the introduction of internal length scales is essential for accurately capturing material failure mechanisms.

The phase-field method's ability to seamlessly bridge the gap between stress-based and toughness-based criteria provides a unified framework for understanding fracture across multiple loading modes. Through a detailed comparison with the coupled criterion, we revealed important correlations between the length scale parameter, l_c , tensile strength,

and crack propagation behavior in both stable and unstable initiation scenarios.

In particular, the chapter offered insights into fracture modes under various conditions, including tensile opening, in-plane shear, and antiplane shear. The introduction of a regularization length scale not only avoids the singularities present in classical fracture mechanics but also successfully models complex phenomena such as echelon cracking under antiplane shear and the size effect in tensile loading.

Moreover, the dynamic fracture analysis demonstrated that without regularization, phenomena like crack kinetics and branching are difficult to predict. The phase-field method, however, captured dynamic crack propagation with impressive correspondence to experimental observations. Its inherent regularization was also shown to be a powerful tool in modeling oxidation-induced fractures, where complex interactions between multiple physical phenomena drive failure.

In conclusion, this chapter has reaffirmed the importance of understanding length scales in fracture mechanics. The phase-field framework, with its flexibility and broad applicability, emerges as a promising approach for capturing the complex behavior of materials under fracture, effectively bridging the gap between theoretical predictions and real-world observations.

Strength and Toughness of Silicate Glasses

The chapter explores the relationship between length scales and mechanical properties in silicate glasses, with a focus on their strength and toughness. Focusing on amorphous silicates, it highlights how compositional variations, such as sodium content, and external factors like pressure, impact elasticity, plasticity, shear banding, and fracture behavior. Through the integration of atomic-scale simulations and continuum modeling, the chapter explores the internal length scales that dictate mechanical responses, offering deeper insights into crack initiation and propagation. Additionally, it emphasizes how regularization methods, such as phase-field modeling, enhance the ability to capture complex phenomena like shear banding and crack propagation in brittle materials.

Associated publications

- [G. Molnár](#), P. Ganster, A. Tanguy, E. Barthel, G. Kermouche, *Densification dependent yield criteria for sodium silicate glasses – An atomistic simulation approach*, Acta Materialia, 111 pp. 129-137, 2016.
- [G. Molnár](#), G. Kermouche, E. Barthel, *Plastic response of amorphous silicates, from atomistic simulations to experiments – A general constitutive relation*, Mechanics of Materials, 114 pp. 1-8, 2017.
- [G. Molnár](#), P. Ganster, A. Tanguy, *Effect of composition and pressure on the shear strength of sodium silicate glasses: An atomic scale simulation study*, Physical Review E, 95, 043001, 2017.

Contents

3.1	Motivation	36
3.2	Elasticity	36
3.3	Densification	37
3.4	Ductile behavior	39
3.4.1	Yield criterion	40
3.4.2	Plastic events	42
3.4.3	Shear bands	44
3.5	Fracture	47
3.5.1	Regularization length	49
3.5.2	Surface free energy and toughness	50
3.5.3	Comparison between methods	51
3.6	Concluding remarks	52

3.1 Motivation

Silicate glasses are widely used in technical applications, particularly where both stiffness and transparency are essential. While these materials are macroscopically brittle, they display ductile behavior at the micron scale [Marsh & Cottrell 1964], a key factor in understanding the origins of brittleness in glasses. However, the plastic response of amorphous silicates presents some unusual characteristics. For example, open-structure glasses like amorphous silica exhibit irreversible volumetric strain when compressed, with densification reaching a saturation point of around 20% under hydrostatic pressures of approximately 20 GPa [Mackenzie 1963, Vandembroucq *et al.* 2008, Deschamps *et al.* 2013, Rouxel 2015].

In technical glasses, additives like sodium oxide (Na_2O) are commonly introduced into silica to modify the glass network, lowering the glass transition temperature and facilitating easier processing. However, the addition of sodium also affects the mechanical ductility. Sodium-rich soda-lime-silicate glasses show reduced densification under hydrostatic compression [Ji *et al.* 2006], with densification occurring at lower pressures [Deschamps *et al.* 2011]. This behavior is due to sodium ions occupying the open network structure, leading to what is often described as "normal glass" behavior, in contrast to the "anomalous" behavior of pure silica glasses, which exhibit unique thermal contraction and plastic densification at small scales.

Simulations play a crucial role in this research, providing detailed insights into the mechanical responses of these glasses and enabling atomic-level analysis of their rearrangement mechanisms. This chapter delves into various aspects of the static behavior of silicate glasses, emphasizing how different length scales influence the transition from atomic structures to continuum material properties.

3.2 Elasticity

Atomic-scale simulations, particularly molecular dynamics (MD), model atoms as concentrated masses, with their interactions represented by non-linear springs governed by empirical potential functions. These functions define the energy state of interactions, and the atomic positions evolve either through explicit time integration (in MD) or energy minimization (in molecular statics) to find equilibrium configurations.

In this study, amorphous silicate glass samples with the composition $x\text{Na}_2\text{O} - (100 - x)\text{SiO}_2$ were prepared by randomly placing atoms within a periodic simulation box. MD simulations were then performed using the LAMMPS software [Plimpton 1995] to equilibrate, quench, and test the samples. Among the various potential functions available for sodium silicate glasses [Tsuneyuki *et al.* 1989, van Beest *et al.* 1990, Pedone *et al.* 2006, Pedone *et al.* 2007], we employed the widely studied van Beest, Kramer, and van Santen (BKS) potential [van Beest *et al.* 1990], following the parameterization by Yuan and Cormack [Yuan & Cormack 2001]. A cutoff function was added to the Buckingham potential to ensure smooth energy and force transitions at the cutoff distance. A short-range repulsive potential was incorporated to prevent atomic collapse at high pressures or temperatures, which is a common issue with the traditional BKS potential. Coulomb interactions were computed using partial charges, with long-range forces managed by the PPPM solver [Hockney & Eastwood 2021] for periodic systems and the Wolf truncation method [Wolf *et al.* 1999] for non-periodic cases. The methodology for sample generation and the potential function are detailed in appendix A.2 and in Ref. [Molnár *et al.* 2016d].

The structural accuracy of the samples was verified using experimental data from neutron scattering studies [Zotov & Keppler 1998, Karlsson *et al.* 2005, Fábíán *et al.* 2007,

[Cormier *et al.* 2011] and local connectivity analyses, such as NMR [Emerson *et al.* 1989, Maekawa *et al.* 1991, Charpentier *et al.* 2004, Naji *et al.* 2015].

Elastic calculations were then conducted by applying small progressive homogeneous deformation steps ($\delta\varepsilon = 10^{-4}$) to the simulation box, followed by energy minimization using the Polak-Ribiere conjugate gradient algorithm to reach static equilibrium. The static approach was chosen over statistical methods [Parrinello & Rahman 1982] due to the absence of thermodynamic equilibrium in the glassy state. In this regime, the system transitions between metastable states driven by mechanical rather than thermal forces.

The global stiffness tensor was calculated, alongside local stiffness properties at different coarse-graining scales to identify where the material transitions from anisotropic to isotropic behavior. Six distinct quasi-static deformations (compressions and shears) were applied to extract the 21 independent elastic moduli [Holzapfel 2001], characterizing the macroscopic mechanical response. The stress-strain relationships revealed minor fluctuations indicative of local microplastic events [Spaepen 1977, Argon 1979, Lemaître & Chaboche 2004, Tanguy *et al.* 2006, Karmakar *et al.* 2010, Mantisi *et al.* 2012], with macroscopic stress was computed by summing the per-atom virial stress [Thompson *et al.* 2009] and dividing this sum by the box volume.

The stiffness components were determined by performing linear regression over small strain increments, by solving the following overdetermined equation system:

$$\mathbf{c} = \text{Arg min}_{\mathbf{c}} (\|\mathbb{M}\mathbf{c} - \mathbf{s}\|). \quad (3.1)$$

relating the tangent moduli to the stresses. The coefficient matrix (\mathbb{M} , size: 36×21) contains the applied strain values. The stiffness components are the unknowns (\mathbf{c} , size: 21×1), and the stress values are the constant terms (\mathbf{s} , size: 36×1). Knowing that the equations are not fully independent, there are always 15 equations that are linear combinations of the others. The relative error (Δ) is determined by substituting the stiffness components into the original equation system and calculating the stress difference between atomic scale and continuum results.

Local elastic properties were computed using a coarse-graining method [Hardy 1982, Goldhirsch & Goldenberg 2002, Goldenberg *et al.* 2007] depicted in Fig. 3.1a. This method offers the advantage of conserving both mass and energy during homogenization. This method allowed for the calculation of local stress, strain, and elastic moduli at different coarse-graining scales. The Gaussian convolution function used for coarse-graining is given by:

$$\phi_{CG}(r) = \frac{1}{w^3\pi^{3/2}} e^{-\frac{r^2}{w^2}}, \quad (3.2)$$

where r is the distance from the observation point to the atom, and w is the coarse-graining width. As shown in Fig. 3.1b, the relative error decreases with increasing coarse-graining width, stabilizing below 3% at $w = 8 \text{ \AA}$, which we define as the smallest length scale where the material can be considered a continuum.

An example of the local shear modulus distribution for $x = 30\% \text{ Na}_2\text{O}$ is shown in Fig. 3.1c, highlighting significant local variations in the amorphous structure despite the macroscopic value of $\mu^M = 24 \text{ GPa}$.

3.3 Densification

Amorphous silica is known to densify significantly under high pressures even at room temperature [Rouxel *et al.* 2010, Deschamps *et al.* 2013]. Pressure-induced densification of

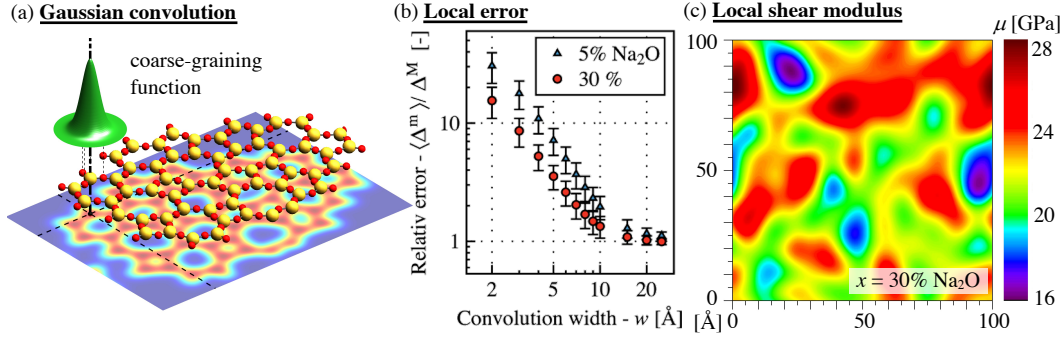


Figure 3.1: (a) Schematic illustration of the coarse-graining method. (b) Relative local error as a function of the coarse-graining scale used. (c) Local shear modulus for $x = 30\%$ Na₂O.

amorphous silica is a process that significantly increases the material's density through the application of high external pressure. Under pressures typically in the range of several gigapascals, the atoms within the disordered silica structure rearrange to reduce free volume, leading to a more compact and dense material. This rearrangement may involve changes in the coordination number of silicon atoms, from the usual four-fold to six-fold coordination, resulting in a tighter atomic packing [Prescher *et al.* 2017]. For example in DAC experiments, it was shown that, the density of amorphous silica can increase from around 2.2 g/cm³ to 2.6 g/cm³. Furthermore, a nonlinear change in mechanical properties was observed like increased elastic modulus or Poisson's ratio upon $\approx 20\%$ densification [Deschamps *et al.* 2014].

To test the hydrostatic behavior of the atomic scale models, simple hydrostatic loading experiments were carried. The permanent volume variations were calculated by compressing the samples isotropically until the desired pressure value was reached, then the deformation was reversed in order to relax the pressure. The difference between the initial and the relaxed volume was compared to compute the permanent volume variation, ε_V^{pl} .

The response was divided into three separate stages. In a first stage, at low pressure, the response was quasi-elastic and the volume change was relatively small. In a second stage, densification was roughly linear with pressure although the details were affected by sodium content. More sodium tends to reduce the densification threshold: $x = 5\%$ Na₂O begins to densify at $p_0 = 3$ GPa while $x = 30\%$ has almost no elastic resistance and plasticity starts at a very early stage ($p_0 = 0.5$ GPa). In a third stage, the linear regime gradually bends over and saturates to a maximum value ($\varepsilon_V^{pl,max}$). The maximum permanent volumetric strain decreases with sodium content. More precisely the yield pressure as a function of permanent volume change can be described using the following sigmoidal curve [Keryvin *et al.* 2014]:

$$p^{y,+}(\varepsilon_V^{pl}) = \begin{cases} \left[-\ln \left(1 - \frac{\varepsilon_V^{pl}}{\varepsilon_V^{pl,max}} \right) \frac{1}{m_1} \right]^{1/m_2} \cdot (p_m - p_0) + p_0 & \text{if } \varepsilon_V^{pl} > \varepsilon_V^{pl,max} \\ \infty & \text{otherwise,} \end{cases} \quad (3.3)$$

where p_0 is the initial yield pressure and p_m , m_1 and m_2 are material parameters.

Qualitatively, the evolution of the plastic properties with increasing sodium content (reduction of the yield threshold and of the permanent volumetric strain at saturation) is in good correspondence to experimental results. Note however that the permanent volumetric

strain at saturation is significantly larger than expected. The maximum volume loss for $x = 30\%$ Na₂O is found at -16%. However, experiments measured a much lower value for window glass around -6% [Ji *et al.* 2006, Deschamps *et al.* 2011]. This discrepancy was probably due to over-minimization in the atomic structure. Nevertheless, as usual with atomistic simulations our aim was not to predict material properties quantitatively, but to observe the atomistic mechanisms and the nature of the mechanical response. Then, the exact values of the response parameters were determined using real life experiments.

3.4 Ductile behavior

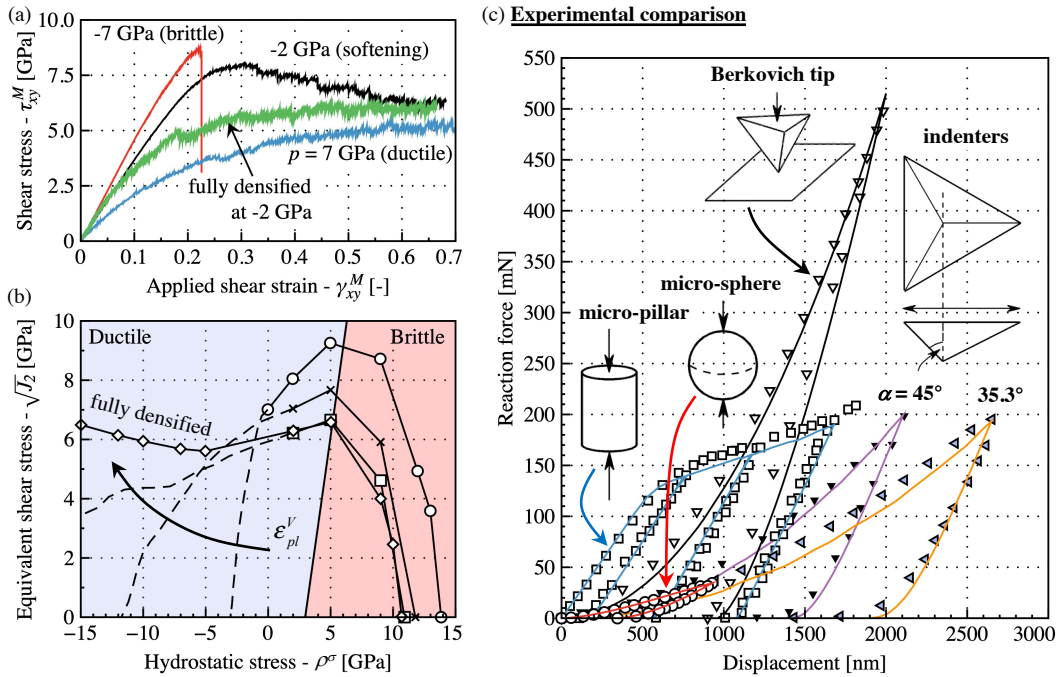


Figure 3.2: Results presented on pure amorphous silica ($x = 0\%$ Na₂O). (a) Shear stress as a function of the applied shear strain for different pressure states for pure silica. The green curve demonstrates the effect of densification. The figure shows the brittle failure at $p = -7$ GPa and the plastic response for the other cases. (b) Maximum yield stress as a function of the hydrostatic stress state and densification for pure silica. (c) Comparison between finite element simulations and experimental measurements (micro pillar compression [Kermouche *et al.* 2016]; micro-sphere compression [Romeis *et al.* 2015]; indentation [Field *et al.* 2003]).

Plasticity in silicate glasses represents a fascinating paradox in materials science, where a material traditionally regarded as brittle at the macroscopic scale, exhibits ductile behavior at the microscopic level [Taylor 1949, Marsh & Cottrell 1964, Romeis *et al.* 2015, Kermouche *et al.* 2016]. This apparent contradiction has sparked significant interest as silicate glasses are known for their glassy, non-crystalline structure while lacking the typical dislocation mechanisms enabling ductility in metals.

In this chapter we will discuss the basic building blocks of ductile behavior in silicate

glasses. Starting with the way we identified the ductile response, how we distinguished it from brittle fracture. Then presenting a novel way to develop yield criteria based on atomic scale results. Analyzing finally the way, how plasticity evolves from the elementary atomistic rearrangements to form a shear band.

Quasi-static shear deformations were conducted at different constant pressure states. The samples were first pre-pressurized then the simulation box was tilted iteratively to apply shear. During the shear deformation all three axial stresses were kept constant by modifying the size of the simulation box iteratively. In this first demonstration the results are presented on smaller a cubic 100 Å sample, which was however large enough to minimize finite size effects, but not large enough to produce a shear band.

In Fig. 3.2a macroscopic Cauchy shear stress is shown as a function of the applied shear strain. All strain measurements in this section are logarithmic Hencky strains. Three different failure modes were distinguished:

- **Brittle:** At high tensile stress (*e.g.*, $p = -7$ GPa), after a maximum shear stress the material loses completely its load-bearing capacity and both shear stress and pressure reduces to zero. This failure mode is characterized by macroscopic crack formation.
- **Ductile:** For higher pressure values, the applied shear strain can be increased without the disintegration of the sample. In this case after either a softening stage (for low pressures) or a monotonic increment (for higher loads), the shear stress enters and maintains a plastic plateau. This way the tangent stiffness reduces to zero, but the pressure and shear stress state is maintained to a non-zero value.
- **Softening:** For intermediate pressure values (*e.g.*, $p = 2$ GPa), after a local stress maximum, the material starts to lose its resistance and enters a non-zero plateau. Interestingly plastic deformation in silica comes with densification thus the material rather than losing its elastic stiffness (associated with damage) becomes more rigid.

Interestingly plastic deformation in silica was associated with densification. In other words, to maintain constant pressure, thus reform the atomic bonds, the sample had to be shrank and the free volume reduced. This phenomenon was shown to create a slightly different atomic structure than hydrostatic densification favoring smaller, 3 member rings. This phenomenon was eventually demonstrated experimentally as well [Martinet *et al.* 2020].

Interestingly, when the sample was densified to its maximum capacity before shear, the softening effect disappeared, although the plateau value remained unchanged, as shown in Fig. 3.2a with green. This was the first sign that density could play a significant role in the failure mechanisms of silicate glasses.

After having identified the elementary shear response, we were able to move forward and develop a yield criterion to describe the homogeneous response of the material.

3.4.1 Yield criterion

In a pioneering work, Schuh and Lund [Schuh & Lund 2003] derived a constitutive relation from atomistic simulations for metallic glasses. Their numerically calculated yield surface compared favorably with experimental results. Since then, many works have been dedicated to measure plasticity in metallic glasses [Schuh & Lund 2003, Lund & Schuh 2003, Lund & Schuh 2004, Lund & Schuh 2005, Shimizu *et al.* 2006], nano-crystalline metals [van Swygenhoven *et al.* 1999, Lund *et al.* 2004] and glassy polymers [Mott *et al.* 1993, Rottler & Robbins 2001]. Amorphous solids in general were stud-

ied [Falk & Maloney 2010, Rodney *et al.* 2011, Xu *et al.* 2014], though an elaborate quantitative description of silicate glasses was still missing.

In the previous sections, we found a strong correlation between densification and yield strength. Therefore, to investigate the pressure and densification dependence of the yield strength, several tests were carried out under combined hydrostatic and deviatoric loading. To evaluate the constitutive relations, permanent plastic strains were calculated as a function of the maximum stress state in various loading/unloading cycles. In practice, the yield stress is often written as a function of plastic strains. Here, by the inverse process, we register plastic strains as a function of applied stresses to determine the hardening functions.

The following protocol was executed to calculate the permanent volume variations (ε_V^{pl}) at a given stress state after loading and unloading. In a first step, the simulation box was deformed hydrostatically ($\sigma_1 = \sigma_2 = \sigma_3$) to obtain the desired pressure value. Then the sides of the box were elongated or compressed separately to apply deviatoric stress at constant pressure and constant meridian angle (step 2) to reach the target load point. During step 3 the direction of the deformation was reversed to reduce the applied deviatoric stress to zero, maintaining the principal stress relations as in step 2. Finally in step 4 the pressure was relaxed to zero. The final box shape was compared to the original one to calculate the permanent volumetric strain as a function of applied stresses. The experiment was carried out for various stress states to map the plastic response of the material accurately.

The envelope in Fig. 3.2b shows the maximum equivalent shear stress (square root of the second invariant of the deviatoric stress tensor) as a function of hydrostatic stress (or negative pressure: $\rho^\sigma = -p$) in the pure shear meridian for pure silica. It can be seen that the maximum values describe a concave failure surface, which appears to violate Drucker's postulate [Drucker 1959] and leads to instability. These observations suggest that the material actually evolves during plastic deformation and that parametrization by some internal variable is necessary.

From the elementary results it is clear that densification lowers the deviatoric strength. To clarify the situation, we have first pre-densified samples using hydrostatic pressure, then performed the same density mapping procedure through combined pressure-shear loading. In Fig. 3.2b with dashed lines, the maximum deviatoric stress is shown as a function of densification. The figure illustrates the transformation of the initial yield surface into the final one: as permanent densification increases, the positive yield pressure increases, the deviatoric yield strength decreases and the yield curve flattens. Most importantly, Fig. 3.2b shows that once the dependence upon density has been explicitly taken into account, the yield surfaces for each given density are convex so that Drucker's postulate is indeed satisfied [Drucker 1959].

The numerical results obtained at the atomic scale were then fitted with an analytical surface and this function was then implemented in a finite element code to be able to compare the atomic scale form to experimental scale results [Molnár *et al.* 2017b]. Based on this evolution, we have proposed a generic shape for the yield surface:

$$\begin{aligned} \frac{p}{p^{y,-}} + \left(\frac{q}{q_c}\right)^b - 1 &= 0 & \text{if } p \leq p^{int} \\ \left(\frac{p-p_h}{p_f}\right)^2 + \left(\frac{q}{q_c}\right)^2 - 1 &= 0 & \text{if } p^{int} < p \end{aligned} \quad (3.4)$$

where q is the von Mises shear stress. In this yield surface, the tensile side of the dome is modeled by an extended Drucker-Prager model. This power law function is closed by an elliptic cap on the compression side. Under the assumption of associated plasticity, densification sets in under pure hydrostatic compression. This model will be subsequently

referred to as DP-cap. The parameters for the DP-cap model are as follows: $p^{y,-}$ sets the tensile strength and b the power law exponent of the extended Drucker-Prager function: for $b = 1$ we find the standard linear Drucker-Prager model while curvature increases with b . Parameter q_c sets the cohesion. The three parameters of the elliptic cap q_e , p_f and p_h are set by the compressive strength $p^{y,+}$ and the requirement that the two component functions meet smoothly at some pressure p^{int} .

For simplicity, we have chosen to work with an associated rule. Thus equation (3.4) will be considered both as yield function and flow potential. This is common practice for microscopic yield criteria [Lambropoulos *et al.* 1996, Schuh & Lund 2003, Kermouche *et al.* 2008, Keryvin *et al.* 2014].

In practice, to model a given amorphous silicate, the material parameters had to be determined. This quantitative evaluation of the numerical parameters – *i.e.*, the calibration of the model – can be performed by comparison between numerical trials and experimental results. To that end, we need quantitative measurements for as many different types of loading cases as possible. However, as stated before, one of the major constraints is the necessity to carry out these measurements at the micron-scale.

This calibration is necessary not only because of the limitations of the potentials used in the atomic scale simulations but also because the calculations are done without thermal activation. Because the experiments are conducted well below the glass transition temperature, it may be assumed that the form of the yield function is unchanged, although the yield strength could actually be lower due to more active plastic zones.

Without entering into details, the densification law, controlling $p^{y,+}$ was set by eq. (3.3), and for the new parameters, c and b we used Berkovich indentation and micro-sphere compression, which showed to cover different parts of the stress space. The determination of $p^{y,-}$ is a bit more difficult to carry out since in this regime there is almost no data available at all. We therefore assume a reasonable value of -5 GPa. This choice turns out to be consistent with the (very scattered) data available [Luo *et al.* 2016]. However, at this stage we have concentrate on the compressive side, as a yield criterion is by definition unable to model brittle failure.

The force-displacement results for the experiments used for calibration and verification are displayed in Fig. 3.2c. It is clearly visible that the correspondence is very good, independent of the geometry. However, we have also emphasized that, due to the increasing complexity of the constitutive models, the simpler data from load-displacement curves under various relevant loading cases must be complemented by a richer data sets, such as strain distribution measurements. Our work also pointed out that experiments in the tensile regime, which are very challenging, would be particularly valuable at this stage. Moreover, even for silicate glasses (*i.e.*, with modifiers), the scarcity of micromechanics experiments significantly limits the accuracy of possible descriptions. Finally, several interesting issues have not been addressed in this model. For instance, softening and the formation of shear bands would have warranted specific developments as well.

3.4.2 Plastic events

In the seventies, Spaepen [Spaepen 1977] and Argon [Argon 1979] have proposed a description of the elementary processes responsible for plasticity in metallic glasses. The description proposed by Spaepen was based on the existence of randomly distributed soft zones, or free volumes, while the description of Argon described low temperature plasticity as a succession of shear dominated dislocation loops identified as shear transformation zones (STZ). Recently, it was shown that the plastic deformation of amorphous systems can be described as a succession of Eshelby inclu-

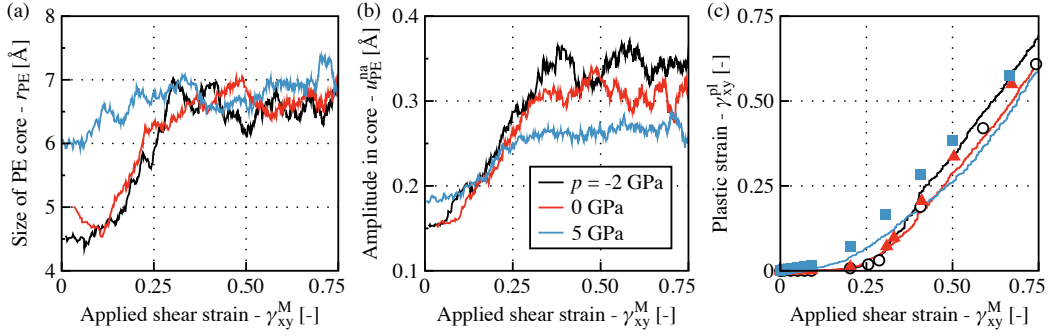


Figure 3.3: Statistics on plastic events in $x = 5\%$ Na_2O content silicates: (a) average size of the PE's core; (b) average amplitude between 10 deformation steps; (c) average cumulated strain in the core of the PE versus the macroscopically measured remaining shear strain.

sions [Eshelby 1957] containing both deviatoric (shear dominated) and compressive (densification) components [Maloney & Lemaître 2004, Tanguy *et al.* 2006, Dasgupta *et al.* 2012, Puosi *et al.* 2014, Nicolas *et al.* 2015, Albaret *et al.* 2016].

To identify the plastic activity [Molnár *et al.* 2017a], the non-affine displacement field is used [Tanguy *et al.* 2002, Weaire & Kermode 1984]. This quantity was shown to highlight the plastic centers that are located precisely at its local maxima as soon as irreversible displacement occurs [Tanguy *et al.* 2006, Goldenberg *et al.* 2007, Tsamados *et al.* 2009, Fusco *et al.* 2014]. The non-affine displacement field $d\mathbf{u}_{na}$ is obtained between two deformation states by subtracting the displacements of the atoms in the affine hypothesis to the real displacements obtained after mechanical equilibrium is reached. It is written:

$$d\mathbf{u}_{na} = d\mathbf{u} - d\boldsymbol{\varepsilon}^M \cdot \mathbf{r}_0, \quad (3.5)$$

where $d\mathbf{u}$ is the atomic displacement obtained from simulations, that compares the atomic positions after energy relaxation to the atomic positions before the external deformation is applied, and $d\boldsymbol{\varepsilon}^M \cdot \mathbf{r}_0$ is the so-called affine part where \mathbf{r}_0 corresponds to the initial position of the atom and $d\boldsymbol{\varepsilon}^M$ is the macroscopic strain step tensor between the deformation states. The non-affine displacement field thus evaluates the atomic displacements occurring during energy minimization. It also corresponds to the deviation from the homogeneous strain field.

To accurately measure the displacements, $d\mathbf{u}_{na}$ was calculated between every 10 load steps (*e.g.*, between the initial and the configuration obtained after 10 load steps, then between the 10th and 20th one, and so on) that is for a strain interval $d\gamma_{xy}^M = 10 \cdot \delta\gamma^M = 0.1\%$.

The non-affine displacements can be used to identify local plastic events (PEs), which control the major part of the irreversible rearrangements in amorphous solids [Argon 1979, Falk & Langer 1998, Tanguy *et al.* 2006]. The PEs were obtained using the method developed by Fusco *et al.* [Fusco *et al.* 2010]. First $d\mathbf{u}_{na}(x, y, z)$ was computed between every 10 load steps then the discrete field was homogenized using a coarse-graining width of $w = 3 \text{ \AA}$. Then the local maxima of this field are identified as individual PEs. Smaller than $d\mathbf{u}_{na} < 0.1 \text{ \AA}$ were neglected because their amplitude is within the numerical precision of the energy minimization scheme.

The size (r_{PE}) of a PE was estimated by looking at the radial decay of the angular averaged intensity of the non-affine field around its local maximum. The values were then fitted with an exponential function: $|\mathbf{u}_{na}| = u_{na}^{\max} \exp(-|\mathbf{r}|/r_{PE})$, where u_{na}^{\max} is the value

at the peak, $|r|$ the radial distance, and r_{PE} measures the radius of PE's core.

The results are summarized for different pressure states for $x = 5\%$ Na₂O in Fig. 3.3. Three stages are clearly visible: (i) a first stage where almost no PE is found; (ii) a second stage where the PEs appear exponentially; (iii) a final stationary stage, where the number of PEs appearing at each strain step is constant, giving rise to a linear strain dependence of the cumulative number of PEs, or constant nucleation rate. The first stage can be considered as elastic (plasticity is negligible); then the material gradually plastifies, and finally the response enters a stationary plastic plateau.

Fig. 3.3a shows the average radius size (r_{PE}) of the plastic event's core as a function of the imposed shear deformation. In all cases, the PE's radius is smaller in the early stage but increases gradually and tends to a stationary value in the plastic plateau. Initially, r_{PE} is clearly pressure dependent. It is enhanced by the pressure. Increasing the pressure from -2 to 5 GPa enlarges the plastic cores by 50% from 4 Å to 6 Å. In the stationary regime, the PE core radius is nearly 6.5 Å and it is only slightly enlarged by pressure but does not depend anymore on composition. After the coarse-graining length, shown in Fig. 3.1b, the average size of the elementary event gives us a second measure for an elementary scale in the material. It can be seen that as in elasticity range of 7 – 8 Å is the minimal size where the material can be considered a continuum. Interestingly a similar cross-over length scale, the Larkin length was found in crystalline materials by Rodney et al. [Rodney *et al.* 2024].

Fig 3.3b shows the amplitude of the non-affine displacement field at the plastic event averaged over all the events in the same strain step. The same kind of stages can be found: after an initially low value, the amplitude increases quasi-linearly and saturates to a stationary regime. Pressure has a significant effect on the amplitude too: increasing the pressure enhances the amplitude in the initial quasi-elastic stage, but the amplitude decreases with pressure in the final stationary plateau. The general trend is thus an enhancement of plastic activity with pressure, combined with slightly larger amplitude events in the early stages of deformation, and then significantly lower amplitude.

Finally, we have showed that plasticity in these simulations are mostly induced by the localized events. When the total strain, computed as the sum of the local deviatoric strain measured in the centers of the PEs, compares quite well with the global plastic deformation measured after unloading the system as shown in Fig 3.3c. We found that the relationship between the non-affine displacement and local shear strain was linear. The equivalent shear strain identified by $\gamma_k^m = \frac{u_{na}}{2r_{\text{PE}}}$ corresponded well to the actual strain value measured in the core of the PE.

3.4.3 Shear bands

In section 3.4, the basics of ductile behavior in silicate glasses were presented. We observed no major collective localization of the plastic events, and the response was well described using local constitutive models. However, as experimentally demonstrated by Gross [Gross & Tomozawa 2008], after a certain length scale and for a given composition, periodic shear bands appear under indentation. This is of course, cannot be modeled using the yield criterion developed in section 3.4.1.

Therefore, in this section, we present atomic scale results on unidirectionally larger samples, in which we were able to observe the formation of a shear band. We analyze the origin and the signature (structural change) of this phenomenon and propose a continuum description to identify the characteristic length originating from the collective motion of individual plastic events to form the shear band.

The simulations were carried out on a sample with dimensions $L_x \times L_y \times L_z = 100 \times 600 \times 100$ Å³, containing approximately 400k atoms. The samples were generated and

verified as discussed in earlier sections. After quenching, shear deformation was applied in the xy plane in an athermal manner until $\gamma_{xy}^M = 0.6$, with incremental steps of $\delta\gamma_{xy}^M = 10^{-4}$. The deformation was performed under a constant pressure of $p = 0$ GPa.

The stress response is displayed in Fig. 3.4a. It can be seen that after a quasi-elastic regime, the material gradually loses its tangent stiffness, and after reaching a maximum peak, it begins to soften, eventually reaching a plateau. When the deformation is reversed, and the stress is unloaded and then reloaded, the softening stage disappears, and the sample perfectly reenters the plateau. This indicates that the structure has been irreversibly changed, and a memory effect remains.

To establish the energy balance we have calculated the external work density by:

$$w_{ext}^M = \int_t \boldsymbol{\sigma}^M : \boldsymbol{\varepsilon}^M dt, \quad (3.6)$$

with $\boldsymbol{\sigma}^M$ and $\boldsymbol{\varepsilon}^M$ being the macroscopic Cauchy stress and Hencky strain tensors respectively. While t symbolizes a pseudo time.

The strain tensor was decomposed into elastic and plastic parts in the traditional manner:

$$\boldsymbol{\varepsilon}^M = \boldsymbol{\varepsilon}_{el}^M + \boldsymbol{\varepsilon}_{pl}^M. \quad (3.7)$$

To calculate the elastic strains, we then used:

$$\boldsymbol{\varepsilon}_{el}^M = \mathbf{C}(\mathbf{t})^{-1} \boldsymbol{\sigma}^M. \quad (3.8)$$

where \mathbf{C} is the elastic stiffness tensor. From this, the elastic energy density can be calculated as:

$$\psi_{el}^M = \int_t \boldsymbol{\sigma}^M : \boldsymbol{\varepsilon}_{el}^M dt, \quad (3.9)$$

and its plastic counterpart as:

$$\psi_{pl}^M = \int_t \boldsymbol{\sigma}^M : \boldsymbol{\varepsilon}_{pl}^M dt. \quad (3.10)$$

Usually in eq. (3.10) $\boldsymbol{\sigma}^M$ is replaced by yield stresses. However, we assumed that if $\boldsymbol{\varepsilon}_{pl}^M$ increases, the stress state should remain on the yield surface. The energy densities are then displayed in Fig. 3.4b.

After a macroscopic analysis, the local kinetics were calculated using the CG technique. The cumulative equivalent plastic shear strain (second invariant) is displayed in Fig. 3.4c. It is clearly visible that plastic deformation localized in a well defined band with an amplitude significantly larger than the macroscopically applied value. Interestingly, after unloading we found that with shear deformation, densification (remaining volume change) increased significantly as well (as shown in Fig. 3.4d). This phenomenon underpins the importance of densification which comes with remaining change in the structure and shear deformation as discussed in Ref. [Molnár *et al.* 2016b].

After unloading, we wanted to determine whether the local strength (the maximum stress it can bear) also decreased in the band, as previously shown in Lennard-Jones glasses by Barbot *et al.* [Barbot *et al.* 2020]. Therefore, we conducted a similar local calculation to Patinet *et al.* [Patinet *et al.* 2016], but with a modification: we left a finite slice of material with a thickness of 20 Å in the y direction free, while the remaining material was

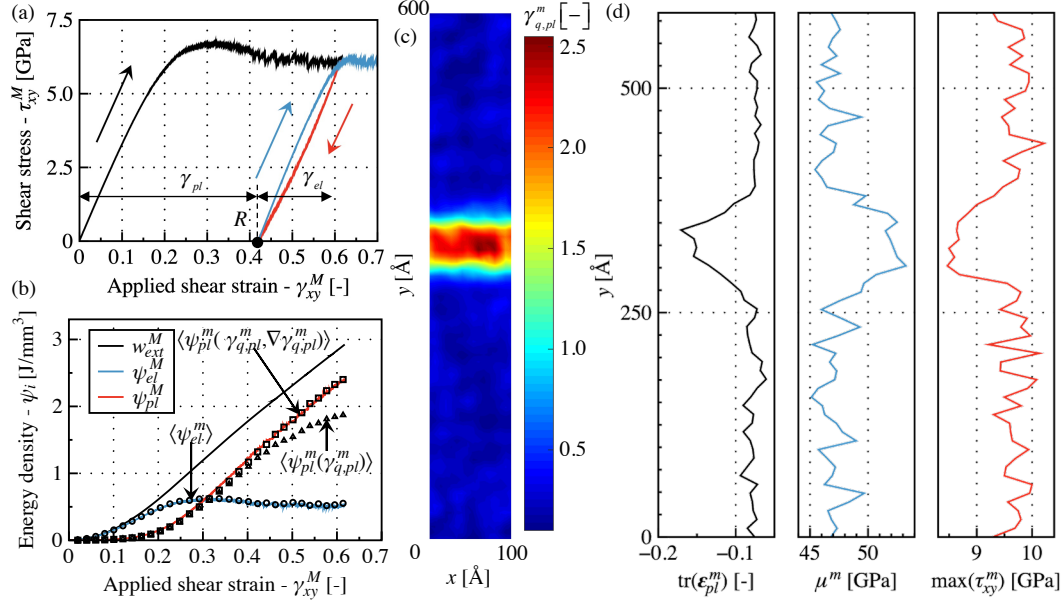


Figure 3.4: Shear band formation in amorphous silica: (a) stress-strain response in loading/unloading and reloading. Arrows indicate the assumed elastic and plastic strain components. (b) Energy density balance calculated from macroscopic stress and strain plotted using solid lines. Symbols display the average energy density values calculated using microscopic quantities. (c) Cumulative plastic equivalent shear strain at $\gamma_{xy}^M = 0.6$ deformation state. (d) Mean local quantities along the y axis after unloading (in strain state R in part a): remaining volume change (densification), shear modulus and maximum shear strength.

deformed in an affine manner. The stress was then calculated from the freely moving slice. The initial slope and the maximum shear stress are plotted in Fig. 3.4d. It can be seen that the stiffness actually increased in the shear band region, which is consistent with the densification, and thus with experimental observations. This highlights that the softening is not related to damage, but rather to structural change.

Additionally, we found that, indeed, in silicate glasses, the local strength in the shear band decreased as well. This phenomenon explains why, during reloading, the shear band appears in exactly the same location at the same stress value. Interestingly, however, it should be noted that the local strength values were consistently higher than the macroscopic strength. This highlights the importance of localization and the need for a non-local description at the macroscopic scale.

Thus, when calculating the local energy densities, we adopted a similar approach to the fracture phase-field method and assumed that the average plastic energy density can be calculated using the following equation:

$$\langle \psi_{pl}^m \rangle = \frac{1}{V} \int_{\Omega} \left[\int_t \sigma^m : \epsilon_{pl}^m dt + l_p^2 q^m |\nabla \gamma_{q,pl}|^2 \right] d\Omega \quad (3.11)$$

where q^m is the von Mises stress, $\gamma_{q,pl}$ is the energy equivalent plastic shear strain and l_p is an intrinsic length scale in shear banding, similar to l_c in fracture. In this case, we identified $l_p \approx 13 \text{ \AA}$.

The elastic energy density was recovered from the average of the local values:

$$\langle \psi_{el}^m \rangle = \frac{1}{V} \int_{\Omega} \int_t \boldsymbol{\sigma}^m : \boldsymbol{\varepsilon}_{el}^m dt d\Omega. \quad (3.12)$$

As shown in Fig. 3.4b, the gradient term was necessary to recover the macroscopic value of the local plastic energies when the shear band became significant.

It is important to note that the gradient plastic model used in eq. (3.11) tends to widen [Jirásek & Rolshoven 2009] as the amplitude of the plastic strain increases, which does not align with what we observed at the atomic scale. A fourfold increase in the maximum amplitude only expanded the shear band by 20%. This suggests the need for a new, potentially incremental, description of the gradient term.

3.5 Fracture

While plasticity and indentation resistance can be important in certain applications, such as electronics and the optical industry, the commonly associated failure mode in silicate glasses is fracture. However, despite the significance of the topic, relatively few papers have focused on atomic-scale modeling of the phenomenon. This may be due to the complexity of the subject, which involves a relatively large number of atoms (leading to long computational times) and challenges in post-processing atomic-scale results to identify the appropriate continuum-scale theory.

The literature mainly focuses on small samples with a thickness of less than 50 Å, which we found to be insufficient to minimize finite size effects. Due to the difficulty of identifying a crack in discrete systems, V-shaped notches are typically used to initiate cracks [Rountree *et al.* 2007, Rimsza *et al.* 2018]. The issue with this method is that the energy release rate associated with a defect that is not sharp is zero. As a result, linear elastic fracture mechanics becomes inapplicable, and a more advanced approach that includes an internal length is required. Nonetheless, many studies still rely on Griffith's original description. Consequently, the results derived from these simulations do not adequately capture crack initiation [Hao & Hossain 2019, Du *et al.* 2021].

Despite these limitations, such studies have successfully demonstrated key atomic-scale phenomena, such as the distinction between free surface energy [Rimsza *et al.* 2017] — used in materials science and surface chemistry — and fracture surface energy [Griffith 1921], which is used in fracture mechanics. However, these simulations have not yet provided a sufficient mechanics description of the results [Rimsza *et al.* 2018]. Therefore in this chapter we will show how to identify diffuse damage at the atomic scale and explain the difference between free and fracture surface energies.

Fracture simulations were carried out on a 3D silica samples, with dimensions $L_x \times L_y \times L_z = 400 \times 300 \times 100 \text{ \AA}^3$, containing $\approx 800\text{k}$ atoms. After periodic bulk heating and quenching, local stiffness was calculated. Periodicity in the xy plane was then suppressed, while periodicity in the z direction was maintained. A rounded incision with a radius of r_c was made to create the initial crack. The atoms were incrementally displaced based on a K-field associated with mode I crack opening on the outer boundaries at a distance of $H_{\text{fix}} = 15 \text{ \AA}$. This distance is larger than the cutoff used for the interatomic potential.

The atomic results were then coarse-grained. As a result, the following continuum quantities were available in both Lagrangian and Eulerian configurations: displacements \mathbf{u} , finite strains $\boldsymbol{\varepsilon}$, Cauchy stresses $\boldsymbol{\sigma}$, potential energy density ψ_{pot} , and mass density ρ .

When choosing the coarse graining width, we found three key aspects that may be influenced by the homogenization process: (i) the elastic behavior, which indicates at what

scale discrete atoms can be approximated as a continuum; (ii) the diffusion width of damage; and (iii) the effect of the free surface on local potential energy.

Our findings indicate that for a minimal length scale of $w = 8 \text{ \AA}$, the elastic strain energy matches the local potential energy. This result aligns well with our previous findings on local elasticity. Additionally, we show that a width of $w = 8 \text{ \AA}$ has minimal impact on damage diffusion. Lastly, we demonstrate that the free surface energy is highly localized on the surface, implying that while varying w may alter the local maximum amplitude, it does not affect the overall sum of the energy change. Detailed explanations are provided below.

Damage is calculated in the Lagrangian configuration following principles of solid mechanics, as most quantities are better defined in the initial state. Only Cauchy stresses needed to be interpolated back from the deformed state because coarse-graining atomic pairs in the initial configuration that were no longer in contact often resulted in locally negative strain energy, which is physically impossible. This interpolation involved displacing grid points of the Lagrangian configuration by their coarse-grained displacements, followed by interpolating stress values from the Eulerian grid to these displaced points.

To account for free surfaces in the Eulerian configuration that appear on the crack lips, a correction multiplier was defined based on the ratio of locally interpolated densities from the deformed configuration to those from the initial configuration. This adjustment compensates for the absence of material at the free surfaces in the deformed configuration, ensuring accurate calculations when parts of the coarse-grained volume are empty.

As amorphous materials lack the ordered structure of crystals, therefore initial local stresses can be found in the quenched material. We assume that these stresses store elastic energy, which is quantified and added to the deformation calculated during loading. The initial strain field can be calculated using linear elasticity as: $\boldsymbol{\varepsilon}_0 = \mathbf{C}^{-1}\boldsymbol{\sigma}_0$, where \mathbf{C} is the local stiffness tensor and $\boldsymbol{\sigma}_0$ is the local initial stress tensor. The initial elastic strain energy density was then obtained by $\psi_{el,0} = \frac{1}{2}\boldsymbol{\sigma}_0 : \boldsymbol{\varepsilon}_0$. We note that this quantity was significantly smaller than the energy from the applied deformation.

To calculate local damage, we used the well-known phase-field formulation:

$$\Psi_{\text{int}}(\mathbf{u}, d) = \int_{\Omega} \psi_{el}(\mathbf{u}, d) d\Omega + g_c \Gamma(d, \nabla d), \quad (3.13)$$

where ψ_{el} is the strain energy density¹:

$$\psi_{el}(\mathbf{u}, d) = (1 - d)^2 \psi_0^+(\boldsymbol{\varepsilon}(\mathbf{u})) + \psi_0^-(\boldsymbol{\varepsilon}(\mathbf{u})), \quad (3.14)$$

with d representing the damage, ψ_0^+ and ψ_0^- representing the tensile and compressive parts of the undamaged strain energy densities, respectively [Molnár *et al.* 2022].

The overall fracture toughness g_c and the fracture surface Γ define the fracture energy in the formulation:

$$\Gamma = \frac{1}{l_c c_\omega} \int_{\Omega} \left(\omega(d) + l_c^2 |\nabla d|^2 \right) d\Omega. \quad (3.15)$$

In this work, we use the AT1 form with $\omega = d$ and $c_\omega = 8/3$. The internal length scale of the phase-field model is denoted by l_c .

From eq. (3.14), the Cauchy stress can be obtained as $\boldsymbol{\sigma} = \frac{\partial \psi_{el}}{\partial \boldsymbol{\varepsilon}}$. Therefore, under the assumption of linear elasticity, we have $\psi_{el} = \psi_{el,0} + \int_{\boldsymbol{\varepsilon}_0}^{\boldsymbol{\varepsilon}} \boldsymbol{\sigma} : d\boldsymbol{\varepsilon} \approx \psi_{el,0} + \frac{1}{2} \boldsymbol{\sigma} : \boldsymbol{\varepsilon} J$, where $\boldsymbol{\varepsilon}$ represents the Hencky strain tensor, and J denotes the determinant of the deformation

¹Capital Ψ is the global value integrated over the whole domain, while small ψ refers to local energy densities.

gradient tensor, accounting for volume variations and $\psi_{el,0}$ is the initial strain energy density after quenching.

We recall that from simulations, the stress, strain, and local stiffness fields are available, allowing the damage to be defined as $d = 1 - \sqrt{\frac{(\psi_{el} - \psi_0^-)}{\psi_0^+}}$.

Fig. 3.5a depicts the damage topology obtained by the atomic scale simulations in the xy plane of the simulation box. Fig. 3.5b shows damage along y at $x = 125 \text{ \AA}$ with a Gaussian fit. Finally, Fig. 3.5c presents the width of the Gaussian function along the crack. The colors represent the maximum damage values.

Finite element model updating (FEMU) was then performed to identify fracture properties, such as the critical energy release rate (g_c) and the internal length scale (l_c). The objective was to update the parameters of a constitutive model so that the results of the phase-field simulation, under appropriate boundary conditions, match as closely as possible the results obtained through molecular scale simulations in the sense of a given norm. We used an AT1 description for the phase-field model with a quadratic degradation function.

The FEMU utilizes the undamaged tensile energy (ψ_0^+) to obtain the local phase-field damage variable. The approach involves iteratively adjusting the material properties, which are considered homogeneous in this case, to minimize the difference between the damage field obtained from the ratio of damaged to undamaged energies (\mathbf{d}_{MD}) and the damage field from finite element calculations (\mathbf{d}_{FEM}).

$$\mathbf{\Lambda} = \operatorname{argmin}[\mathbf{d}_{MD} - \mathbf{d}_{FEM}(\mathbf{\Lambda})]^T [\mathbf{d}_{MD} - \mathbf{d}_{FEM}(\mathbf{\Lambda})], \quad (3.16)$$

with $\mathbf{\Lambda} = [g_c \ l_c]$. The iteration is done by solving the following linear equation system:

$$\mathbf{M}\mathbf{\Lambda} = \mathbf{b}, \quad (3.17)$$

with

$$\begin{aligned} \mathbf{M} &= \left[\frac{\partial \mathbf{d}_{FEM}}{\partial \mathbf{\Lambda}} \right]^T \left[\frac{\partial \mathbf{d}_{FEM}}{\partial \mathbf{\Lambda}} \right], \\ \mathbf{b} &= \left[\frac{\partial \mathbf{d}_{FEM}}{\partial \mathbf{\Lambda}} \right]^T [\mathbf{d}_{MD} - \mathbf{d}_{FEM}(\mathbf{\Lambda})]. \end{aligned} \quad (3.18)$$

The fracture properties were changed until the maximum change in error was smaller than 10^{-6} . The procedure was executed for 20 equally spaced 2D slices in the xy plane along the z direction.

3.5.1 Regularization length

The simulations demonstrate that damage around the crack is diffused rather than localized, extending into the material beyond the immediate crack tip. This diffusion width is notably larger than the coarse-graining width used to transition from atomic to continuum scales, indicating that the CG width is sufficient to capture essential damage features but the actual physical damage spreads further. Specifically, for fully opened cracks, the damage zone varies in width between approximately 16 and 23 \AA , reflecting a non-uniform distribution of damage that suggests its extent may be influenced by local material properties or stress concentrations. This local variability implies that damage diffusion is a local property rather than a purely global phenomenon. Interestingly, the Finite Element Model Updating process produced an internal length scale (l_c) ranging from 12 to 20 \AA , which correlates well with the observed geometric damage width, even though l_c is treated as a global parameter in the model. This correlation suggests that, while damage diffusion is locally variable, the global parameter l_c effectively captures the average behavior of the damage width.

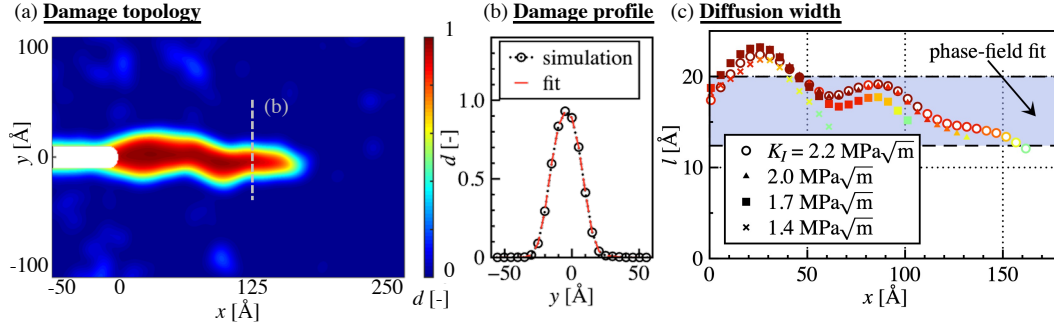


Figure 3.5: Damage field obtained from atomistic simulations: (a) Distribution of damage in the middle plane of the sample. (b) Circles represent the damage profile along the y direction at $x = 125$ Å, fitted with a Gaussian function of maximum height d_{\max} and width l . (c) Variation of the fitted width l along the crack and under different global loading states, color-coded by d_{\max} according to the colorbar. The blue region indicates l_c identified using the FEMU scheme based on the phase-field formulation.

3.5.2 Surface free energy and toughness

The free surface energy was calculated by dissecting (cutting it in half) the samples. The periodic boundary condition in the y direction was suppressed, and mechanical equilibrium was achieved by minimizing the potential energy. The energy difference divided by the newly exposed surface gives 2γ . This quantity was found to be independent of the sample size once it exceeded a certain minimum.

We determined $2\gamma = 2.8 \pm 0.2$ J/m², slightly higher than experimental measurements but within the same order of magnitude (≈ 1 J/m²) [Kimura *et al.* 2015]. This value correlates well with simulations using more sophisticated potentials [Rimsza *et al.* 2017].

In deformed samples, the free surface energy density (ψ_{FSE}) was identified by subtracting the elastic strain energy (ψ_{el}) from the coarse-grained potential energy density (ψ_{pot}). The study's analysis of the free surface energy profile revealed important insights into the localization of energy changes associated with crack formation. The profile width of ψ_{FSE} is observed to be 8 Å, indicating that the energy change is highly localized to the region immediately surrounding the crack. When the convolution is omitted and energy change is instead calculated by averaging over 1 Å slices, a pronounced localized peak emerges. This suggests that the energy change due to the formation of the free surface is primarily a result of surface relaxation due to the loss of atomic connectivity at the crack, rather than a diffusive process that would penetrate deeper into the sample, as is often seen with damage diffusion.

In literature, crack length is often calculated based on an assumed position of the crack tip, either from local density [Rimsza *et al.* 2018] or using a singular Williams series fit [Roux *et al.* 2009]. These methods are not precise enough to identify the crack front in a discrete system, nor can they capture multiple crack fronts. Furthermore, as they assume a sharp crack, they are unable to identify the size of a potential process zone. Analyzing the free surface energy (ψ_{FSE}) provides a more precise understanding of energy changes associated with crack formation. This energy localization is consistent across different sample conditions, making ψ_{FSE} a reliable metric for calculating crack length. The crack length derived from ψ_{FSE} showed good correspondence to phase-field model calculations, validating this method as an accurate alternative to traditional approaches.

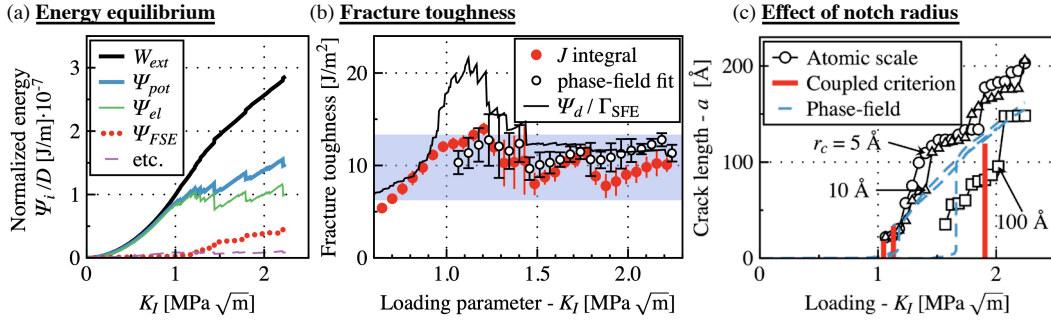


Figure 3.6: (a) Energy balance showing the external work (W_{ext}), the potential energy (Ψ_{pot}), the elastic strain energy (Ψ_{el}) and the free surface energy ($\Psi_{FSE} = \Psi_{pot} - \Psi_{el}$). (b) Energy release rate calculated with various methods. The damage energy (Ψ_d) is obtained by subtracting the elastic strain energy from the external work. The fracture surface from the free surface energy is obtained by $\Gamma_{FSE} = \Psi_{FSE}/(2\gamma)$.

In the context of global energy equilibrium shown in Fig. 3.6a, the energy balance analysis links additional dissipation during crack propagation to damage mechanisms. Under tensile stress, minimal energy dissipation is attributed to plasticity and ring folding, indicating their limited role in overall energy dissipation. The total dissipation, defined as the difference between external work and elastic strain energy, correlates well with fracture processes, with free surface energy being a critical but partial component. The consistency across different methods for calculating total energy dissipation, including FEMU fits and energy balance, highlights the robustness of the analysis. The fracture surface energy calculated post-crack initiation remains consistent across various methods, emphasizing the importance of accurately quantifying damage to understand energy dissipation during fracture as shown in Fig. 3.6b.

However, the study also highlights a significant limitation in the phase-field approach to define g_c . This method integrates both damage-induced toughness and free surface energy, potentially unifying the distinct contributions of these two components. A more refined approach to fracture energy would involve separating free surface energy, treated as a surfacic term, from damage, considered a volumetric term. The original Mumford–Shah functional offers a theoretical framework for this separation, though its implementation presents significant challenges for variational methods. Despite these difficulties, such a distinction could lead to a more nuanced understanding of the fracture process and enhance the precision of energy dissipation models.

3.5.3 Comparison between methods

The comparison between atomic-scale simulations, the coupled criterion, and the phase-field model is shown in Fig. 3.6c for three different notch radii (r_c). The phase-field model was based on the inhomogeneous Young’s modulus and Poisson’s ratio obtained from the atomic-scale model, with a constant toughness of $g_c = 10$ J/m² and an $l_c = 16$ Å. For the calculation, the AT1 form was applied. On the other hand, the coupled criterion was calculated on a homogeneous body. The details of the calculation are presented in Appendix A.1.

As shown in Fig. 3.6c, the crack length for the smaller $r_c = 5$ and 10 Å cases are almost indistinguishable, indicating that the crack initiates once a critical loading is achieved. This

critical loading, when expressed in terms of the global energy release rate ($G_I = \frac{K_I^2(1-\nu^2)}{E}$), aligns with the Griffith-like description, as the crack initiates at $G_{I,cr} \approx 10 \text{ J/m}^2$ for small r_c values.

However, when the notch radius is large ($r_c = 100 \text{ \AA}$), the crack initiates at a higher loading and starts with a large, unstable jump. Unfortunately, this jump varies between methods, as the atomic-scale simulations are highly inhomogeneous, not only in stiffness but potentially in toughness as well. Nonetheless, quantitatively, the results of the three methods show good correspondence, validating the existence of a regularization length below which the crack behaves in a sharp manner.

3.6 Concluding remarks

In this chapter, we explored the strength and toughness of silicate glasses through atomic-scale simulations, focusing on the role of composition, pressure, and internal mechanisms like densification and plastic deformation. By analyzing the elastic, plastic, and fracture behaviors of silicate glasses, we demonstrated the importance of pressure and composition in determining their mechanical response, particularly highlighting how sodium content affects both densification and yield behavior.

The results emphasize a trinity of key mechanical responses in silicate glasses: elasticity, plasticity, and fracture. Elasticity dominates at small deformations, with pressure and composition influencing the material's stiffness. Plasticity emerges at higher strains, particularly through densification mechanisms that are highly dependent on sodium content. Finally, fracture processes were shown to involve complex interactions between atomic-scale damage, surface energy, and crack propagation.

The chapter underscores the utility of advanced simulation techniques, such as molecular statics and the phase-field method, in capturing the intricate mechanical responses of silicate glasses. These methods provide insights into the internal length scales governing both plasticity and fracture, furthering our understanding of how atomic-level phenomena influence macroscopic mechanical behavior.

Furthermore, understanding the transition from localized atomic events to macroscopic material behavior is crucial for improving predictive models. Future work should also focus on refining constitutive models to better capture the interaction between densification and plastic deformation at various length scales.

In summary, to fully capture the behavior of silicate glasses, future research must explore the interplay between densification, plasticity, and damage. Atomic scale simulations, combined with experimental validation and multi-scale modeling, will be critical in driving this understanding forward, leading to more accurate models and innovative solutions for the use of silicate glasses in various applications.

Architected Materials

The chapter examines the mechanical behavior of architected materials, focusing on beam lattices and their optimization. Using both beam theory and Cosserat elasticity, it highlights the impact of microstructure on material properties like stiffness, strength, and fracture toughness. The Cosserat model proved to be more effective in capturing size effects and rotational deformations in lattice structures. Fracture behavior was studied through beam and phase-field models, showing that homogenized toughness values remain constant during crack propagation. An anisotropic phase-field approach was developed to capture directional fracture behavior. Additionally, topology optimization using the Cosserat model yielded accurate, optimized lattice structures, outperforming traditional Cauchy models.

Associated publications

- [G. Molnár](#), N. Blal, *Topology optimization of periodic beam lattices using Cosserat elasticity*, Computers & Structures, 281, 107037, 2023.
- [G. Molnár](#), J. Réthoré, *Fracture Toughness of Periodic Beam Lattices*, Journal of Theoretical, Computational and Applied Mechanics (submitted, 2024) [hal: hal-04793587](#)

Contents

4.1	Motivation	54
4.2	Elasticity of beam lattices	54
4.2.1	Micro-macro kinetics	56
4.2.2	Periodic boundary conditions	57
4.2.3	Constitutive response	58
4.2.4	Cosserat length	58
4.3	Fracture in architected materials	58
4.3.1	Fracture in beam lattices	59
4.3.2	Equivalent fracture toughness	61
4.3.3	Experimental validation	64
4.4	Topology optimization of beam lattices	66
4.5	Concluding remarks	69

4.1 Motivation

Historically, lattice and truss elements have been employed in the construction of large-span structures, such as bridges, roofs, and towers, to reduce mass while simultaneously enhancing global stiffness. Early structural engineers recognized that increasing the spacing between bent components would raise both tensile and compressive forces, thereby increasing the bending inertia quadratically with distance, according to the Huygens–Steiner theorem. This additional bending inertia not only amplified stiffness but also enhanced the overall stability of the structure. Consequently, such designs allowed structures to span considerable distances that would not be achievable with solid forms.

This phenomenon mirrors what is observed in nature [Nepal *et al.* 2023] where structural hierarchies are evident in the microstructure of various load-bearing components. Examples include cork [Chen *et al.* 2010], several diatom species [Jang *et al.* 2013], honeycombs [Mousanezhad *et al.* 2015], and trabecular bone [Lakes 1993, Ritchie 2011]. In each case, smaller beam-like elements form a complex network designed to withstand specific loads.

Recent advancements in additive manufacturing have enabled the fabrication of metamaterials with customized microstructures [Askari *et al.* 2020]. This approach not only enhances stiffness but also strengthens the load-bearing elements at the microscale. As materials approach their microscopic length scale, the size and impact of manufacturing defects diminish, allowing materials that are macroscopically brittle to exhibit ductile behavior [Ritchie *et al.* 2009, Zheng *et al.* 2016, Bauer *et al.* 2016]. This results in lightweight, stiff, and yet resilient materials.

This chapter focuses on the homogenization and optimization of these beam lattices, highlighting the need for more sophisticated models than the conventional anisotropic Cauchy models to accurately describe their behavior.

Here, the superscript \circ^m denotes a microscopic or beam quantity, while \circ^M represents a macroscopic, homogenized Cosserat quantity.

4.2 Elasticity of beam lattices

Main studies on architected materials use the classical framework of Cauchy’s theory, and the methods are thus suitable for large-scale transitions but limited to exhibiting the microstructure size effects. Moreover, such first-order frameworks fail when the scale separation assumption does not prevail (*e.g.*, when topology cells are kinematically coupled as in some compliant mechanisms). Enriched kinematic homogenization schemes are thus needed to efficiently design architected materials and capture local microstructural effects, mutual interactions, non-localities, or instabilities.

One of the first higher-order theories was proposed by the Cosserat brothers [Cosserat & Cosserat 1909]. They enriched the simple Cauchy model with an independent rotation field gradient. This way, the model had 3 displacement and 3 rotational degrees of freedom (in 2D: 2 displacements DoFs and 1 rotation DoF). This theory was the first to define couple stresses and to render the Cauchy stress tensor non-symmetric. Since its first introduction, Toupin [Toupin 1962] formulated the energy density function using the classic displacement and rotation gradient terms. Finally, Mindlin [Mindlin 1963] gave the linearized mathematical theory, serving as the basis of the variational solution.

Since its first introduction, the Cosserat theory has been used in numerous fields, such as granular materials [Li *et al.* 2010], masonry structures [Addessi *et al.* 2010], composites [Lakes 1991], or even human bone [Lakes & Saha 1979, Park & Lakes 1986]. However,

most importantly, it was shown that Cosserat elasticity efficiently captures the effect of the intrinsic length scale in cellular structures [Rueger & Lakes 2016]. The constitutive equations of the model can be written in several forms ranging from a single added constant to Hooke's law [Aifantis 1984] to the entirely redefined stiffness matrix [Zhang *et al.* 2008]. However, one of the main disadvantages of the Cosserat theory is that it has too many material parameters.

The classical description of continuum mechanics is ill-suited to characterize the response of materials with an inhomogeneous microstructure, *i.e.*, a characteristic microscopic length scale. However, the mechanical behavior of architected materials (*e.g.*, lattice structures) is often determined by their specific micro-scale configurations. Therefore, the Cosserat theory (or micropolar elasticity) incorporates rotational degrees of freedom (ϕ) into the mechanical description.

In this work, the Cauchy model is completed with an additional set of equations describing momentum equilibrium in 2D:

$$\begin{aligned} \nabla \cdot \boldsymbol{\sigma} &= \mathbf{0} && \text{in } \Omega, \\ \nabla \cdot \mathbf{m} + \boldsymbol{\sigma} \hat{\boldsymbol{\varepsilon}} &= \mathbf{0} && \text{in } \Omega, \\ \boldsymbol{\sigma} \cdot \mathbf{n} &= \bar{\mathbf{t}} && \text{on } \Gamma_N, \\ \mathbf{m} \cdot \mathbf{n} &= \bar{M} && \text{on } \Gamma_N, \\ \mathbf{u} &= \bar{\mathbf{u}} && \text{on } \Gamma_D, \\ \phi &= \bar{\phi} && \text{on } \Gamma_D. \end{aligned} \quad (4.1)$$

In this equation, $\boldsymbol{\sigma}$ is now a non-symmetric ($\sigma_{xy} \neq \sigma_{yx}$) force-stress tensor, \mathbf{m} is the moment or couple-stress tensor, and $\hat{\boldsymbol{\varepsilon}}$ is the Levi-Civita symbol. The bar symbol represents external forces ($\bar{\mathbf{t}}$), moments (\bar{M}), prescribed displacements ($\bar{\mathbf{u}}$), and rotation ($\bar{\phi}$).

The literature [Forest *et al.* 2001] recounts various ways to define linear elastic behavior. In this paper, we chose to correlate the complete stress tensor to the deformation components using the following model:

$$\begin{bmatrix} \boldsymbol{\sigma} \\ \mathbf{m} \end{bmatrix} = \begin{bmatrix} \sigma_x \\ \sigma_y \\ \sigma_{xy} \\ \sigma_{yx} \\ m_x \\ m_y \end{bmatrix} = \mathbb{C} \begin{bmatrix} \boldsymbol{\varepsilon} \\ \boldsymbol{\kappa} \end{bmatrix} = \mathbb{C} \begin{bmatrix} \varepsilon_x \\ \varepsilon_y \\ \varepsilon_{xy} \\ \varepsilon_{yx} \\ \kappa_x \\ \kappa_y \end{bmatrix}. \quad (4.2)$$

As a result, the first four elements of the stress vector correspond to the Cauchy stress components, however paying attention that in the Cosserat case σ_{xy} and σ_{yx} are not necessarily equal. Finally, the last components are the couple stresses.

Similarly the deformation components can be written as a function of the macroscopic degrees of freedoms, the displacements (\mathbf{u}) in the x and y directions and the rotation around the z axis (ϕ):

$$\varepsilon_x = \frac{\partial u_x}{\partial x}, \varepsilon_y = \frac{\partial u_y}{\partial y}, \varepsilon_{xy} = \frac{\partial u_x}{\partial y} + \phi, \varepsilon_{yx} = \frac{\partial u_y}{\partial x} - \phi, \kappa_x = \frac{\partial \phi}{\partial x}, \kappa_y = \frac{\partial \phi}{\partial y}. \quad (4.3)$$

As a result in 2D, the stiffness tensor takes the form of a 6×6 matrix. However, one of the main disadvantage of the Cosserat theory, that its rigidity is available only for a few types of lattices.

Bottom-up homogenization methods are usually applied to determine the elastic Cosserat constants of lattice structures. Two main approaches exist: (i) the micro-scale is represented by an inhomogeneous Cauchy continuum [Forest & Sab 1998,

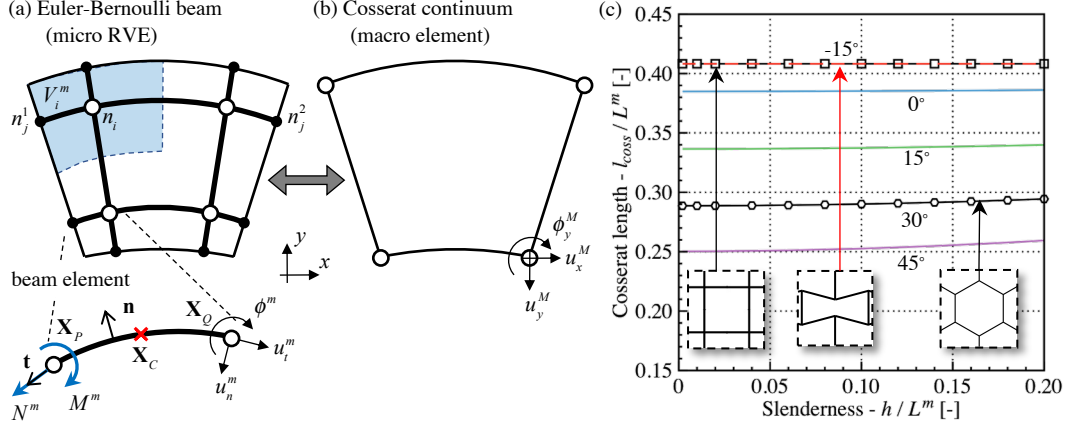


Figure 4.1: Cosserat homogenization: (a) Discrete Euler-Bernoulli beam model; (b) homogenized Cosserat medium. (c) Emerging Cosserat length scale for various structures. The continuous line represents numerical, while symbols denote analytical results [Pradel & Sab 1998, Sab & Pradel 2009]. The angle shows the orientation of the horizontal beams in the hexagonal (and bow tie) lattices.

Forest 1998, Forest *et al.* 2001, Forest 2002], and (ii) the lattices are modeled with either Euler-Bernoulli [Pradel & Sab 1998, Sab & Pradel 2009, Reis & Ganghoffer 2012] or Timoshenko–Ehrenfest beams [Liebenstein & Zaiser 2018]. The important difference is that in the latter case, the rotational degrees of freedom are already present at the microscale. On the other hand, with beam theory, the solid volume fraction cannot be represented.

In order to treat arbitrary microstructures in topology optimization and fracture, a computational homogenization scheme was developed to calculate the stiffness components of Euler-Bernoulli beam lattices. In essence, we made discrete beam calculation on an RVE with periodic boundary conditions, then extracted average stress and strains. Finally calculate Cosserat constants. The details are presented below.

4.2.1 Micro-macro kinetics

The Hill-Mandel energy condition states that the energy of the RVE at the microscale has to be equal to the energy of the element at the macro-scale and can be written as follows for the current problem:

$$\frac{1}{V} \sum_{i=1}^{n_{\text{beam}}} (N_i^m \varepsilon_i^m + M_i^m \kappa_i^m) L_i = \boldsymbol{\sigma}^M : \boldsymbol{\varepsilon}^M + \mathbf{m}^M : \boldsymbol{\kappa}^M + {}^3\mathbf{Q}^M : {}^3\mathbf{G}^M. \quad (4.4)$$

Here, the left side of the equation represents the total internal energy of the RVE shown in Fig. 4.1a, consisting of Euler-Bernoulli beams. While the right hand side gives the energy of the Cosserat medium at the homogenized macro-scale. This assumption allows us to define work conjugate stress measures for the macro scale deformation components. The macroscopic strain tensor $\boldsymbol{\varepsilon}^M$, can be obtained from the RVE using the following equations:

$$\boldsymbol{\varepsilon}_M = \nabla \mathbf{u}^M + \hat{\boldsymbol{\varepsilon}} \frac{1}{V} \sum_{i=1}^{n_{\text{joint}}} \phi_i V_i^m, \quad (4.5)$$

where $\nabla \mathbf{u}^M$ is the displacement gradient tensor, V is the volume of the RVE, n_{joint} is the number of junctions in the RVE, ϕ_i are the rotations of these junction nodes, V_i^m are the volumes defined by the Voronoi cell around each junction (shown in Fig. 4.1a with transparent blue) and $\hat{\boldsymbol{\varepsilon}}$ is the Levi-Civita tensor.

$\boldsymbol{\varepsilon}^M$ and $\boldsymbol{\kappa}^M$ are the exactly the same deformation components, which are used in the Cosserat theory.

Finally, ${}^3\mathbf{G}^M$ represents the second order deformations [Geers *et al.* 2001, Kouznetsova *et al.* 2002] which arise from the finite size of the RVE, but do not contribute to the homogenization. It is calculated by ${}^3\mathbf{G}^M = \nabla \boldsymbol{\varepsilon}^M$.

The work conjugate macroscopic stress measures can be obtained from the RVE beam simulations using the following equations:

$$\boldsymbol{\sigma}^M = \frac{1}{V} \sum_{i=1}^{n_{\text{beam}}} \mathbf{F}_i^m \otimes \mathbf{l}_i, \quad (4.6)$$

where \mathbf{F}_i^m contains the forces acting on a beam element (which is constant along the beam) in a Cartesian coordinate system and \mathbf{l}_i is the so-called beam vector which is the difference between the midpoint between two junctions and a junction point.

The so-called couple stress tensor \mathbf{m}^M can be obtained using the following equation:

$$\mathbf{m}_M = \frac{1}{V} \sum_{i=1}^{n_{\text{beam}}} \left(m_i^m - \left\| \mathbf{F}_i^m \times \frac{1}{2} \mathbf{l}_i \right\| \right) \otimes \mathbf{l}_i, \quad (4.7)$$

where due to the 2D nature of the problem m_i^m is a scalar, therefore it is sufficient to take the length of the second term as cross product is perpendicular to the xy plane.

Finally, the third order stress tensor is defined as:

$${}^3\mathbf{Q}^M = \frac{1}{2} \sum_{i=1}^{n_{\text{beam}}} \left[(\mathbf{F}_i^m \otimes \mathbf{l}_i)^T \otimes \mathbf{X}_{C,i} + \mathbf{X}_{C,i} \otimes (\mathbf{F}_i^m \otimes \mathbf{l}_i) \right], \quad (4.8)$$

where $\mathbf{X}_{C,i}$ are the coordinates of middle point of the beam elements.

4.2.2 Periodic boundary conditions

To apply periodic boundary conditions on the RVE, the difference in the degrees of freedoms are constrained between the opposite boundary nodes using Lagrange multipliers. For example, for boundary nodes j , the differences can be calculated as follows:

$$(\mathbf{u}_j^2 - \mathbf{u}_j^1) = (\nabla \mathbf{u}^M + \mathbf{I}) \cdot d\mathbf{X}_j + \frac{1}{2} {}^3\mathbf{G}^M \cdot (d\mathbf{X}_j \otimes d\mathbf{X}_j) - d\mathbf{X}_j, \quad (4.9)$$

and

$$(\varphi_j^2 - \varphi_j^1) = d\mathbf{X}_j^T \boldsymbol{\kappa}^M, \quad (4.10)$$

with $d\mathbf{X}_j = \mathbf{X}_j^2 - \mathbf{X}_j^1$.

To apply a homogeneous rotation field (ϕ^M), the junction nodes (n_j) were rotated clockwise. This act adds neither first, nor second order (curvature) deformations.

4.2.3 Constitutive response

To calculate the Cosserat rigidity of the lattice structure, the RVE is deformed in six different ways similar to the deformations of the Cosserat model: 2 axial extensions ($\varepsilon_x^M, \varepsilon_y^M$), 2 asymmetric shears ($\varepsilon_{xy}^M, \varepsilon_{yx}^M$), and 2 curvatures (κ_x^M, κ_y^M).

Six different quasi-static deformation cases result in 36 equations. The stiffness matrix is symmetric. Therefore, in 2D, an anisotropic material can be described by 21 unknowns with the Cosserat theory. The six individual equations were rewritten as an overdetermined equation system ($\text{Arg min}_{\mathbf{c}} [||\mathbb{M}\mathbf{c} - \mathbf{s}||]$) relating the Cosserat moduli to the stresses. The coefficient matrix (\mathbb{M} , size: 36×21) contains six blocks with the applied strain values for each deformation case. The stiffness components are the unknowns (\mathbf{c} , size: 21×1): $\mathbf{c} = [C_{11} \dots C_{16} \ C_{22} \dots C_{26} \ C_{33} \dots C_{36} \ C_{44} \ C_{45} \ C_{46} \ C_{55} \ C_{56} \ C_{66}]^T$, and the stress values are the constant terms in six blocks for each deformation case (\mathbf{s} , size: 36×1): $\mathbf{s} = [\dots \sigma_x^{M,(j)} \ \sigma_y^{M,(j)} \ \sigma_{xy}^{M,(j)} \ \sigma_{yx}^{M,(j)} \ m_x^{M,(j)} \ m_y^{M,(j)} \dots]^T$. To solve the overdetermined system QR decomposition was used.

4.2.4 Cosserat length

The Cosserat length is a key parameter in Cosserat elasticity, representing the scale at which the material's microstructural effects become significant. It is one of the smallest length scales which already represents the microstructure in elasticity. Understanding the Cosserat length is crucial for accurately modeling phenomena like size effects, where traditional elasticity theories might fail to capture the nuanced mechanical behavior of materials. There are multiple ways to define this elementary length scale. For simplicity we will take the ratio of the mean bending stiffness and the shear stiffness:

$$l_{\text{coss}} = \sqrt{\frac{C_{55} + C_{66}}{2C_{33}}}. \quad (4.11)$$

Furthermore this analysis serves as a verification for the numerical procedure presented above. Stiffness results are available for equal side rectangular and hexagonal lattices [Pradel & Sab 1998, Sab & Pradel 2009]. Fig. 4.1c shown l_{coss} normalized by the microscopic length of the individual beams L^m as a function of the slenderness of the beams.

It can be seen that the analytic results for both structures are in agreement with the numerical results, validating the technique used to determine the stiffness of the beam lattices.

Furthermore, it is clear the Cosserat length scales linearly with the length of the beams, and effected significantly by the type of the structure. However, the height of the beam plays a minor role in its definition. Furthermore, we found that the length is always smaller than the characteristic size of the micro-scale structure.

4.3 Fracture in architected materials

Even if works in the past few decades have concentrated on predicting the strength of homogenized microstructured materials [Pichler & Hellmich 2011, Kolpakov & Rakin 2020], they struggle to predict the materials resistance in presents of a crack. Due to the theoretical stress singularity in the homogenized model at the crack tip, scale separation cannot be assumed, as the gradient of the stress peak becomes comparable to the scale of the microstructure. While the theoretical concept of homogenized fracture toughness was initially

introduced by references [Roux & Hild 2008, Vasoya *et al.* 2016, Lebihain *et al.* 2021], it has thus far been demonstrated only for Gaussian random microstructure model materials. We asked ourselves, if the unit cell of a periodic beam lattice contains all the information, how can the materials toughness be calculated? As brittle fracture is a unique problem characterized by its dissipative nature, stress localization at the crack tip, and the coupling with the microstructure, it is still a topical debate if intrinsic fracture properties can be defined independent of the macroscopic structural context.

This section seeks to answer whether it is possible to identify a homogenized phase-field model that behaves similarly to the beam lattice in terms of fracture. First, it introduces the mechanical problem under investigation and outlines the objectives of the analysis. Specifically, it compares two approaches to modeling fracture in architected materials: the Euler-Bernoulli beam theory and the phase-field fracture technique.

Fracture resistance is characterized differently by each approach. In the beam model, the microstructure is explicitly represented, with individual beams modeled according to their geometry and material properties. When a beam fractures, it can be discretely identified. In contrast, the phase-field technique treats the material as a continuum, using homogenized material parameters to describe its behavior. Here, cracks emerge gradually as a damage variable diffuses through the material.

For the beam model, the microstructure is defined by parameters such as the height (h^m) and lengths (L^m) of the elementary beams. These structures are characterized by their material properties, which describe stiffness (Young's modulus, E) and strength (the maximum tensile stress they can withstand, σ_c^m).

On the other hand, the phase-field approach is a diffuse damage model that represents the elastic behavior of the material using homogenized continuum stiffness, described here by the Cosserat theory. This theory is essential for capturing the complex behavior of beam lattices, as demonstrated previously [Molnár & Blal 2023]. Fracture initiation and propagation in this model are governed by the critical energy release rate (g_c^M , referred to as toughness) and a regularization length scale (l_c^M), which controls the extent of damage diffusion.

This analysis seeks to answer three key questions: (i) Can we define a unique fracture toughness for a given beam lattice? If so, what parameters influence this toughness? (ii) Can we develop a phase-field continuum model that accurately describes cracks in beam lattices? (iii) How do the predicted fracture patterns compare with experimental observations?

For consistency, this study focuses on a single lattice type: the rectangular beam lattice with equal beam lengths in both directions, analyzed in 2D.

4.3.1 Fracture in beam lattices

Fracture in beam lattices is defined by the failure of individual beams. We consider beams failed, when the maximum axial stress equal or overcomes their elementary strength σ_c^m :

$$\sigma_n^m = \frac{N^m}{A} + \frac{|M^m|}{I} \frac{h^m}{2} \leq \sigma_c^m, \quad (4.12)$$

with N^m and M^m being the normal force and the bending moment acting on the beam. A and I are the area and the bending inertia of the rectangular beam cross section.

In this case, their stiffness, thus the stress which they support goes to zero. Basically, we deactivate the element, only leaving a very small residual stiffness to avoid the singularity of the global stiffness matrix of the model.

The length of the crack (a) is measured by the incremental position of the furthest beam broken. The advantage of this consideration is that it remains consistent with a

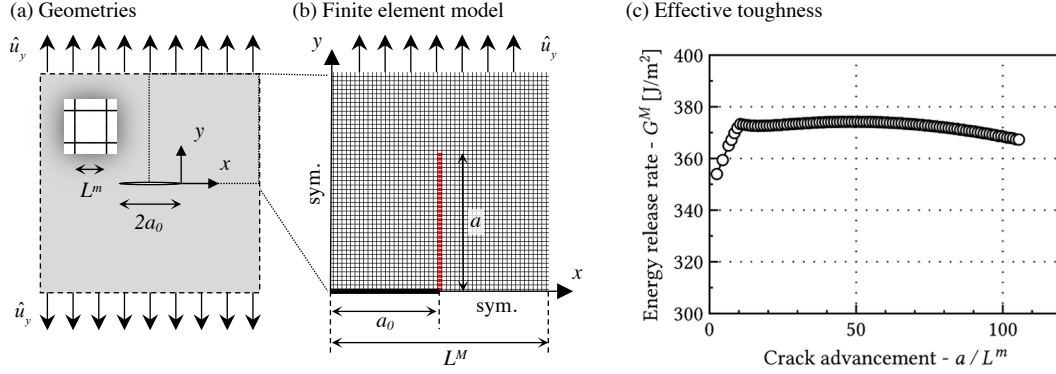


Figure 4.2: (a) Plate with a central crack of length $2a_0$, composed of a rectangular beam lattice with beam dimensions L^m and h^m . (b) One-quarter model of the symmetric geometry with size L^M , with broken beams highlighted in red. (c) Energy release rate G^M as a function of normalized crack advancement.

macroscopic (continuum) approach, where we follow a crack tip. The disadvantage, is that we have trouble following branched cracks and potential crack widening.

Nevertheless, if the crack length is defined, the differential energy release rate (G^M) is expressed by the following energy balance equation:

$$G^M(a + \Delta a/2) = -\frac{\Psi_{\text{int}}(a + \Delta a, P) - \Psi_{\text{int}}(a, P) - \Delta W_{\text{ext}}(P)}{\Delta a}, \quad (4.13)$$

where Ψ_{int} is the elastic strain energy, ΔW_{ext} is the external work, and P represents the applied displacements or external forces on the boundaries. Here, a is the initial crack length, and Δa is the crack increment.

Let us consider a simple problem depicted in Fig. 4.2a. A plate with a $2a_0$ length crack in its middle is subjected to tensile stress on its upper and lower boundaries. While the perpendicular sides are left free to displace. The plate is constructed from a rectangular beam lattice with an elementary beam length of L^m and a beam height of h^m . The beams have a Young's modulus of E and a failure strength of σ^m . As the problem is symmetric, we only model one fourth of the geometry depicted in Fig. 4.2b. The size of the model is taken as L^M with a crack length in the bottom left corner of a_0 . On the left and bottom sides (except along the crack) symmetric boundary conditions are defined in both the displacement and rotation DoFs. The load is applied through displacement Dirichlet boundary conditions on the top. The broken beams are highlighted in red.

Finally, Fig. 4.2c depicts G^M as a function of the normalized crack advancement for a model with $L^m = 5$ mm, $E = 3$ GPa, $h = 1$ mm and $\sigma_c^m = 100$ MPa. The geometry: $a_0 = 25L^m$ and $L^M = 150L^m$ was used. It can be seen that after initiation, the energy release rate changes less than 10%, thus can be considered constant.

We found, that for a given set of structural and material parameters the energy release rate, G^M , remains nearly constant as the crack advances. This invariance suggests that G^M is a characteristic property of the lattice structure itself in stable propagation.

The impact of macroscopic geometry on G^M is minimal, with significant changes only observed when the geometry approaches the scale of the individual beams. This stability of G^M with respect to macroscopic dimensions highlights its role as an intrinsic characteristic of the lattice.

Microstructural and material properties have a more pronounced effect on G^M . The beam height h^m significantly influences G^M , showing a strong linear relationship. In contrast, the slenderness has a smaller effect, which diminishes as its value increases. Material properties also affect G^M : it scales quadratically with the failure strength σ_c^m and exhibits a hyperbolic dependence on Young's modulus E . These results are consistent with theoretical models link Irwin's length (see eq. 2.6) and phase-field studies [Molnár *et al.* 2020a, Molnár *et al.* 2024], suggesting a correlation between discrete microscopic parameters and homogenized phase-field characteristics. The detailed analysis can be found in Ref. [Molnár & Réthoré 2024].

4.3.2 Equivalent fracture toughness

The previous section demonstrated that the energy released in a rectangular beam lattice remains relatively constant with respect to the length of the crack. This result motivated us to define a continuum model capable of reproducing the crack patterns observed in the discrete beam lattice. As the elastic stiffness of the material suggests that the response may be orthotropic, therefore we turned our attention to anisotropic phase-field formulations.

In phase-field simulations, anisotropic can be induced in a hard or soft manner. The hard representation [Nguyen *et al.* 2017] requires a penalty function which acts on the gradient of the damage in the phase field formulations. While in the soft model [Bleyer & Alessi 2018, Scherer *et al.* 2022] introduces a directional dependent g_c^M . The soft model is preferred in our case as it accurately describes the behavior of the unitary cell structure independent of crack length and geometry. While promising, this soft representation has not yet been calibrated to a real cell structures.

In this work, we introduce multiple damage variables (d_i) with directional fracture toughness and length scale values. Thus, the traditional damage energy, introduced in eq. (2.10) for the AT1 formulation, is replaced by the following expression:

$$\Psi_d(\mathbf{d}, \nabla \mathbf{d}) = \sum_{i=1}^n \frac{g_{c,i}^M}{c_\omega l_{c,i}^M} \int_{\Omega} \left[d_i + (l_{c,i}^M)^2 |\nabla d_i|^2 \right] d\Omega. \quad (4.14)$$

With the anisotropic multi-phase-field model, the key is to correctly determine how many damage variables are needed and which variable acts on which stiffness component. In revers, energy stored by the stiffness component will contribute to the crack driving force to induce damage in a given direction.

The undamaged Cosserat stiffness of a rectangular lattice results in a diagonal matrix with constants [Pradel & Sab 1998, Sab & Pradel 2009]:

$$\begin{aligned} C_{11} &= C_{22} = \frac{h^m}{L^m} E, \\ C_{33} &= C_{44} = \left(\frac{h^m}{L^m} \right)^3 E, \\ C_{55} &= C_{66} = \frac{(h^m)^3}{12L^m} E. \end{aligned} \quad (4.15)$$

From the structural configuration of a rectangular grid, it is easy to observe that there are two principal directions. Therefore, we will use two independent damage variables ($n = 2$ in eq. 4.14), where d_1 corresponds to the horizontal grid, and d_2 to the vertical grid direction.

Until this point, we have not discussed how damage variables affect the stiffness matrix. This step is crucial, as it determines which deformation induces which damage. To identify the couplings, we took a representative volume element (RVE) of a rectangular lattice, removed the horizontal beams, and then the vertical beams, before recalculating the Cosserat stiffness using the computational homogenization method discussed in 4.2.

By applying the same procedure on each deformation case, assuming that in each step the $g_{c,1}^M/l_{c,1}^M$ are equal, and normalizing each row, that $\chi_{11} = 0$ and $\chi_{22} = 0$, we can identify χ to be:

$$\chi = \begin{bmatrix} 0 & 0 & 0 & 8 & 2 & 0 \\ 0 & 0 & 8 & 0 & 0 & 2 \end{bmatrix}, \quad (4.22)$$

where each row corresponds to the i^{th} damage variable and each column corresponds to the given member of the stiffness tensor (now diagonal).

From these results it is clearly visible, that shear for example generates a stress peak 3 times larger, than unidirectional extension in the rectangular lattice. This value corresponds exactly to the square root of the ratio $1 + \gamma_{14}$, which associated with the energy difference in the phase-field model between extension and shear.

Of course these parameters would have to be recalculated for a different lattice type, and χ would potentially become longer as matrix \mathbb{C} might have off-diagonal elements as well.

The homogeneous solution calculated using the beam model and the phase-field formulation is compared in Fig. 4.3a for different load angles. It is visible that both methods agree at pure deformations such as $\omega = 0^\circ, 45^\circ, 90^\circ$. This is due to the calibrated constants of χ . When mixed, there is a small difference due to the fact that in the beam model the stresses are summed up, while in the phase-field approach, the energies.

In the phase-field calculation compressive and tensile strain energies are distinguished only for the two axial components. In other words, if ε_x^M or ε_y^M are smaller than 0, their energies do not contribute to the crack driving force, and vice versa the stiffness in this cases are not degraded.

The homogeneous solution helps to identify appropriate ratios for g_c^M/l_c^M . However, to fully calibrate these parameters, an additional test case is required. Typically, in phase-field simulations, one uses a scenario where size effects are minimal (*e.g.*, no defects) and a case involving a sufficiently large crack, as in classical fracture mechanics (Griffith-type cases).

To investigate the impact of initial defect size, the maximum force was recorded at two key points: when the crack initiated and when the sample reached its maximum load-bearing capacity. Fig. 4.3b shows the moment of the first beam fracture with red circles and the final load-bearing capacity with red crosses. The critical loading is normalized using the homogeneous solution:

$$\sigma_{c,y}^M = \sigma_c^m \frac{h^m}{L^m}. \quad (4.23)$$

When $a_0 < L^m$, the critical loading matches the homogeneous solution since the crack is smaller than the beam spacing. As a_0 increases, a power-law behavior is observed in both crack initiation and maximum loading, aligning with linear elastic fracture mechanics.

Thus, by setting l_c^M equal to L^m , the phase-field results closely replicate those observed in the beam model. It is important to note that, due to the gradual appearance of damage in the model, pinpointing the exact loading state corresponding to the first beam fracture is challenging. For the remainder of the analysis, we therefore set $l_{c,i}^M = L^m$. We note that a similar transition as a function of initial crack length was observed in failure lodes experimentally in 3 point bending for cordierite square lattices [Quintana-Alonso *et al.* 2010].

When eq. (4.21), (4.15) and L^m is substituted into eq. (4.20), we get:

$$g_{c,1}^M = \frac{8h^m(\sigma_c^m)^2}{3E}. \quad (4.24)$$

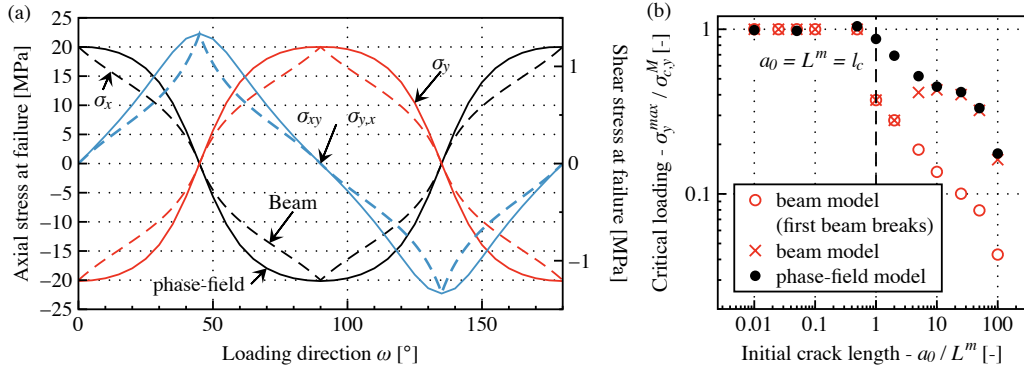


Figure 4.3: (a) Homogeneous solution of the phase-field model compared with the beam results. (b) Critical loading normalized by the homogenized macroscopic strength as a function of the initial crack length.

From this equation we recover the correlations found in the beam simulations. The critical fracture toughness has indeed a quadratic dependence on the tensile strength, a hyperbolic dependence on Young's modulus, and a linear dependence on the beam height. Interestingly, L^m disappears from this correlation.

4.3.3 Experimental validation

The phase-field model was initially calibrated to the beam model for tensile opening, but beam-architected materials are inherently anisotropic and may exhibit different behaviors under varying loading directions. To investigate the primary mechanical couplings present in a rectangular beam lattice, we conducted a series of tests inspired by the Ref. [Ayatollahi & Aliha 2009]. The basic concept involves extending a rectangular plate at two of its opposite corners, which allows for the application of both tensile and shear loading in a tensile testing machine with relative ease.

In the original study [Ayatollahi & Aliha 2009], the load was applied through pinholes in homogeneous materials. However, due to the weakened nature of the material in our lattice structure, a concentrated load could cause the sample to fracture around the point of load application. To address this, we replaced the pinhole with a solid section and applied the load using clamps.

In a rectangular grid, the orthotropic microstructure introduces a third notable direction, in addition to the orientation of the loading and the crack: the orientation of the microstructure itself. To validate our numerical models, we selected four configurations designed to test the relative loading between these directions:

- **Case 1:** Tensile opening with microstructure parallel to the crack,
- **Case 2:** Shear opening with microstructure parallel to the crack,
- **Case 3:** Shear opening with microstructure oriented at 45° to the crack,
- **Case 4:** Tensile opening with microstructure oriented at 45° to the crack.

These elementary cases are illustrated in the different rows of Fig. 4.4.

The experimental samples were cut from 5 mm thick polymethyl methacrylate (PMMA) sheets using a laser cutter. The microscopic unit spacing was chosen to be $L^m = 5$ mm, with

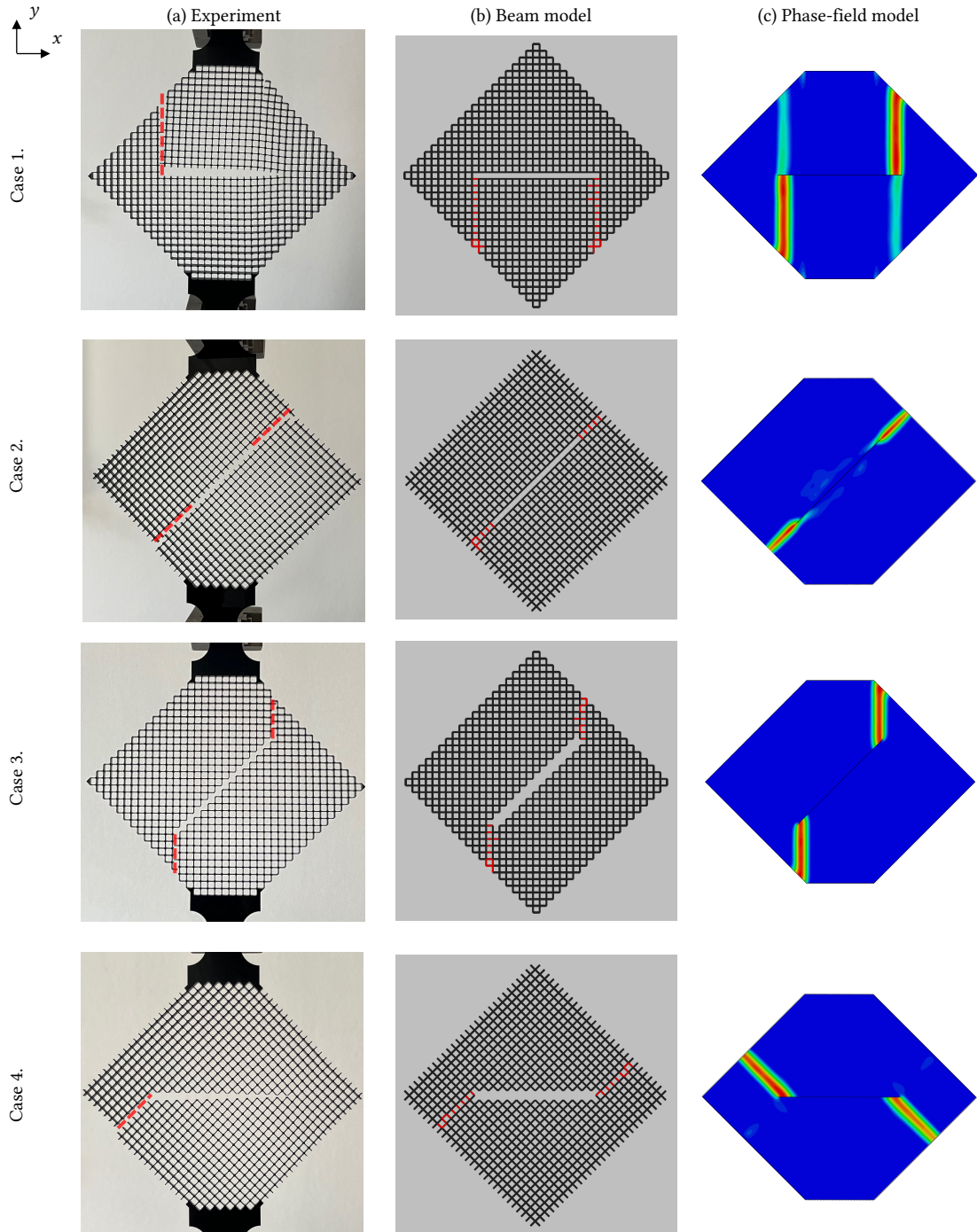


Figure 4.4: Comparison between experiments and simulations. Red highlights the cracks.

a beam height of $h^m = 0.66$ mm. The macroscopic size of the samples was $L^M = 141$ mm. Prior to the experiments, a series of numerical tests were conducted to determine the appropriate length of the clamping zone. The clamping zone length and the initial crack length were carefully set to ensure that fracture initiation occurred at the initial crack. If the clamped zone was either too small or too large, the crack tended to initiate at the edges of the clamped zone rather than at the intended location. Consequently, we selected a clamped width of $L_c = 10L^m = 50$ mm and an initial crack length of $2a_0 = 18L^m = 90$ mm.

The results from these tests are displayed in the first column of Fig. 4.4, with the cracks highlighted in red.

To replicate the asymmetric crack initiation observed in the experiments, the tensile strength and fracture toughness in the numerical models were varied by 5%. The results from the Euler-Bernoulli beam model are shown in the second column of Fig. 4.4, while the corresponding phase-field simulations are presented in the third column.

The results from all models exhibit coherence and agreement, with the crack consistently favoring the direction of the original microstructure. This behavior aligns with expectations, as the shear contribution (third and fourth columns of eq. 4.22) is the most significant factor influencing crack propagation.

Our analysis demonstrates that both simulation techniques accurately represent physical reality and can be used as predictive tools for modeling fracture in lattice structures.

4.4 Topology optimization of beam lattices

Advanced manufacturing processes now allow the development of products with optimized properties by modifying their shape or topology. Topology optimization provides a mathematical framework to optimize material structure, *i.e.*, the spatial distribution of material within a design domain. After defining a cost function, sensitivity analysis provides an updating scheme for design variables, allowing for the optimization of various parameters like compliance, stress, and displacement. These optimization problems, modeled as constrained partial differential equation design problems, require both optimization solvers and numerical discretization schemes (usually finite element methods).

In practice, two types of solvers are used: (i) meta-heuristic approaches that rely on multiple cost function evaluations, and (ii) gradient-based solvers that use the adjoint state method to compute the derivative of the cost function. Among topology optimization techniques, the density-based Solid Isotropic Material with Penalization (SIMP) method is widely used. It defines density variables at each element of the finite element mesh, using a power law to penalize intermediate densities, resulting in optimized structures with solid and void regions. The correct choice of penalization parameters is crucial for achieving optimal results, as explained by Bendsøe and Sigmund [Bendsøe & Sigmund 1999].

One challenge in SIMP is checkerboard patterns, where alternating void and solid elements emerge. This issue can be mitigated using filtering techniques, such as density filters or sensitivity filters, which help reduce mesh dependency [Bourdin 2001]. Another class of methods is based on level-set functions [Sethian 1996], which represent void-solid boundaries and evolve based on shape or topological derivatives to achieve optimized designs [Jackowska-Strumillo *et al.* 1999].

Recent manufacturing advancements have enabled the design of materials with complex, small-scale topologies. Multi-scale topology optimization has emerged to handle these designs, combining macro and micro optimization techniques, with microstructures influencing the overall material behavior. While traditional methods rely on periodic homogenization,

Most studies focusing on the topology optimization of the Cosserat medium use ficti-

tious material parameters, whereas papers presenting the optimization of lattice structures calculate only the Cauchy coefficients [Watts *et al.* 2019]. A comparative analysis using real microstructures and a homogenized second-order continuum was missing.

Periodic beam lattices were known to behave as the Cosserat continuum when properly homogenized. Due to the discrete network of the joints, an independent rotation is needed to properly mimic their behavior. This is confirmed herein by topology optimization.

We presented a new method [Molnár & Blal 2023] to optimize the topology of slender lattice structures with small local volume fractions. We compared the optimal topology of discrete Euler-Bernoulli beam lattices to topologies obtained using the Cosserat theory. The local stiffness was calculated based on real geometrical properties, such as the beam height or the slenderness. We finally highlighted the importance of the enriched model in the optimization of lattice structures and presented optimal microstructures for a variety of macroscopic mechanical problems.

We chose to use the algorithm published by Sigmund [Sigmund 2001] and replaced the arbitrary design variable with the height of the beams. Among its advantages, the modified algorithm is easy to implement, robust and converges rapidly. Despite that Bendsøe and Sigmund [Bendsøe & Sigmund 1999] showed that, for the SIMP method, the cubic penalty function is physically permissible, we decided to use the constitutive analytic relations.

The overall aim of the topology optimization procedure is to keep the compliance of the model at a minimum by minimizing the potential energy as a function of the local design variables:

$$\mathbf{h} = \text{Arg min}_{\mathbf{h}} \left\{ c(\mathbf{h}) = \frac{1}{2} \mathbf{U}^T \mathbf{K} \mathbf{U} = \frac{1}{2} \sum_{e=1}^N \mathbf{u}_e^T \mathbf{k}_e(h_e) \mathbf{u}_e \right\}. \quad (4.25)$$

This was done by respecting the equilibrium constraint:

$$\mathbf{K} \mathbf{U} = \mathbf{F}, \quad (4.26)$$

and the volume constraint:

$$\frac{V(\mathbf{h})}{V_0} = \hat{\rho}, \quad (4.27)$$

with lower and upper bounds on the design variables (beam heights):

$$0 < \mathbf{h}_{\min} \leq \mathbf{h}_e \leq \mathbf{h}_{\max}. \quad (4.28)$$

In eq. (4.25), c is the total potential energy, \mathbf{U} and \mathbf{u}_e are the vectors of the global and elementary degrees of freedom (translation, rotation), \mathbf{K} and \mathbf{k}_e are the global and elementary stiffness matrices, N is the number of finite elements in the design domain and \mathbf{h} is the vector containing the elementary design variables (h_e). In our case, this is the height of the beam cross sections. In this paper, we assume rectangular beam sections with a unitary thickness in the out-of-plane (z) direction. In the equilibrium equation (4.26), \mathbf{F} is the global force vector, V is the total volume of the model, V_0 is the volume of the design domain, and $\hat{\rho}$ is called the relative density or prescribed volume fraction. The optimality criterion method [Bendsøe 1995] with a sensitivity filter [Sigmund 1997] was utilized to update the design variables for a given equilibrium problem.

Fig. 4.5a depicts the geometry of the optimization problem. In this section, a cantilever geometry of length $L_x = 100$ and height $L_y = 50$ was chosen. The concentrated force (F) applied at the end was set to 10^{-3} . In the continuum model the finite element meshes were chosen homogeneously. Both translational and rotational degrees of freedom were constrained on the nodes on the left side.

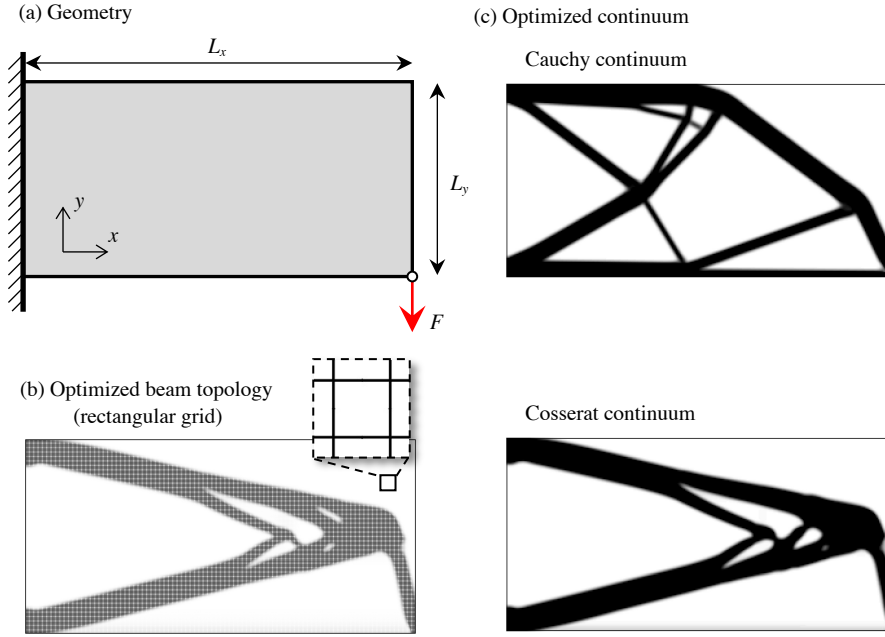


Figure 4.5: Optimized topology of a cantilever: (a) geometry ($L = 100$, $H = 50$), (b) optimal topology using the beam model for $\hat{\rho} = 0.12$ ($r_{\min} = 1$); (c) Continuum models.

For a beam structure, the volume constraint, defined in eq. (4.27) can be expressed by summing up all the individual elements and dividing the sum by the overall area of the design domain:

$$\hat{\rho} = \frac{V(\mathbf{h})}{V_0} = \frac{\sum_{e=1}^N h_e l_e}{LH}, \quad (4.29)$$

where V_0 is the total volume of the design domain, l_e represents the individual length of the beams, and h_e is their height. There are N beams in the structure. In this case, h_e , The design variable has a geometrical significance wherefore its bounds can be defined as:

$$0 < h_{\min} \leq h_e \leq h_{\max}, \quad (4.30)$$

with h_{\min} as a lower bound responsible for numerical stability ($h_{\min} = h_{\max}/5000$), and h_{\max} as an upper bound:

$$h_{\max} \leq \frac{V_0}{N} \cdot \sum_{i=1}^N l_i. \quad (4.31)$$

The characteristic quantities, upper bounds, and the correlation between local volume fraction and beam height are summarized in our recent paper [Molnár & Blal 2023].

Fig. 4.5b shows the optimization results of a rectangular lattice modeled using Euler-Bernoulli beams, while part (c) using Cauchy continuum with SIMP and Cosserat continuum based on the beam heights as internal variable.

When employing the Cauchy description, the design variable was penalized using a cubic function, and the maximum value of the design variable was limited to 0.4, which corresponds to the volume ratio of the rectangular grid RVE when $h_e = l_m/5$. It can be clearly seen that Cauchy's description with the SIMP technique is unable to correctly determine the optimal topology. However, the Cosserat continuum gives not only qualitatively good correspondence, but quantitative agreement. The maximum difference between the deflection values was 2.16%, which was within the precision of the built models. Furthermore, we observed a tendency to favor thicker beams.

Further study included three microstructures: square, hexagonal, and reinforced honeycomb lattices.

In the square lattice, the homogenized stiffness is orthotropic, meaning the material properties differ along the two principal beam directions. Because there is no interaction causing contraction in one direction when extending in another, the Poisson's ratio is zero. The study explored how local and global volume fractions impacted the optimal topology of the lattice, demonstrating that increasing the local volume fraction decreased maximum deflection. The beam model and the Cosserat model yielded nearly identical topologies, although they differed significantly from those produced by traditional Cauchy continuum.

For the honeycomb lattice, homogenization results in an isotropic response with a Poisson's ratio between 0.3 and 0.5, depending on slenderness. This structure's optimal topologies closely resembled those obtained using the SIMP method. The study examined how varying the filter width affected the topology and maximum deflection. It found that larger filter widths increase displacement, but the Cosserat and beam models still agree, except when filtering is turned off.

In the reinforced honeycomb lattice, a traditional hexagonal structure is strengthened with a triangular grid, which adds normal rigidity. The homogenized stiffness remains isotropic with a Poisson's ratio of around 0.3 to 0.34. Structures with different beam lengths were created to test the effect of micro-length scales, showing that micro-length did not significantly affect the optimal topology.

Overall, the study demonstrates that the Cosserat model effectively captures the mechanical response and optimal topologies of beam lattice structures. The findings suggest that depending on the design problem, the optimal lattice structure can be chosen using Cosserat elasticity.

4.5 Concluding remarks

In this chapter, we explored the mechanical behavior of architected materials, particularly beam lattices, and their potential for optimizing structural performance. By applying both beam theory and Cosserat elasticity, we demonstrated how the microstructure significantly influences material properties such as stiffness, strength, and fracture toughness. The analysis showed that the Cosserat theory, with its ability to incorporate rotational degrees of freedom, is a more suitable model for capturing the size effects and complex deformation behaviors present in lattice structures.

We also addressed the fracture behavior of beam lattices, comparing discrete beam models with continuum phase-field models. The results revealed that the fracture resistance in beam lattices can be effectively characterized by homogenized toughness values, which remain relatively stable throughout crack propagation. Furthermore, we developed an anisotropic phase-field approach to capture directional fracture toughness, showing agreement with beam simulations.

Topology optimization played a key role in the chapter, where we demonstrated that

using the Cosserat continuum for optimizing lattice structures yields more accurate and realistic results compared to traditional Cauchy models. The optimized topologies not only minimized compliance but also reflected the true mechanical behavior of the underlying microstructure.

Overall, the findings emphasize the importance of using enriched models like Cosserat elasticity for accurately predicting and optimizing the mechanical performance of architected materials.

Conclusion and Perspectives

In this manuscript, I have demonstrated six major results that contribute to a deeper understanding of fracture mechanics and material behavior. These findings highlight key advancements in the modeling and analysis of fracture processes, as well as the implications for designing fracture-resistant materials. The following chapter summarize the most significant outcomes of this study:

1. We have shown that the material length scales, such as Irwin's length and the phase-field length, differ from the lengths that emerge in cases involving complex geometries.
2. We have shown that limiting crack velocities can be correlated to the average stiffness around the crack tip.
3. We have developed and calibrated complex, densification dependent yield criteria for sodium silicate glasses.
4. We have shown that diffuse damage establishes the difference between free and fracture surface energies.
5. We have established that periodic beam lattices have a unique fracture toughness based on the elementary structure and the materials tensile strength.
6. We have demonstrated that the Cosserat theory is necessary and sufficient to optimize beam structures.

The work presented in this manuscript delves deeply into the role of length scales in material failure, using a range of advanced models and methods to better understand fracture mechanics across multiple scales. From atomic-level simulations to continuum-scale models, the work has illustrated how length scales fundamentally influence crack initiation, propagation, and the overall mechanical behavior of materials. The findings are particularly relevant in addressing the limitations of classical fracture mechanics, which often fail to capture the full complexity of material behavior in modern engineered systems.

This research serves as a unifying framework that bridges diverse aspects of fracture mechanics, linking theoretical constructs, numerical models, and material-specific phenomena. By focusing on the critical role of length scales—from atomic dimensions to macroscopic structural features—this study provides a cohesive perspective on material failure that transcends traditional disciplinary boundaries. The integration of phase-field methods, atomic-scale simulations, and continuum theories reflects the interconnected nature of fracture processes, offering a holistic view that encompasses both fundamental mechanisms and practical applications. The common thread throughout these contributions is the emphasis on understanding and leveraging length scales to resolve the complexities of crack propagation, energy dissipation, and structural optimization. By uniting distinct approaches under a shared analytical framework, this work not only advances the theoretical foundations of fracture mechanics but also lays a pathway for designing resilient materials and structures tailored to the demands of modern engineering challenges.

A key contribution of this work is the detailed exploration of phase-field models and their ability to regularize fracture mechanics problems. By introducing a length scale parameter, the phase-field approach effectively bridges stress-based and energy-based criteria for failure, allowing for a more nuanced understanding of crack behavior. The work presented here goes beyond traditional models by considering dynamic fracture scenarios, as well as multi-physics interactions, such as oxidation-induced failure. These extensions of the phase-field method underscore its versatility and potential as a powerful tool in both theoretical studies and practical applications.

Another significant aspect of this work is the examination of the fracture behavior in silicate glasses, particularly how composition and external pressure influence the mechanical properties of these materials. Through atomic-scale simulations, this thesis demonstrated the critical role of sodium content in modifying the ductility, densification, and fracture toughness of silicate glasses. These findings are particularly valuable in industries that rely on glass materials for high-strength applications, as they provide a deeper understanding of how to tailor glass compositions to improve performance under stress. Additionally, the research highlights how fracture toughness in these materials is influenced by atomic-level mechanisms, providing a clear pathway for optimizing their mechanical properties.

The investigation of architected materials, particularly beam lattice structures, further emphasizes the importance of length scales in determining material behavior. The research presented shows that traditional Cauchy models are often insufficient to capture the complex deformations and size effects in architected materials. By employing Cosserat elasticity, this thesis provides a more accurate framework for understanding and optimizing the mechanical performance of these structures. The use of topology optimization, in conjunction with enriched continuum models, demonstrated how architected materials can be designed to minimize compliance while maintaining robustness. This is a critical insight for the development of lightweight, high-strength materials in modern engineering applications.

One of the overarching themes of this thesis is the importance of coupling different theoretical approaches to capture the full complexity of fracture mechanics. By comparing the phase-field approach with the coupled criterion, the research demonstrates how multiple fracture modes—tensile, shear, and antiplane—can be accurately modeled to reflect real-world behaviors. This is especially relevant in the context of dynamic fracture, where the interaction between crack speed, branching, and material strength poses significant challenges. The findings show that the introduction of an internal length scale, such as in the phase-field method, is essential for accurately modeling the transition between stable and unstable crack propagation.

In conclusion, this work provides a comprehensive investigation into the role of length scales in material failure, offering new insights and advanced models to better predict and understand fracture behavior. By integrating theoretical models, numerical simulations, and atomic-scale analysis, the research has demonstrated the critical role of internal length scales in governing material performance. These findings have important implications for the design and optimization of materials in a wide range of engineering applications, from high-performance glasses to architected lattice structures. Looking forward, the continued development and refinement of these models, along with their experimental validation, will be key to advancing the field of fracture mechanics and material's science.

Perspectives

In this section, we explore various perspectives on the future directions of research in non-linear fracture mechanics, building on the findings of this study. While significant progress

has been made, several key areas remain unexplored. Specifically, we have identified three major directions that warrant deeper exploration: (i) the experimental identification of the regularization length scale or process zone shape, (ii) the design of novel material architectures engineered for superior fracture resistance, and (iii) the development of innovative glass compositions with enhanced fracture resistance.

Experimental observation of l_c — The first major challenge lies in the experimental identification of the regularization length scale or process zone shape, which is critical for the accurate application of phase-field models in fracture mechanics. While these models have proven effective in regularizing fracture problems, extending their application to more complex material systems, such as those with heterogeneous microstructures or multiphysics interactions, demands further refinement. A key limitation is the current lack of experimental validation, which is necessary to ensure that these models accurately reflect real-world fracture behavior.

To address this, future research should prioritize several key approaches. First, computed tomography imaging of echelon cracks in antiplane shear offers a promising method for directly visualizing complex fracture geometries, providing insights into the regularization length scale. This technique allows for the precise observation of the process zone in challenging fracture scenarios.

Additionally, high-resolution digital image correlation (DIC) can be used to capture detailed displacement fields around fracture zones. Traditionally, the region near the crack tip has been excluded from analysis due to deviations in measured displacements from the singular assumptions of the William's series. However, by applying non-singular methods, such as those proposed by Bažant & Beissel [Bažant & Beissel 1994], we can more accurately fit these displacement fields and gain deeper insights into the shape and extent of the fracture process zone. Performing this analysis across various geometries would help determine whether the size and shape of the process zone are intrinsic material properties or influenced by structural geometry.

Furthermore, integrating these experimental techniques with phase-field simulations presents a significant opportunity for future advancements. By employing finite element method updating (FEMU) that incorporates both phase-field models and real-world experimental data from DIC, we could improve the accuracy of fracture predictions. This integration allows for continuous refinement of simulations, aligning computational models more closely with observed experimental behavior, ultimately enhancing the predictive power of phase-field models in complex material systems.

Creating new, fracture-resistant material architectures — Building on the insights from this study, future work will focus on designing novel material architectures through the topology optimization of meso- and microstructures. This research holds significant industrial potential, particularly in sectors like aerospace, automotive, energy storage, and defense, where the demand for lightweight, fracture-resistant materials is critical. The development of these advanced materials could lead to considerable weight reductions without compromising structural integrity, offering substantial benefits in terms of energy efficiency and sustainability.

To advance the development of fracture-resistant metamaterials, future research will focus on three key aspects: homogenization, optimization for toughness, and dehomogenization/rendering (as illustrated in Fig. 5.1). Homogenization will seek to transition from detailed microstructural models, such as beam lattices, to simplified continuum descriptions that accurately capture essential mechanical properties, including fracture

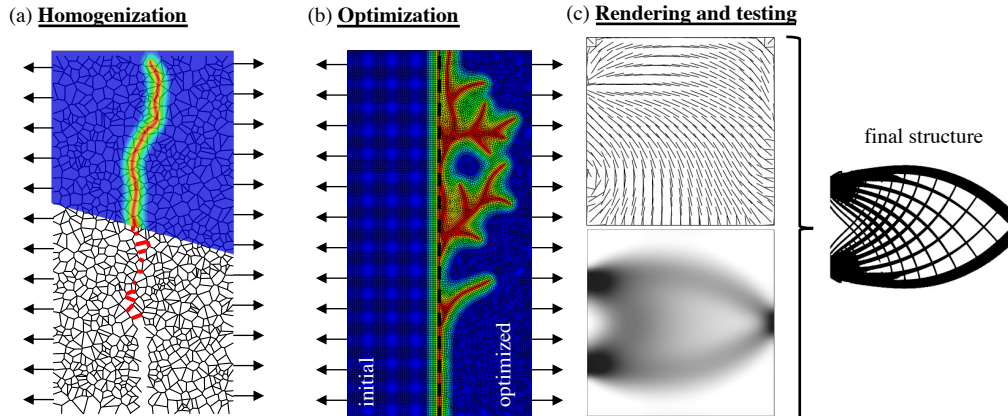


Figure 5.1: Schematic illustration of fracture-resistant material designs.

toughness. Advanced methods, such as Cosserat theory and phase-field fracture modeling, will be employed with the goal of demonstrating that fracture properties can be represented by a single macroscopic model, independent of the material’s geometry or loading conditions.

In parallel, optimization for toughness will concentrate on enhancing fracture resistance through topology optimization. This involves identifying material structures that facilitate energy dissipation and delay crack propagation by promoting micro-branching, thereby increasing overall toughness. Future research will also explore advanced statistical methods and algorithms, such as genetic algorithms [Wang & Tai 2005, Li *et al.* 2022], to discover material configurations that maximize resistance across various loading scenarios.

Finally, de-homogenization [Geoffroy-Donders 2018], or rendering, will involve translating these optimized continuum models back into heterogeneous microstructures suitable for real-world applications. This step is critical for manufacturing, where attention will be given to preserving the structural integrity and smoothness of the microstructures to ensure they accurately reflect the optimized designs. Techniques like convolutional neural networks [Elingaard *et al.* 2022] will be explored to achieve precise projections of the microstructures at the desired scale. These three interconnected aspects will be central to advancing the practical application of fracture-resistant metamaterials.

A notable example of the need for optimizing material architectures can be found in silicon-based anodes for lithium-ion batteries. Silicon, while offering high energy density, becomes increasingly fragile due to repeated stressing at the atomic scale during charge and discharge cycles. This leads to a progressive mechanical breakdown that compromises battery performance [Abdelouhab *et al.* 2024]. As a result, understanding atomic-scale processes becomes crucial for addressing mechanical failure in these systems [Saidi *et al.* 2023]. The design and optimization of the anode structure must account for how silicon deforms and fractures at this scale, requiring a deeper focus on atomic interactions and stress distributions. With advances in additive manufacturing, new structural scales can be reached, enabling precise control over material architecture at both the macro and atomic scales.

Fracture resistant glass compositions — In this study, we have tested various aspects of atomic-scale failure in silicate glasses, gaining valuable insights into how these materials behave under various mechanical conditions. However, the next crucial step is to

unify these findings into a comprehensive constitutive model that can accurately describe the failure mechanisms observed experimentally. Developing such a model will enable us to better understand the intrinsic properties of silicate glasses and their response to different macroscopic loading conditions. This, in turn, could pave the way for the creation of new glass compositions, such as boro-silicate glasses, which are known to exhibit greater resistance to fracture, particularly under compressive loads. These improved glass materials have multiple applications, including use in chemical processing equipment, laboratory glassware, and even in advanced optical devices and nuclear waste containment.

Appendices

A.1 Coupled criterion

A.1.1 Working example

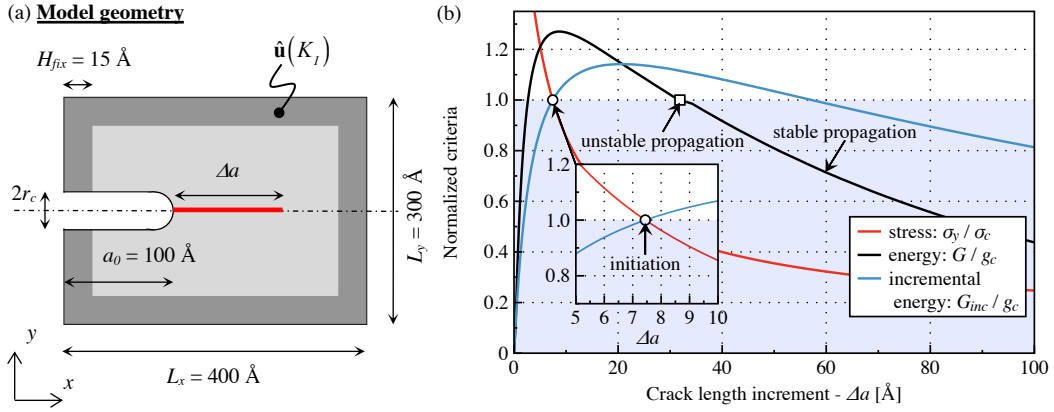


Figure A.1: (a) Geometry of a sample with a rounded notch. (b) Coupled stress and energy criteria for the sample.

The section focuses on the demonstration, how the coupled criterion can predict crack initiation, propagation and arrest. The geometry depicted in Fig. A.1a is particular due to the crack initiating in an unstable way, but after a well-defined distance, it stops. The sides at H_{fix} distance are constrained according to a K-field displacement:

$$\begin{aligned} \hat{u}_x &= \frac{K_I}{8\mu\pi} \sqrt{2\pi r} \left[(2\kappa - 1) \cos \frac{\theta}{2} - \cos \frac{3\theta}{2} \right], \\ \hat{u}_y &= \frac{K_I}{8\mu\pi} \sqrt{2\pi r} \left[(2\kappa + 1) \sin \frac{\theta}{2} - \sin \frac{3\theta}{2} \right], \end{aligned} \quad (\text{A.1})$$

where r and θ are polar coordinates measured from the initial crack tip, μ is the shear modulus, $\kappa = 3 - 4\nu$, and ν is Poisson's ratio. For the bulk sample, the elastic constants were determined as $\mu = 31.7 \text{ GPa}$ and $\nu = 0.25$ for amorphous silica.

As can be seen, the initial crack radius can be varied, and in the case of this particular geometry, neither the tensile stress nor the energy release rates are available analytically. For this reason, the finite element method was used to determine the functions. For the coupled criterion the stress function was calculated using a mesh densified around the crack tip. The smallest element size was chosen to be 0.1 \AA . The energy release rate was calculated by a seam crack, and the opposite nodes were gradually separated. Finally, the derivative of the global potential energy was taken in respect to the crack length, using the finite difference method as shown in eq. (2.1) and (2.2). Essential to note, that to obtain smooth

results, the energy difference had to be calculated on the same mesh. The sample was considered homogeneous and isotropic.

The normalized criteria are presented in Fig. A.1b. The inset illustrates the smallest length where both stress and energy criteria are satisfied (hollow circle), while the global figure shows the evolution of the energy release rate as a function of the crack length.

The crack propagated as long as the differential energy criterion is fulfilled. The energy release rate was not monotonous. In all cases, the energy release rate at $\Delta a = 0$ was zero, since the Griffith criterion cannot be used if there is no sharp crack at the beginning. After this, G first increased according to a power law, then after a maximum value, both functions decreased monotonously. For $\Delta a = L_x - a_0$, G became zero as there was no longer any stored energy in the sample. After the first unstable jump, the energy release rate decreased monotonously wherefore the propagation became stable.

As a consequence the first instance when both incremental energy release rate and strength criteria intersects the same point the line at 1 (circle) pinpoints the loading state when crack initiates. Furthermore, until the moment, the differential energy release rate remains larger then 1 (square) shows the unstable propagation.

A.1.2 Error estimation

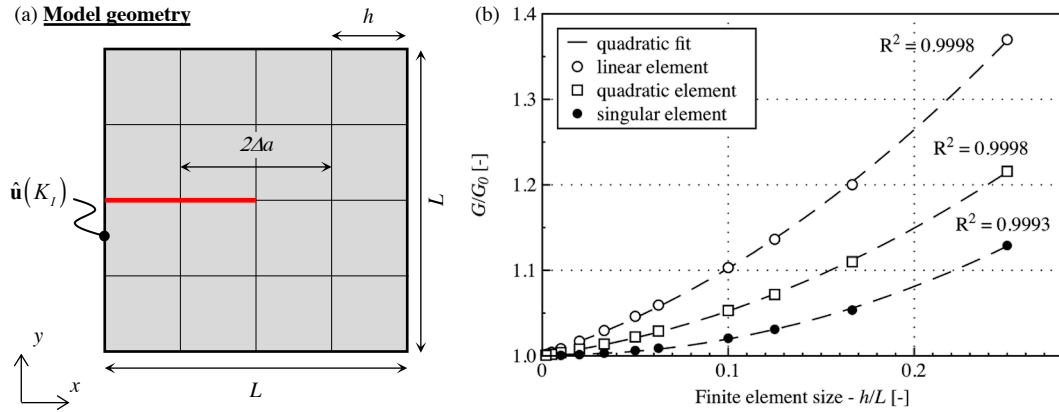


Figure A.2: (a) Geometry of the benchmark sample for mode I opening in infinite space. (b) Energy release rate results as a function of mesh size (h) and element type.

In most geometries the stress field converges quickly with the densification of the finite element mesh. However, due to the moving singularity when calculating the energy release rates, a convergence analysis is necessary. Therefore, this section is dedicated to a benchmark example to show how different mesh densities and finite element types affect the calculation of G .

Basically, A rectangular 2D plane strain geometry was taken with side lengths L . The crack was positioned in the middle with a length of $a_0 = L/2$. For this case, the analytical value is available:

$$G_0 = \frac{K_I (1 - \nu^2)}{E}, \quad (\text{A.2})$$

where K_I represents the applied loading, E is Young's modulus, and ν stands for Poisson's ratio. For this simulation $\nu = 0.3$ was considered.

To calculate the energy release rate exactly at the initial state the crack's length was changed in both forward (right) and backwards (left) direction. Thus the numerically obtained G was calculated from the energy equilibrium:

$$G = -\frac{\Psi(a_0 + \Delta a) - \Psi(a_0 - \Delta a)}{2\Delta a}, \quad (\text{A.3})$$

with Ψ being the potential energies for a fixed loading and varying crack lengths.

To test the effect of mesh density on G we have varied the element size (h) homogeneously keeping $\Delta a = h$.

The results for various element sizes and element types are shown in Fig. A.2b. The presented results clearly indicate that as the element size approaches zero, the computed energy release rate converges to the exact analytical solution. This behavior is consistent across all cases, demonstrating that with sufficiently small element sizes, the finite element method can accurately reproduce the theoretical results.

The convergence behavior for all the element types can be approximated using a second-order polynomial. This finding suggests that the rate of convergence of the energy release rate is quadratic with respect to the element size, which is typical for many finite element approximations. Such a convergence pattern reinforces the reliability of the employed method in recovering the analytical solution as the mesh is refined.

It is also evident that using higher-order elements, such as second-order elements, and the modified singular element [Akin 1994] at the crack tip significantly accelerates the convergence. This is particularly important in the context of fracture mechanics, where accurately capturing stress intensity factors and the associated energy release rates is crucial. The ability of these elements to enhance accuracy with fewer degrees of freedom compared to standard linear elements underscores their potential for efficient numerical simulations.

One notable implication of these findings is that larger elements can be employed in practical simulations while still achieving an accurate approximation of the analytical solution. By extrapolating from results obtained with larger mesh sizes, it may be possible to reduce the computational cost associated with fine mesh discretizations, which is particularly useful in complex or large-scale models where the mesh size becomes a critical factor.

Additionally, the use of singular elements at critical regions, such as crack tips, shows promise for future applications. These elements provide a more efficient means of capturing the localized stress fields and energy release rates without the need for overly refined meshes. This can greatly benefit simulations in industries where fracture mechanics plays a pivotal role, such as aerospace, civil engineering, and materials science. By leveraging singular elements, computational efficiency can be improved without sacrificing accuracy, making this approach advantageous for large-scale simulations in future research and applications.

A.2 Atomic scale simulation

To generate the initial samples, the atoms were placed randomly, taking care that the minimum distance is larger than 1.5 Å. Using NPT ensemble simulations with Berendsen barostat [Berendsen *et al.* 1984] and Nosé-Hoover thermostat [Frenkel & Smit 2002], the systems were first equilibrated at the liquid state of 3000 K and zero pressure (± 5 MPa) for 1.4 picoseconds with a coupling time of one timestep (1 fs) to the thermostat. This way the initial explosion of the kinetic energy was controlled without particle collisions. After this short period the coupling time to the thermostat was set to 2 ps. The systems were then melted for 100 ps at 3000 K. We did not increase further the initial melting temperature because at higher temperature ranges the repulsive part of the potential function becomes active which dilutes the results [Vollmayr *et al.* 1996]. Then the liquids were quenched with the cooling rate of 10 K/ps (10^{+13} K/s) down to a final total kinetic energy ($E_{kin} \sim 10^{-4}$ eV) which corresponded to 10^{-5} K temperature. Finally the systems were equilibrated for 100 ps and the total energy of the systems was minimized using Polak-Ribiere conjugate gradient algorithm to reach static equilibrium. This quenching rate may seem fast, although it was shown in Ref. [Vollmayr *et al.* 1996] and also double checked by this study that neither structural nor density properties change furthermore by decreasing this parameter [Binder & W. Kob 2005].

A.2.1 Potential function

From several types of empirical potential functions developed to describe sodium silicate glasses [Tsuneyuki *et al.* 1989, van Beest *et al.* 1990, Pedone *et al.* 2006, Pedone *et al.* 2007], we chose to adapt the so-called van Beest, Kramer and van Santen (BKS) potential [van Beest *et al.* 1990] which was extensively studied. We used the parameters set according to the work of Yuan and Cormack [Yuan & Cormack 2001]. The two-body potential function used in this paper can be described as follows:

$$\Phi_{\alpha\beta}^{\text{BKS}}(r) = \begin{cases} \Phi_{\alpha\beta}^{\text{Coul}}(r) + \Phi_{\alpha\beta}^{\text{Buck}}(r) \Psi_{\text{cut}}(r, r_{\text{cut}}, \gamma_{\text{cut}}) & \text{for } r \geq r_{\text{rep}}, \\ \Phi_{\alpha\beta}^{\text{Coul}}(r) + \Phi_{\alpha\beta}^{\text{Rep}}(r) & \text{for } r < r_{\text{rep}}, \end{cases} \quad (\text{A.4})$$

where

$$\Phi_{\alpha\beta}^{\text{Buck}}(r) = A_{\alpha\beta} e^{-r/\rho_{\alpha\beta}} - C_{\alpha\beta}/r^6, \quad (\text{A.5})$$

$$\Psi_{\text{cut}}(r, r_{\text{cut}}, \gamma_{\text{cut}}) = e^{-\gamma_{\text{cut}}^2/(r_{\text{cut}}-r)^2}, \quad (\text{A.6})$$

$$\Phi_{\alpha\beta}^{\text{Rep}}(r) = D_{\alpha\beta}/r^{12} + rE_{\alpha\beta} + F_{\alpha\beta}. \quad (\text{A.7})$$

In equation (A.4), α and β correspond to the different species (Si, O or Na) and r is the distance between two atoms. $\Phi_{\alpha\beta}^{\text{Buck}}$ is the well known Buckingham term, which was set according to the parameters ($A_{\alpha\beta}$, $\rho_{\alpha\beta}$, $C_{\alpha\beta}$) of Yuan and Cormack [Yuan & Cormack 2001].

In addition to this description, the $\Psi_{\text{cut}}(r, r_{\text{cut}}, \gamma_{\text{cut}} = 0.5)$ cutoff function was added to the Buckingham potential to ensure that the potential energy and its first derivative (contact force) goes smoothly to zero at the distance equal to the cutoff (r_{cut}). A stronger very short range (if $r < r_{\text{rep}}$) repulsive potential (see in equation A.7) was added to the traditional BKS potential in order to avoid the collapse of atoms at high pressure or temperature as usually seen [Kerrache *et al.* 2006, Mantisi *et al.* 2012]. $D_{\alpha\beta}$, $E_{\alpha\beta}$, and $F_{\alpha\beta}$ have been set, that the potential function and its first and second derivative stays continues. r_{rep} was

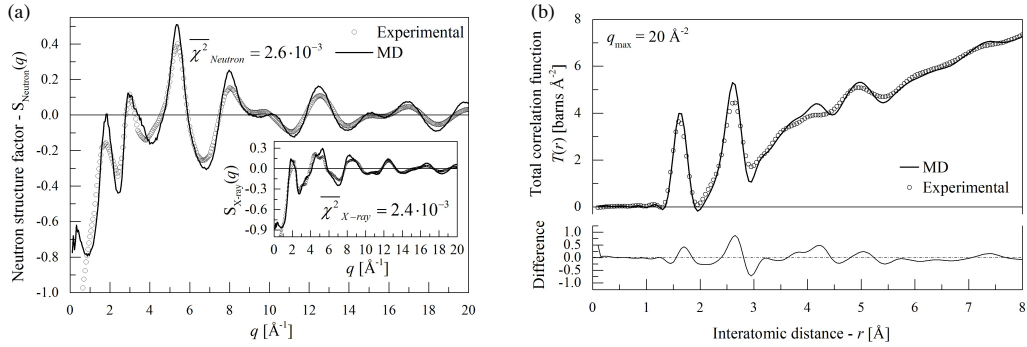


Figure A.3: (a) Comparison between neutron and X-ray structure factor obtained by experiments [Fábíán *et al.* 2007] (circles) and MD simulation (black line) for $x = 30$ %mol Na_2O . (b) Top: Total correlation functions calculated from neutron scattering [Fábíán *et al.* 2007] and MD simulation. Bottom: Difference between MD simulations and experimental measurements from for $x = 30$ %mol Na_2O .

Q^n	This work	Emerson	Maekawa	Charpentier	
Q^0	0.04 %	0 %	0 %	0 %	0 %
Q^1	0.82 %	0 %	0 %	0 %	0 %
Q^2	8.42 %	6 %	2 %	8.33 %	4.17 %
Q^3	38.81 %	40 %	48 %	33.33 %	41.76 %
Q^4	51.91 %	54 %	50 %	58.34 %	54.17 %

Table A.1: Q^n species in sodium silicate containing $x = 20$ %mol Na_2O with the theoretical bond length $r_{\text{Si-O}} = 1.7$ Å. Experimental data were taken from Emerson [Emerson *et al.* 1989], Maekawa [Maekawa *et al.* 1991] and Charpentier [Charpentier *et al.* 2004] (with two different methods).

taken as close as possible to r_0 (distance, where the potential function has its maximum) in order to have a repulsive effect at small r values. The classic Coulomb interactions in equation (A.5) ($\Phi_{\alpha\beta}^{\text{Coul}} = k_C \frac{q_\alpha q_\beta}{r}$, where k_C is Coulomb's constant) are calculated using partial charges ($q_0 = -1.2$, $q_{\text{Si}} = +2.4$ and $q_{\text{Na}} = +0.6$) [Yuan & Cormack 2001].

A.2.2 Structural verification

In Fig. A.3a experimental [Fábíán *et al.* 2007] neutron and X-ray (inset) structure factors are compared with the simulated ones for 30 % Na_2O - 70 % SiO_2 sodium silicate glass. Numerical comparison can be made using a χ^2 test: $\overline{\chi^2} = \sum_{i=1}^{n_p} \left(S(q_i)_{\text{MD}} - S(q_i)_{\text{Experimental}} \right)^2 / n_p$, where $S(q_i)$ is the value of the function at q_i and n_p is the number of q_i points. The difference between the two functions are $\overline{\chi^2}_{\text{Neutron}} = 2.6 \cdot 10^{-3}$ and $\overline{\chi^2}_{\text{X-ray}} = 2.4 \cdot 10^{-3}$, which can be considered relatively low. Furthermore the peaks of the functions are in corresponding places.

A better interpretation of the scattering results can be made with the total correlation functions (TCF) calculated from the Fourier transform of the structure factors. The calculated TCF shown in Fig. A.3b displays a very good match with the experimental data of Fábíán *et al.* [Fábíán *et al.* 2007].

To compare two structures, another standard measurement is the connectivity of the

silica system (Q^n distribution). Therefore, we focused on the number of bridging (BO) and non-bridging oxygen (NBO) atoms around a silicon to describe the connectivity of the silica system. This number was calculated by counting BO atoms, whose position to the central silicon atom was closer than 1.7 Å. This distance is the first local minimum (1.7 Å) after the first peak (1.6 Å) of the corresponding Si-O pair distribution function. We considered bridging oxygens if they had two silicon atoms at a distance closer than 1.7 Å. All other oxygens were considered NBOs. The Q^n species ($n = 4, 3, 2, 1, 0$) are defined as Si atoms having n BO atoms. Table A.1 shows comparison between the Q^n distribution obtained by our simulation and NMR measurements [Emerson *et al.* 1989, Maekawa *et al.* 1991, Charpentier *et al.* 2004]. 20 % Na_2O content was chosen because this is the composition for which the most experimental measurements exists in literature. Our results lie within the scatter of the experimental results.

We have shown in this part, that the comparison between the simulation and experimental data is adequate, and is within the accuracy of the most recent experimental measurements.

A.2.3 Error estimation

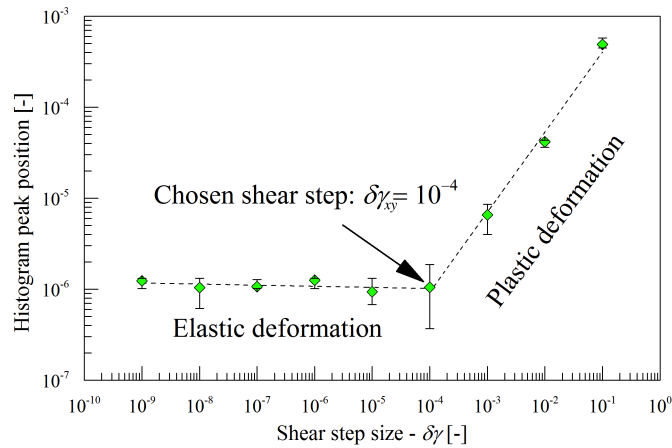


Figure A.4: Position of the peaks of the histograms of the displacement of the particles after a forth and back deformation step as a function of strain step size.

The elementary strain steps were chosen to allow the system to respond elastically. In order to find the largest strain step allowed, the following test was used: the box was deformed, relaxed and re-deformed to its original shape, then the displacement of the atoms were calculated between the original and the new configuration. The remaining displacements were divided by the box length to achieve strain-like unit. The histogram of the remaining displacements were then fitted by a log-normal distribution function. In Fig. A.4 the position of the histogram peak is plotted as a function of the strain step size ($\delta\gamma_{xy}$) for shear deformation. Until $\delta\gamma_{xy} = 10^{-4}$ the average deformation stays elastic, but for larger steps the remaining displacements increase drastically and enter the plastic regime. Therefore the largest elementary strain step used was set to 10^{-4} which is consistent with previous measurements [Mantisi *et al.* 2012, Léonforte *et al.* 2005].

A.3 Coarse-graining

The technique discussed in this chapter is a weighted Gaussian convolution or the so-called coarse-graining method [Goldhirsch & Goldenberg 2002]. Its aim is to transform discrete quantities in space to continuum variables. We can use this method to establish the correlation between discrete simulations like molecular dynamics or discrete elements, and a continuum description (*e.g.*, finite element method). Present method should not be confused with coarse-grained molecular simulations, where stiff atomic configurations (*e.g.*, pyran rings) are replaced by a single larger particle.

The algorithm presented here is a generalized version of the code used in references [Molnár *et al.* 2016d, Molnár *et al.* 2017a, Molnár *et al.* 2018].

The averaging function was chosen as the following form :

$$\phi_{CG}(r) = \frac{1}{w^n \pi^{n/2}} e^{-(r/w)^2}, \quad (\text{A.8})$$

where w is the coarse-graining width and n is the number of dimensions. The function is normalized in order to obtain a unit integral in an infinite domain:

$$\int_{\Omega} \phi_{CG}(r) d\Omega = 1, \quad (\text{A.9})$$

with the distance between grid point and particle:

$$r = \|\mathbf{r}_i - \mathbf{r}\| = \sqrt{(x - x_i)^2 + (y - y_i)^2 + (z - z_i)^2}, \quad (\text{A.10})$$

and x , y and z are the coordinates of the grid point, while x_i , y_i and z_i are the coordinates of particle i .

A.3.1 Local quantities

To obtain the mass belonging to the grid point the following equation is calculated:

$$\rho^{CG}(\mathbf{r}) = \sum_i m_i \phi_{CG}(\|\mathbf{r}_i - \mathbf{r}\|). \quad (\text{A.11})$$

Each particle is taken into account with its proper mass and a weight associated with the particle as a function of its distance to the grid point. This technique can also be used for stress, energy or other discrete quantities defined on particles.

To calculate the displacements on grid points, the particle displacement is normalized by its mass/volume. The weighted average is obtained by the following equation:

$$\mathbf{u}^{CG}(\mathbf{r}) = \frac{\sum_i \mathbf{u}_i m_i \phi_{CG}(\|\mathbf{r}_i - \mathbf{r}\|)}{\sum_i m_i \phi_{CG}(\|\mathbf{r}_i - \mathbf{r}\|)}, \quad (\text{A.12})$$

where \mathbf{u}_i is the displacement vector of atom i .

The spatial derivatives of the displacements (strains) can be calculated analytically. The calculation on the x directional deformation is used to demonstrate the technique:

$$\begin{aligned}
\varepsilon_x^{CG}(\mathbf{r}) &= \frac{\partial u_x^{CG}}{\partial x} = \frac{\partial}{\partial x} \frac{\sum_i u_{x,i} m_i \phi_{CG}(\|\mathbf{r}_i - \mathbf{r}\|)}{\sum_i m_i \phi_{CG}(\|\mathbf{r}_i - \mathbf{r}\|)} = \frac{\partial}{\partial x} \frac{\sum_i u_{x,i} m_i \phi_{CG}(\|\mathbf{r}_i - \mathbf{r}\|)}{\rho(\mathbf{r})} \\
&= \frac{\rho(\mathbf{r}) \frac{\partial}{\partial x} \left[\sum_i u_{x,i} m_i \phi_{CG}(\|\mathbf{r}_i - \mathbf{r}\|) \right] - \left[\sum_i u_{x,i} m_i \phi_{CG}(\|\mathbf{r}_i - \mathbf{r}\|) \right] \cdot \frac{\partial \rho(\mathbf{r})}{\partial x}}{\rho(\mathbf{r})^2} \\
&= \frac{\sum_i u_{x,i} m_i \frac{\partial \phi_{CG}(\|\mathbf{r}_i - \mathbf{r}\|)}{\partial x}}{\rho(\mathbf{r})} - \frac{\left[\sum_i u_{x,i} m_i \phi_{CG}(\|\mathbf{r}_i - \mathbf{r}\|) \right] \cdot \frac{\partial \rho(\mathbf{r})}{\partial x}}{\rho(\mathbf{r}) \cdot \rho(\mathbf{r})} \\
&= \frac{\sum_i u_{x,i} m_i \frac{\partial \phi_{CG}(\|\mathbf{r}_i - \mathbf{r}\|)}{\partial x}}{\rho(\mathbf{r})} - u_x^{CG}(\mathbf{r}) \cdot \frac{\sum_i m_i \frac{\partial \phi_{CG}(\|\mathbf{r}_i - \mathbf{r}\|)}{\partial x}}{\rho(\mathbf{r})}.
\end{aligned} \tag{A.13}$$

The spatial derivatives of the coarse graining function, can be obtained as:

$$\begin{aligned}
\frac{\partial \phi_{CG}(r)_i}{\partial x} &= \frac{1}{w^3 \pi^{3/2}} \frac{\partial}{\partial x} \left[e^{-(r^2/w^2)} \right] \\
&= \frac{1}{w^3 \pi^{3/2}} e^{-(r^2/w^2)} \cdot \frac{\partial}{\partial x} \left(-\frac{r^2}{w^2} \right) \\
&= \frac{1}{w^3 \pi^{3/2}} e^{-(r^2/w^2)} \cdot \left(-\frac{1}{w^2} \right) \cdot \frac{\partial}{\partial x} (x - x_i)^2 \cdot \\
&= \frac{1}{w^3 \pi^{3/2}} e^{-(r^2/w^2)} \cdot \left(-\frac{1}{w^2} \right) \cdot 2(x - x_i) \\
&= -\frac{2(x - x_i)}{w^5 \pi^{3/2}} e^{-(r^2/w^2)}.
\end{aligned} \tag{A.14}$$

A.3.2 Error estimation

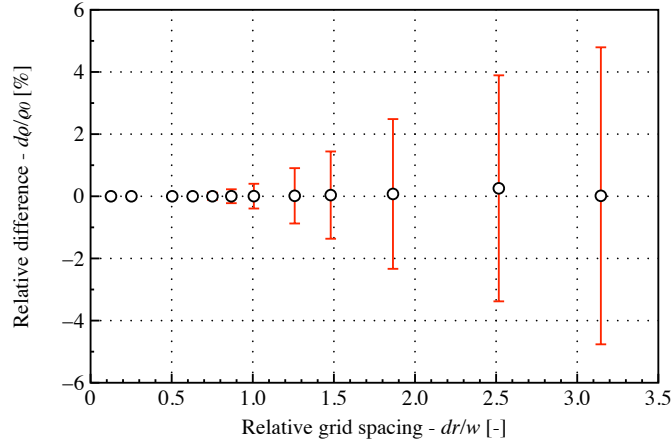


Figure A.5: Mean relative difference in mass density as a function of the grid spacing. The error bar shows the relative standard deviation.

One of the critical decisions to make before executing the coarse-graining algorithm is the characteristic distance between grid points. While the w , the coarse-graining length, should be determined based on the discrete structure, the grid points possess no real physical meaning. Basically, we only chose the positions, where the continuum quantities are sampled.

To demonstrate the influence of the grid distance on the obtained results, we have executed the technique on the middle plane of a large $400 \times 300 \times 100 \text{ \AA}^3$ system. The coarse-graining width was fixed at $w = 8 \text{ \AA}$, with a cutoff of $r_{cut} = 3w$.

First, a relatively small grid distance was chosen, $dx = dy = dz = 1 \text{ \AA}$, to which the results of larger grid spacing were compared by first calculating the local density then using a 2D spline interpolation the grid spacing was densified to 1 \AA . The advantage of the former method is that the interpolation is incredible fast, and if we find the maximum spacing where no more detail could be collected from the microstructure, renders further densification (*e.g.*, calculating the coarse-grained quantities on all atomic positions) pointless and only a waste of time.

Fig. A.5 displays the average relative difference and its standard deviation as a function of relative grid spacing. In the figure, it can be seen, that the mean difference between a fine and a coarse grid is relatively small, which means, that until the analysis has a representative portion of the sample, the mean value will represent the global quantity relatively well. However, when considering the local variations, thus the standard deviation of the mass density difference, we see that if the grid spacing is larger than w a difference is detected between interpolated and calculated results. As a consequence, we always recommend to take a grid distance slightly lower than the coarse-graining with and densify the tessellation using interpolation techniques if it is needed for visualization purposes. However, taking a too dense grid, is pointless.

Parallel projects

This chapter presents several projects I worked on in parallel to the main subject of the manuscript. While these projects have not yet made a direct contribution to understanding length scales in fracture, they offer valuable insights and may spark new directions for future research.

Associated publications

- [G. Molnár](#), D. Rodney, P. Dumont, F. Martoia, Y. Nishiyama, K. Mazeau, L. Orgéas, *Cellulose crystals plastify by localized shear*, Proceedings of the National Academy of Sciences of USA, 115 (28) 7260-7265, 2018.
- A. Saidi, A. Tanguy, M. Fourmeau, [G. Molnár](#), A. Boucherif, D. Machon, *Coupling between mechanical stresses and lithium penetration in a lithium ion battery*, Mechanics of Materials, 177, 104532, 2023.
- M. Sepulveda-Maciasa, [G. Molnár](#), A. Tanguy, *Thermomechanical Dissipative behaviour of Metallic Glasses*, Journal of Non-Crystalline Solids, 636, 123028, 2024.

Contents

B.1	Elasto-plastic response of cellulose nanofibrils	90
B.2	Lithium penetration in a silicon-based batteries	91
B.3	Heat conductivity of bulk metallic glasses	91

B.1 Elasto-plastic response of cellulose nanofibrils

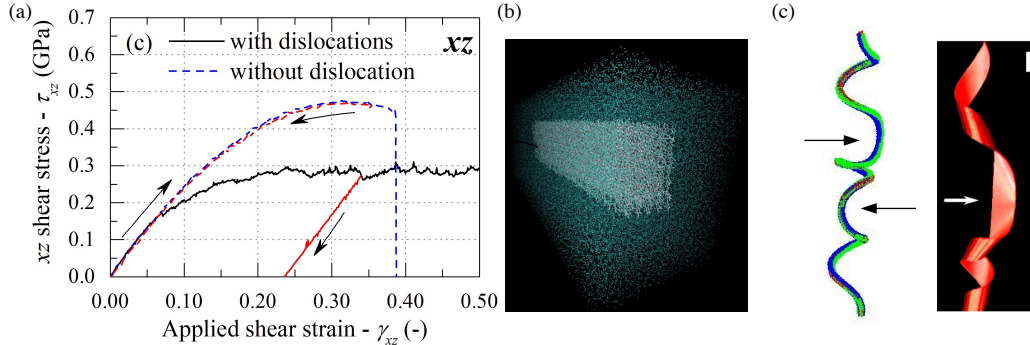


Figure B.1: (a) Molecular dynamic simulation of a periodic cellulose crystal with and without dislocations. (b) Finite size atomistic cellulose nanofibril in water. (c) Discrete element simulation showing a helical perversion (shown by arrows) compared to an experimental demonstration [Silva *et al.* 2016].

The project focused on the multi-scale analysis of the elasto-plastic response of cellulose nanofibrils. The project’s strategy is summarized in Fig. B.1

First, we explored the plastic deformation of cellulose crystals under shear using atomistic simulations in a periodic environment to uncover the mechanisms governing their mechanical behavior. Cellulose microfibrils, which are essential structural elements in plants and potential eco-friendly reinforcements in engineered materials, possess complex mechanical properties that are not fully understood, especially their behavior under shear deformation.

We focused on cellulose I β , the most common crystalline form in plants, and performed molecular statics simulations to analyze its response to shear along three different planes. Our results showed that cellulose crystals exhibit a highly anisotropic elastoplastic behavior characterized by localized shear bands, which form depending on the direction of the applied shear. For perfect crystals, we observed that the shear deformation is accompanied by significant dilatancy, with the cellulose chains undergoing local deformations, translations, and rotations.

Additionally, we demonstrated that defects, such as dislocations, significantly impact the mechanical properties of cellulose crystals, reducing both yield strength and dilatancy in a manner akin to metallic crystals. These findings underscore the importance of both perfect and defective structures in the plastic deformation of cellulose, providing a basis for micromechanical modeling of cellulose microfibrils in structural applications. Our research thus advances the understanding of cellulose crystal mechanics, particularly their plasticity under shear, and lays the groundwork for developing novel materials with enhanced mechanical properties.

Subsequently, we investigated the behavior of finite-sized cellulose beams (fibrils) under torsion, bending, and buckling using molecular dynamics simulations. In the final phase, we conducted a beam-like discrete element [Bergou *et al.* 2008] analysis of lightly packed nanofibrillated cellulose suspensions. The discrete element model employed was specifically designed to simulate thin, flexible rods, efficiently capturing their extension, bending, and twisting dynamics by explicitly modeling the centerline for tension and bending, while treating the material frame for twisting quasistatically.

B.2 Lithium penetration in a silicon-based batteries

In this study we explored the coupling between mechanical stresses and lithium penetration in silicon-based anodes for lithium-ion batteries using molecular dynamics simulations. Silicon anodes are a promising alternative to traditional graphite due to their high theoretical capacity, but they face significant challenges from mechanical stresses during lithiation, leading to rapid degradation.

We focused on understanding how mechanical and electrochemical phenomena interact during lithiation. We first examined the diffusion of lithium atoms in silicon, revealing that this process is highly dependent on the crystalline orientation and applied pressure. Notably, we observed a regime change in lithium diffusion above a certain pressure threshold, where lithium atoms displayed a ballistic motion along specific crystallographic planes.

To compute the local stress fields generated by lithiation, we used a coarse-graining method that considers thermal effects. We found that the stress field varies significantly based on lithium density, temperature, and the crystalline orientation of the free surface. High pressures induced by lithiation can lead to the amorphization of the silicon support, a critical factor affecting the stability and durability of the anode.

Our findings highlight the crucial role of mechanical constraints in influencing lithium diffusion and the associated stress fields, providing new insights into optimizing silicon-based anodes for longer-lasting, more efficient lithium-ion batteries.

B.3 Heat conductivity of bulk metallic glasses

In our study, we investigated the thermo-mechanical behavior of $Zr_{50}Cu_{50}$ metallic glass by employing molecular dynamics simulations to explore how plastic deformation affects heat generation and dissipation under different conditions. Specifically, we examined the influence of strain rate, temperature, and sample size on the material's behavior.

We began by performing simulations on two different samples of $Zr_{50}Cu_{50}$ metallic glass: a small sample containing 4800 atoms and a larger sample containing 145200 atoms. Both samples were subjected to successive cycles of volume-preserving shear deformation across various strain rates (10^8 , 10^9 , and 10^{10} 1/s) and temperatures (10 K, 100 K, and 300 K). During these simulations, we measured the stress-strain response and monitored the evolution of temperature to derive thermo-mechanical constitutive laws. The schematic illustration of the methodology is depicted in Fig. B.2.

Our findings revealed that plastic deformation in metallic glasses serves as a significant heat source. However, we observed strong finite size effects that impact the formation and dissipation rate of shear bands, which are localized zones of intense deformation where most of the heat generation occurs. The small sample displayed markedly different thermomechanical behaviors compared to the larger sample, particularly at lower strain rates. This discrepancy arises because the smaller sample is unable to form large, mature shear bands effectively, thereby failing to replicate the collective deformation behavior seen in larger systems.

We also found that the material's response is highly sensitive to the strain rate. At higher strain rates, the mechanical behavior of the glass becomes smoother, and we observed the formation of thermal hysteresis loops, which indicate a persistent temperature change during each loading-unloading cycle. In contrast, at lower strain rates, the material exhibits a more chaotic, noisy behavior, characterized by pronounced local plastic events and less thermal stabilization.

To quantitatively describe this complex behavior, we proposed a thermo-mechanical

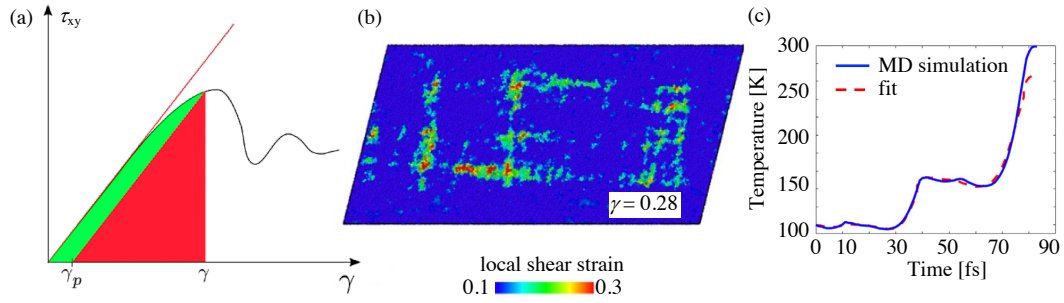


Figure B.2: (a) Comparison between the elastic strain energy and the dissipated plastic energy densities. The shear modulus values are given by the initial slope in the stress–strain curve. (b) Shear bands for the large sample at an initial temperature of 100 K and a loading rate of 10^{10} 1/s. Shear strain is computed from the deviatoric part of the coarse-grained strain tensor. (c) Comparison between simulated temperature and fit using the thermo-mechanical constitutive law from plastic dissipation.

constitutive law at the continuum scale. This law accounts for the conversion of plastic work into heat (the thermo-mechanical coupling effect) and allows us to predict the temperature evolution of the material based on strain rate, temperature, and finite size effects. Our model effectively reproduces the observed self-heating phenomena, demonstrating the strong interplay between thermal and mechanical responses in metallic glasses.

Our study offers new insights into the fundamental thermo-mechanical properties of $Zr_{50}Cu_{50}$ metallic glass, highlighting how plastic deformation leads to significant self-heating, with this behavior being strongly influenced by strain rate, temperature, and sample size. These findings underscore the importance of considering these factors when designing applications that utilize metallic glasses, particularly in fields like nanotechnology, micro-electro-mechanical systems, and biomedical devices, where precise thermal management is crucial.

In conclusion, our work provides a deeper understanding of the complex interplay between mechanical deformation and thermal response in metallic glasses, paving the way for more accurate modeling and potential optimization of their use in various advanced technologies.

Curriculum vitae

Personal information

Name: Molnár, Gergely
Identifiers: [ORCID 0000-0002-7274-5373](https://orcid.org/0000-0002-7274-5373)
[Research ID N-9034-2016](https://orcid.org/0000-0002-7274-5373)
Date of birth: 27/08/1986
Nationality: Hungarian
Website: molnar-research.com
Google Scholar : scholar.google.fr/citations?user=KWldOG8AAAAAJ&hl

Research thematic

- Modeling and experimental study of crack propagation in static and dynamic cases.
- Multi-scale understanding of the resistance of amorphous materials.
- Development of optimization processes to design fracture resistant architected materials.

Education & Employment

2018- **CNRS Researcher (CR)**, section 9, INSA de Lyon, LaMCoS, Lyon
2017-2018 **Postdoc**, École Centrale de Nantes, GeM, Nantes
2016-2017 **Postdoc**, Univ. Grenoble Alpes, 3SR, Grenoble
2016 (5 mois) **Postdoc**, INSA de Lyon, LaMCoS, Lyon
2015-2016 **Postdoc**, École des Mines de Saint-Étienne, Saint Étienne
2014-2015 **Postdoc**, Univ. Lyon 1, ILM , Lyon
2011-2014 **Ph.D.**, Budapest Univ. of Technology and Economics, Budapest, Hungary
Thesis title: "Multi-scale modelling of structural glass"
2009-2011 **M.Sc.**, Budapest Univ. of Technology and Economics, Budapest, Hungary
2005-2009 **B.Sc.**, Budapest Univ. of Technology and Economics, Budapest, Hungary

Awards

- Best foreign Postdoctoral researcher in Lyon (by AAUL), 2016
(Multiscale mechanical modelling of sodium silicate glasses)

- Conference grant for Early Stage Researchers (by COST), 2014
(Rate dependent elastic response of modelled soda-lime-silica)
- Itasca Education Partnership Mentorship Program (by Itasca Inc.), 2013
(Post-brakeage behavior of laminated glass panels)
- 1th prize of the Mat. Conf. of Scientific Students' Associations (OTDK), 2011
(Numerical stability and critical time step evaluation of explicit solvers)
- Diploma Award Competition of the Hungarian Engineering Chamber, 2009
(Glass roof reconstruction for the central building of BUTE)

Research projects

- **2019-2025:** ANR PRCE, project e-WARNINGS: *"Early detection of fatigue and intermittent failure using full-field approved Acoustic Emission multiplets"*
Main participants: S. Deschanel (MATEIS), J. Réthoré (GeM), J. Weiss (ISTerre), G. Molnár (LaMCoS), A. Proust (Mistras Group)
Role: PI for LaMCoS (PI: S. Deschanel)
Funding: 630k€(LaMCoS: 103k€)
- **2021-2026:** ANR PRC, project GaLAaD: *"Crack initiation in silicate glasses – plastic flow, shear bands and damage"*
Main participants: E. Barthel (SIMM/ESPCI), M. Ciccotti (SIMM/ESPCI), G. Molnár (LaMCoS)
Role: PI for LaMCoS (PI: E. Barthel)
Funding: 414k€(LaMCoS: 150k€)
- **2021-2026:** ANR PRC, project RATES: *"high strain RAte, TEMperature and Small-scale mechanical properties of materials"*
Main participants: G. Kermouche (LGF/MINES), M. Fivel (SIMaP), A. Tanguy (LaMCoS), J.-L. Loubet (LTDS)
Role: Investigator (PI: G. Kermouche)
Funding: 486k€(LaMCoS: 114k€)
- **2019-2023:** Regional project CarAbdo: *"Mechanical characterization of abdominal walls repaired by the application of a reinforcing textile, with a view to limiting the risks of eventration"* (in French)
Main participants: B. Pierrat (STBio/MINES), A. Bel-Brunon (LaMCoS)
Role: Investigator (PI: B. Pierrat)
Funding: 99k€

Industrial projects

- **2018-2022:** IRSN Cadarache: *"Study of the creep behavior of pre-oxidized zirconium alloy sheaths under thermomechanical stresses representative of a primary coolant loss accident"* (in French)
Collaborators: J. Desquines (IRSN), T. Taurines (IRSN), M.-C. Baietto (LaMCoS), N. Tardif (LaMCoS), M. Coret (GeM)
Role: co-PI
Funding: 68k€+ PhD student

- **2020-2023:** CEA Saclay: "*Crack propagation by a coupled AMR/phase field approach*"
Collaborators: B. Prabel (CEA), J. Bluthé (CEA), A. Gravouil (LaMCoS)
Role: co-PI
Funding: 30k€+ PhD student
- **2018-:** Nippon Electric Glass: "*On the study of plastic behavior of silicate glasses at the atomic scale*"
Collaborators: G. Rosales (NEG), Y. Kato (NEG), E. Barthel (SIMM/ESPCI)
Role: PI
Funding: 40k€

Memberships

- I am an active member and participant in the gatherings of the GDRs **MePhy**, **ARCHI-META**, and **IDE**, which cover a wide range of topics, from the physics and mechanics of complex systems to architected materials and the application of artificial intelligence to disordered materials.
- I am also a member of **EUROMECH**, **ISMM**, **Mécamat**, and **CSMA**.

Supervision

Postdoctoral researchers

- 2022-2023: **Eli Eid** (ANR e-WARNINGS) : Numerical identification of the acoustic signal emitted by intermittent crack propagation using the phase-field method.
- 2022-2023: **Sára Lévy** (ANR GaLaAD): Shear band and damage formation in soda-lime and boro-silicate glasses in atomic-scale models.
- 2022-2023: **Matías Sepúlveda** (ANR RATES): Heat conductivity of bulk metallic glasses.
- 2024-2025: **Kevin Daigne** (Project COMUN, AAP LaMCoS): Numerical investigation of multi-scale nature of contact. (in French)
- 2024-2025: **Sylvain Fournier** (CEA Grenoble / LITEN): Mechanical reliability of Solid Oxide Cell during Ni re-oxidation.
- 2025-2026: **Hui Ruan** (ANR GaLaAD): Brittle to ductile transition in silicate glasses using the phase-field model.

Ph.D students

- 2018-2022 (def. 26/04/2022): **Ethel-Borel Djeumen** (IRSN Cadarache) (codirector): Study of the creep behavior of pre-oxidized zirconium alloy sheaths under thermomechanical stresses representative of a primary coolant loss accident. (in French)
- 2019-2023 (def. 10/02/2023): **Baptiste Pillet** (CarAbdo): Mechanical characterization of abdominal walls repaired by the application of a reinforcing mesh.
- 2020-2023 (def. 07/11/2023): **Adrien Jaccon** (CEA Saclay) (codirector): Numerical acceleration methods for high cycle fatigue crack propagation with a phase-field model.
- 2024-2027: **Tom Guisard** (CNRS, Sherbrooke University Canada): Structural optimization of silicon anode batteries using the phase-field technique.

Thesis juries

- **Thomas Duminy** : "Multi-scale characterization and simulation of fracture in nacre-like ceramics " (dir. : Sylvain Meille, INSA Lyon, 2023)
- **Soukaina Riad** : "Towards irradiation-assisted stress corrosion modeling of super-alloy 718" (in French) (dir. : Julien Réthoré, EC Nantes, 2022)
- **Vasudevan Kamasamudram** : "Investigation of dynamic fracture of elastomers: On the role played by viscoelasticity" (dir. : Michel Coret, EC Nantes, 2021)

Teaching activities

In the **CarAbdo** project, I welcomed an intern, Xavier Faure (4th-year student), at **LaM-CoS** in 2022.

Additionally, I contributed to the **PRI (Final Study Project)** courses (M2) at **INSA Lyon** for the Mechanical Engineering Department by supervising the following students:

1. Adrien Jaccon (01/2020, 8 hours)
2. Bastien Rivière (02/2021, 16 hours)
3. Charles Mareau (02/2021, 16 hours)
4. Hamza Radi (01/2022, 16 hours)

These students worked on the homogenization of toughness in micro-structured materials.

I also regularly post tutorials on YouTube about phase-field modeling of fracture. As of November 15th, 2024, the channel had 517 subscribers and 36,626 views.

Organization related activities

- I was participating in the organization of the conference "Plasticité 2023", which is a French national conference aiming to discuss recent developments in plasticity. The conference took place in Lyon from April 3 to 5, 2023. It is a traditional conference with a long history (for the last 50 years) with a biannual frequency and about 100 to 120 participants. Co-organizers: Pierre Antoine Geslin (main organizer), David Rodney, Michel Perez, Tristan Albaret, and Stéphanie Deschanel.
- I am regularly organizing invited sessions at the COMPLAS conference series in Barcelona on multi-scale mechanics of material failure.
- I am co-organizing the damage, plasticity and fracture symposium at ESMC 2025.
- I chaired sessions at the Plasticité 2023 (Lyon), ECF23 (Madeira), ICPDF 2024 (Panama) and COMPLAS 2023 (Barcelona) conferences.

Editorial and reviewer activities

- I am a member of the editorial board of the journal "Glass Structures & Engineering" (Springer, IF 1.5).

-
- I am a regular reviewer for the journals: Journal of the Mechanics and Physics of Solids, Acta Materialia, Computational Mechanics, Theoretical and Applied Fracture Mechanics, Computer Methods in Applied Mechanics and Engineering, International Journal of Fracture, Mechanics of Materials, Engineering Fracture Mechanics, International Journal of Mechanical Sciences and International Journal of Applied Glass Science. Over the 5 years, I have reviewed around 40 articles.

Administrative tasks

- **Since 2024**, I have been an elected member of the **LaMCoS** advisory board. The laboratory comprises 239 members, including 80 permanent and 159 temporary staff. We collaborate with numerous industrial partners, such as Airbus, DGA, EDF, and SAFRAN. The board represents all member groups, from full professors to Ph.D. students; I represent the associate professors. Our role is to provide strategic guidance, evaluate research directions, and foster collaborations to enhance the laboratory's scientific impact and alignment with national and international priorities.
- **Since 2022**, I have been a member of the **LaMCoS IT Commission**, where we review investments and developments, focusing on the laboratory's digital assets.

Conferences and seminars

Invited talks

- NewFrac 2024 (Porto, Portugal, 2024)
- EMMC 2024 (Madrid, Spain, 2024)
- COMPLAS 2023 (Barcelona, Spain, 2023)
- NewFrac 2023 (Torino, Italy, 2023)
- COMPLAS 2021 (Barcelona, Spain, 2021)
- Challenging Glass 5 (Ghent, Belgium, 2015)

Conference attendances

- MMM-11 (Prague, Czech Republic, 2024)
- ICPDF 2024 (Panama city, Panama, 2024)
- Challenging Glass 9 (Delft, Netherlands, 2024)
- CFRAC 2023 (Prague, Czech Republic, 2023)
- EUROMECH Colloquia FFM (Lyon, France, 2023)
- DPG Spring Meeting (Dresden, Germany, 2023)
- EMMC 18 (Oxford, UK, 2022)
- CSMA 2022 (Giens, France, 2022)
- ECF 23 (Madeira, Portugal, 2022)
- ICG 26 (Berlin, Germany, 2022)
- WCCM 14 (Paris, France, 2020)
- COMPLAS 2019 (Barcelone, Spain, 2019)

- DGG 2019 (Nürnberg, Germany, 2019)
- ESMC 2018 (Bologna, Italy, 2018)
- ISDMM 2017 (Lyon, France, 2017)
- ICC 2017 (Fukuoka, Japan, 2017) - poster
- MMM-8 (Dijon, France, 2016)
- MRS 2015 (Boston, USA, 2015)
- CFM 2015 (Lyon, France, 2015)
- Challenging Glass 5 (Lausanne, Switzerland, 2014)
- IIS 2019 (Vienna, Austria, 2013)
- Particles 2013 (Stuttgart, Germany, 2013)
- Structural Glass Conference (Poreč, Croatia, 2013)
- ESMC 2012 (Graz, Austria, 2012)
- DAS 28 (Siófok, Hungary, 2011) - poster
- MAMEK XI. (Miskolc, Hungary, 2011)

Invited seminars

- LaMCoS, INSA Lyon, France, 2022
- 3SR, UGA, Grenoble, France, 2017
- PMMH, ESPCI, Paris, France, 2017
- GeM, EC Nantes, Nantes, France, 2017
- LaMCoS, INSA Lyon, Lyon, France, 2016
- <MSE>2, MIT-CNRS, Cambridge, USA, 2016
- École Polytechnique, Palaiseau, 2015

List of publication

In preparation

G. Molnár, E. Barthel, How glass breaks – Damage explains the difference between surface and fracture energies in amorphous silica, *Physical Review Letters* (submitted, 2024) [arxiv: arxiv.org/abs/2412.11817](https://arxiv.org/abs/2412.11817)

G. Molnár, J. Réthoré, Fracture Toughness of Periodic Beam Lattices, *Journal of Theoretical, Computational and Applied Mechanics* (submitted, 2024) [hal: hal-04793587](https://hal.archives-ouvertes.fr/hal-04793587)

Peer-reviewed journal articles

2025

[[Molnár & Doitrand 2025](#)] A. Doitrand G. Molnár, Understanding regularized crack initiation through the lens of Finite Fracture Mechanics, *International Journal of Fracture*, 249, 12, 2025.

[[Molnár et al. 2025](#)] G. Molnár, A. Doitrand, R. Estevez and A. Gravouil, A Review of Characteristic Lengths in the Coupled Criterion Framework and Advanced Fracture Models, *Comptes Rendus. Mécanique*, 353, pp. 91-111, 2025.

2024

[[Molnár et al. 2024](#)] G. Molnár, A. Doitrand and V. Lazarus. Phase-field simulation and coupled criterion link echelon cracks to internal length in antiplane shear. *Journal of the Mechanics and Physics of Solids*, 188, p. 105675, 2024.

[[Sepulveda-Macias et al. 2024](#)] M. Sepulveda-Macias, G. Molnár, A. Tanguy, Thermomechanical dissipative behaviour of CuZr metallic glasses, *Journal of Non-Crystalline Solids*, 636, 123028, 2024.

2023

[[Eid et al. 2023](#)] E. Eid, A. Gravouil, G. Molnár, Influence of rate-dependent damage phase-field on the limiting crack-tip velocity in dynamic fracture, *Engineering Fracture Mechanics*, 292, 109620, 2023.

[[Jacon et al. 2023](#)] A. Jacon, B. Prabel, G. Molnár, J. Bluthé, A. Gravouil, Adaptive mesh refinement and cycle jumps for phase-field fatigue fracture modeling, *Finite Elements in Analysis and Design*, 224, 104004, 2023.

[[Doitrand et al. 2023a](#)] A. Doitrand, D. Leguillon, G. Molnár, V. Lazarus, Revisiting facet nucleation under mixed mode I + III loading with T-stress and mode-dependent fracture properties, *International Journal of Fracture*, 242 pp. 85–106, 2023.

[[Molnár & Blal 2023](#)] G. Molnár, N. Blal, Topology optimization of periodic beam lattices using Cosserat elasticity, *Computers & Structures*, 281, 107037, 2023.

[[Doitrand et al. 2023b](#)] A. Doitrand, G. Molnár, R. Estevez, A. Gravouil, Strength-based regularization length in phase field fracture, *Theoretical and Applied Fracture*

Mechanics, 124, 103728, 2023.

[Saidi *et al.* 2023] A. Saidi, A. Tanguy, M. Fourmeau, G. Molnár, A. Boucherif, D. Machon, Coupling between mechanical stresses and lithium penetration in a lithium ion battery, *Mechanics of Materials*, 177, 104532, 2023.

2022

[Barthel *et al.* 2022] E. Barthel, T. Deschamps, G. Kermouche, C. Martinet, G. Molnár, A. Tanguy, Le verre: fragile ou ductile ? *Reflète physique*, 74, 46-51, 2022.

[Deschamps *et al.* 2022] T. Deschamps, C. Martinet, B. Champagnon, G. Molnár, E. Barthel, Memory effect in the plasticity of a silicate glass densified at room temperature, *Physical Review B*, 105, 224206, 2022.

[Djeumen *et al.* 2022] E. Djeumen, G. Molnár, N. Tardif, M. Coret, J. Desquines, T. Taurines, M.-C. Baïetto, Modeling diffusive phase transformation and fracture in viscoplastic materials, *International Journal of Solids and Structures*, 252, 111757, 2022.

[Molnár *et al.* 2022] G. Molnár, A. Doitrand, A. Jaccon, B. Prabel, A. Gravouil, Thermodynamically consistent linear-gradient damage model in Abaqus, *Engineering Fracture Mechanics*, 266, 108390, 2022.

[Doitrand *et al.* 2022] A. Doitrand, G. Molnár, D. Leguillon, E. Martin, N. Carrère, Dynamic crack initiation assessment with the coupled criterion, *European Journal of Mechanics - A/Solids*, 93, 104483, 2022.

2020

[Molnár *et al.* 2020a] G. Molnár, A. Doitrand, R. Estevez, A. Gravouil, Toughness or strength? Regularization in phase-field fracture explained by the coupled criterion, *Theoretical and Applied Fracture Mechanics*, 109, 102736, 2020.

[Molnár *et al.* 2020b] G. Molnár, A. Gravouil, R. Seghir, J. Réthoré, An open-source Abaqus implementation of the phase-field method to study the effect of plasticity on the instantaneous fracture toughness in dynamic crack propagation, *Computer Methods in Applied Mechanics and Engineering*, 365, 113004, 2020.

[Martinet *et al.* 2020] C. Martinet, M. Heili, V. Martinez, G. Kermouche, G. Molnár, N. Shcheblanov, E. Barthel, A. Tanguy, Highlighting the impact of shear strain on the SiO₂ glass structure: From experiments to atomistic simulations, *Journal of Non-Crystalline Solids*, 553, 119898, 2020.

2018

[Molnár *et al.* 2018] G. Molnár, D. Rodney, P. Dumont, F. Martoia, Y. Nishiyama, K. Mazeau, L. Orgéas, Cellulose crystals plastify by localized shear, *Proceedings of the National Academy of Sciences of USA*, 115 (28) 7260-7265, 2018.

2017

[Molnár *et al.* 2017b] G. Molnár, G. Kermouche, E. Barthel, Plastic response of amorphous silicates, from atomistic simulations to experiments – A general constitutive relation, *Mechanics of Materials*, 114 pp. 1-8, 2017.

[Molnár *et al.* 2017a] G. Molnár, P. Ganster, A. Tanguy, Effect of composition and pressure on the shear strength of sodium silicate glasses: An atomic scale simulation study, *Physical Review E*, 95, 043001, 2017.

[Molnár & Gravouil 2017] G. Molnár, A. Gravouil, 2D and 3D Abaqus implementation of a robust staggered phase-field solution for modeling brittle fracture, *Finite Elements in Analysis and Design*, 130 pp. 27-38, 2017.

2016

[Molnár *et al.* 2016b] [G. Molnár](#), P. Ganster, A. Tanguy, E. Barthel, G. Kermouche, Densification dependent yield criteria for sodium silicate glasses – An atomistic simulation approach, *Acta Materialia*, 111 pp. 129-137, 2016.

[Molnár *et al.* 2016c] [G. Molnár](#), P. Ganster, A. Tanguy, J. Török, G. Kermouche, Transition from ductile to brittle failure of sodium silicate glasses: a numerical study, *MRS Advances*, 1(24) pp. 1797-1802, 2016.

[Molnár *et al.* 2016d] [G. Molnár](#), P. Ganster, J. Török, A. Tanguy, Sodium effect on static mechanical behavior of MD-modeled sodium silicate glasses, *Journal of Non-Crystalline Solids*, 440 pp. 12-25, 2016.

[Molnár *et al.* 2016a] [G. Molnár](#), M. Ferentzi, Z. Weltsch, G. Szabó, L. Borbás, I. Bojtár, Fragmentation of wedge loaded tempered structural glass, *Glass Structures & Engineering*, pp 1-10, 2016.

2013

[Molnár & Bojtár 2013] [G. Molnár](#), I. Bojtár, The effects of the manufacturing inhomogeneities on strength properties of float glass, *Mechanics of Materials*, 59 pp. 1-13, 2013.

2012

[Molnár *et al.* 2012d] [G. Molnár](#), L. G. Vigh, Gy. Stocker, L. Dunai, Finite Element Analysis of Laminated Structural Glass Plates With Polyvinyl Butyral (PVB) Interlayer, *Periodica Polytechnica Civil Engineering*, 56(1) pp. 35-42, 2012.

[Molnár *et al.* 2012b] [G. Molnár](#), L. M. Molnár, I. Bojtár, Preparing a comprehensive analysis of the mechanical classification of structural glass, *Materials Engineering*, 19 pp. 71-81, 2012.

[Molnár *et al.* 2012a] [G. Molnár](#), L. M. Molnár, I. Bojtár, Multi-Scale Analysis of Structural Glass, Imaging of The Mesosstructure, *Journal of Material Testers*, 21(3-4) pp. 1-14, 2012. (in Hungarian)

[Molnár & Bojtár 2012] [G. Molnár](#), I. Bojtár, Solution of 1D Finite Element Problems With Explicit Time Integration, *Architectonics and Architecture*, 40(1) pp. 5-32, 2012. (in Hungarian)

[Molnár *et al.* 2012c] [G. Molnár](#), L. G. Vigh, Gy. Stocker, Load bearing capacity of laminated glass, *Magyar Építőipar*, 62(1) pp. 17-23, 2012. (in Hungarian)

Peer-reviewed conference proceedings

[Molnár 2024] [G. Molnár](#), Challenges in Phase-Field Modeling of Glass Fracture, Challenging Glass Conference Proceedings, vol. 9, Delft, 2024. ([hal-04684123v1](#))

[1] [G. Molnár](#), I. Bojtár, J. Török, Microscopic scale Simulations of Soda-Lime-Silica Using Molecular Dynamics, Proceedings of PARTICLES 2013, Stuttgart, 2013.

[2] [G. Molnár](#), I. Bojtár, J. H. Nielsen, Ongoing Model Development Analyzing Glass Fracture, COST Action TU0905, Mid-term Conference on Structural Glass, pp. 197-204, Poreč, 2013.

[3] M. Vandebroek, J. Belis, C. Louter, [G. Molnár](#), Ratio of mirror zone depth to flaw depth after failure of glass beams' COST Action TU0905, Mid-term Conference on Structural Glass, pp. 235-241, Poreč, 2013.

[4] [G. Molnár](#), Effect of the Mesoscale Defects on the Strength Properties of Structural Glass' COST Training School "Structural Glass" Student Colloquium, pp. 15-18, Ghent,

2012.

Doctoral thesis

G. Molnár, Multi-scale modelling of structural glass, 2013. (in Hungarian)

Bibliography

- [ABAQUS 2011] ABAQUS. Abaqus documentation. Dassault Systemes, Providence, RI, USA, 2011. (Cited on page 19.)
- [Abdelouhab *et al.* 2024] S. Abdelouhab, G. H. A. Abrenica, A. Heitz, S. Meille, L. Roué, A. Boucherif and D. Machon. High-areal capacity Si architecture as an on-chip anode for lithium-ion batteries. *Energy Storage Materials*, vol. 65, page 103172, 2024. (Cited on page 74.)
- [Addressi *et al.* 2010] D. Addressi, E. Sacco and A. Paolone. Cosserat model for periodic masonry deduced by nonlinear homogenization. *European Journal of Mechanics - A/Solids*, vol. 29, no. 4, pages 724–737, 2010. (Cited on page 54.)
- [Aghababaei *et al.* 2016] R. Aghababaei, D. H. Warner and J.-F. Molinari. Critical length scale controls adhesive wear mechanisms. *Nature communications*, vol. 7, no. 1, page 11816, 2016. (Cited on page 7.)
- [Aghababaei *et al.* 2017] R. Aghababaei, D. H. Warner and J.-F. Molinari. On the debris-level origins of adhesive wear. *Proceedings of the National Academy of Sciences*, vol. 114, no. 30, pages 7935–7940, 2017. (Cited on page 7.)
- [Aicher 2010] S. Aicher. Process zone length and fracture energy of spruce wood in mode-I from size effect. *Wood and fiber science*, pages 237–247, 2010. (Cited on page 5.)
- [Aifantis 1984] E. C. Aifantis. On the Microstructural Origin of Certain Inelastic Models. *Journal of Engineering Materials and Technology*, vol. 106, no. 4, pages 326–330, 10 1984. (Cited on page 55.)
- [Akin 1994] J. E. Akin. *Finite elements for analysis and design: computational mathematics and applications series*. Elsevier, 1994. (Cited on page 81.)
- [Albaret *et al.* 2016] T. Albaret, A. Tanguy, F. Bolioli and D. Rodney. Mapping between atomistic simulations and Eshelby inclusions in the shear deformation of an amorphous silicon model. *Physical Review E*, vol. 93, page 053002, 2016. (Cited on page 43.)
- [Ambrosio & Tortorelli 1990] L. Ambrosio and V. M. Tortorelli. Approximation of functional depending on jumps by elliptic functional via Γ -convergence. *Communications on Pure and Applied Mathematics*, vol. 43, no. 8, pages 999–1036, 1990. (Cited on pages 8 and 16.)
- [Amestoy & Leblond 1992] M. Amestoy and J. B. Leblond. Crack paths in plane situations—II. Detailed form of the expansion of the stress intensity factors. *International Journal of Solids and Structures*, vol. 29, no. 4, pages 465–501, 1992. (Cited on pages 25 and 26.)
- [Argon 1979] A. S. Argon. Plastic deformation in metallic glasses. *Acta Metallurgica*, vol. 27, no. 1, pages 47 – 58, 1979. (Cited on pages 37, 42 and 43.)
- [Askari *et al.* 2020] M. Askari, D. A. Hutchins, P. J. Thomas, L. Astolfi, R. L. Watson, M. Abdi, M. Ricci, S. Laureti, L. Nie, S. Freear, R. Wildman, C. Tuck, M. Clarke, E. Woods and A. T. Clare. Additive manufacturing of metamaterials: A review. *Additive Manufacturing*, vol. 36, page 101562, 2020. (Cited on page 54.)

- [Ayatollahi & Aliha 2009] M. R. Ayatollahi and M. R. M. Aliha. Analysis of a new specimen for mixed mode fracture tests on brittle materials. *Engineering Fracture Mechanics*, vol. 76, no. 11, pages 1563–1573, 2009. (Cited on pages 25 and 64.)
- [Barbot *et al.* 2020] A. Barbot, M. Lerbinger, A. Lemaitre, D. Vandembroucq and S. Patinet. Rejuvenation and shear banding in model amorphous solids. *Physical Review E*, vol. 101, no. 3, page 033001, 2020. (Cited on page 45.)
- [Barenblatt 1959] G. I. Barenblatt. The formation of equilibrium cracks during brittle fracture. General ideas and hypotheses. Axially-symmetric cracks. *Journal of Applied Mathematics and Mechanics*, vol. 23, no. 3, pages 622–636, 1959. (Cited on pages 6 and 7.)
- [Barenblatt 1962] G. I. Barenblatt. The mathematical theory of equilibrium cracks in brittle fracture. *Advances in applied mechanics*, vol. 7, pages 55–129, 1962. (Cited on pages 6 and 7.)
- [Barthel *et al.* 2022] E. Barthel, T. Deschamps, G. Kermouche, C. Martinet, G. Molnár and A. Tanguy. Le verre: fragile ou ductile? *Reflète de la physique*, no. 74, pages 46–51, 2022. (Cited on page 100.)
- [Bauer *et al.* 2016] J. Bauer, A. Schroer, R. Schwaiger and O. Kraft. Approaching theoretical strength in glassy carbon nanolattices. *Nature materials*, vol. 15, no. 4, pages 438–443, 2016. (Cited on page 54.)
- [Bažant & Beissel 1994] Z. P. Bažant and S. Beissel. Smeared-tip superposition method for cohesive fracture with rate effect and creep. *International Journal of Fracture*, vol. 65, pages 277–290, 1994. (Cited on page 73.)
- [Bažant & Kazemi 1990] Z. P. Bažant and M. T. Kazemi. Size effect in fracture of ceramics and its use to determine fracture energy and effective process zone length. *Journal of the American Ceramic Society*, vol. 73, no. 7, pages 1841–1853, 1990. (Cited on page 5.)
- [Bažant & Pijaudier-Cabot 1989] Z. P. Bažant and G. Pijaudier-Cabot. Measurement of characteristic length of nonlocal continuum. *Journal of Engineering Mechanics*, vol. 115, no. 4, pages 755–767, 1989. (Cited on page 8.)
- [Bažant *et al.* 1986] Z. P. Bažant, J. Kim and P. Pfeiffer. Nonlinear fracture properties from size effect tests. *Journal of Structural Engineering*, vol. 112, no. 2, pages 289–307, 1986. (Cited on page 5.)
- [Bažant *et al.* 1996] Z. P. Bažant, I. M. Daniel and Z. Li. Size effect and fracture characteristics of composite laminates. *Journal of engineering materials and technology*, vol. 118, no. 3, pages 317–324, 1996. (Cited on page 5.)
- [Bažant 1984] Z. P. Bažant. Size effect in blunt fracture: concrete, rock, metal. *Journal of Engineering Mechanics*, vol. 110, no. 4, pages 518–535, 1984. (Cited on page 5.)
- [Bažant 1997] Z. P. Bažant. Scaling of quasibrittle fracture: asymptotic analysis. *International Journal of Fracture*, vol. 83, no. 1, page 19, 1997. (Cited on page 14.)
- [Bažant 1999] Z. P. Bažant. Size effect on structural strength: a review. *Archive of applied Mechanics*, vol. 69, pages 703–725, 1999. (Cited on page 5.)

- [Benallal *et al.* 1991] A. Benallal, R. Billardon and J. Lemaitre. Continuum damage mechanics and local approach to fracture: numerical procedures. *Computer Methods in Applied Mechanics and Engineering*, vol. 92, no. 2, pages 141–155, 1991. (Cited on page 8.)
- [Bendsøe & Sigmund 1999] M. P. Bendsøe and O. Sigmund. Material interpolation schemes in topology optimization. *Archive of applied mechanics*, vol. 69, no. 9, pages 635–654, 1999. (Cited on pages 66 and 67.)
- [Bendsøe 1995] M. P. Bendsøe. Optimization of structural topology, shape, and material, volume 414. Springer, 1995. (Cited on page 67.)
- [Beremin *et al.* 1983] F. M. Beremin, A. Pineau, F. Mudry, J. C. Devaux, Y. D’Escatha and P. Ledermann. A local criterion for cleavage fracture of a nuclear pressure vessel steel. *Metallurgical transactions A*, vol. 14, pages 2277–2287, 1983. (Cited on page 5.)
- [Berendsen *et al.* 1984] H. J. C. Berendsen, J. P. M. Postma, W. F. van Gunsteren, A. DiNola and J. R. Haak. Molecular dynamics with coupling to an external bath. *The Journal of Chemical Physics*, vol. 81, no. 8, pages 3684–3690, 1984. (Cited on page 82.)
- [Bergou *et al.* 2008] M. Bergou, M. Wardetzky, S. Robinson, B. Audoly and E. Grinspun. Discrete elastic rods. In *ACM SIGGRAPH 2008 papers*, pages 1–12. 2008. (Cited on page 90.)
- [Bergou *et al.* 2010] M. Bergou, B. Audoly, E. Vouga, M. Wardetzky and E. Grinspun. Discrete viscous threads. *ACM Transactions on graphics (TOG)*, vol. 29, no. 4, pages 1–10, 2010. (Cited on page ii.)
- [Bernard *et al.* 2012] P.-E. Bernard, N. Moës and N. Chevaugeon. Damage growth modeling using the Thick Level Set (TLS) approach: Efficient discretization for quasi-static loadings. *Computer Methods in Applied Mechanics and Engineering*, vol. 233, pages 11–27, 2012. (Cited on page 19.)
- [Binder & W. Kob 2005] K. Binder and W. W. Kob. Glassy materials and disordered solids: an introduction to their statistical mechanics. World Scientific, Singapore, 2005. (Cited on page 82.)
- [Bleyer & Alessi 2018] J. Bleyer and R. Alessi. Phase-field modeling of anisotropic brittle fracture including several damage mechanisms. *Computer Methods in Applied Mechanics and Engineering*, vol. 336, pages 213–236, 2018. (Cited on page 61.)
- [Bleyer & Molinari 2017] J. Bleyer and J.-F. Molinari. Microbranching instability in phase-field modelling of dynamic brittle fracture. *Applied Physics Letters*, vol. 110, no. 15, 2017. (Cited on page 30.)
- [Bleyer *et al.* 2017] J. Bleyer, C. Roux-Langlois and J.-F. Molinari. Dynamic crack propagation with a variational phase-field model: limiting speed, crack branching and velocity-toughening mechanisms. *International Journal of Fracture*, vol. 204, no. 1, pages 79–100, 2017. (Cited on page 30.)
- [Bobaru *et al.* 2016] F. Bobaru, J. T. Foster, P. H. Geubelle and S. A. Silling. Handbook of peridynamic modeling. CRC press, 2016. (Cited on page 7.)

- [Bourdin *et al.* 2000] B. Bourdin, G.A. Francfort and J.-J. Marigo. Numerical experiments in revisited brittle fracture. *Journal of the Mechanics and Physics of Solids*, vol. 48, no. 4, pages 797 – 826, 2000. (Cited on pages 8, 9, 16 and 17.)
- [Bourdin *et al.* 2008] B. Bourdin, G. A. Francfort and J.-J. Marigo. The variational approach to fracture. Springer Netherlands, 2008. (Cited on page 16.)
- [Bourdin 2001] B. Bourdin. Filters in topology optimization. *International Journal for Numerical Methods in Engineering*, vol. 50, pages 2143–2158, 2001. (Cited on page 66.)
- [Broek 1982] D. Broek. Elementary engineering fracture mechanics. Springer Science & Business Media, 1982. (Cited on page 25.)
- [Brooks 2013] Z. Brooks. Fracture process zone: Microstructure and nanomechanics in quasi-brittle materials. PhD thesis, Massachusetts Institute of Technology, 2013. (Cited on page 6.)
- [Cahn & Hilliard 1958] J. W. Cahn and J. E. Hilliard. Free energy of a nonuniform system. I. Interfacial free energy. *The Journal of chemical physics*, vol. 28, no. 2, pages 258–267, 1958. (Cited on pages 16 and 32.)
- [Caleyron *et al.* 2012] F. Caleyron, A. Combescure, V. Faucher and S. Potapov. Dynamic simulation of damage-fracture transition in smoothed particles hydrodynamics shells. *International Journal for Numerical Methods in Engineering*, vol. 90, no. 6, pages 707–738, 2012. (Cited on page 7.)
- [Camacho & Ortiz 1996] G. T. Camacho and M. Ortiz. Computational modelling of impact damage in brittle materials. *International Journal of solids and structures*, vol. 33, no. 20-22, pages 2899–2938, 1996. (Cited on page 8.)
- [Cedolin *et al.* 1983] L. Cedolin, S. Dei Poli and I. Iori. Experimental determination of the fracture process zone in concrete. *Cement and Concrete Research*, vol. 13, no. 4, pages 557–567, 1983. (Cited on page 6.)
- [Chaboche *et al.* 2001] J. L. Chaboche, F. Feyel and Y. Monerie. Interface debonding models: a viscous regularization with a limited rate dependency. *International journal of solids and structures*, vol. 38, no. 18, pages 3127–3160, 2001. (Cited on page 19.)
- [Charpentier *et al.* 2004] T. Charpentier, S. Ispas, M. Profeta, F. Mauri and C. J. Pickard. First-Principles Calculation of ^{17}O , ^{29}Si , and ^{23}Na NMR Spectra of Sodium Silicate Crystals and Glasses. *The Journal of Physical Chemistry B*, vol. 108, no. 13, pages 4147–4161, 2004. (Cited on pages 37, 83 and 84.)
- [Chen *et al.* 2010] B. Chen, Q. Yuan, J. Luo and J. H. Fan. Fibre reinforced cellular microstructure of cork wood. *Plastics, Rubber and Composites*, vol. 39, no. 2, pages 86–90, 2010. (Cited on page 54.)
- [Chen *et al.* 2015] C.-H. Chen, T. Cambonie, V. Lazarus, M. Nicoli, A. J. Pons and A. Karma. Crack front segmentation and facet coarsening in mixed-mode fracture. *Physical Review Letters*, vol. 115, no. 26, page 265503, 2015. (Cited on page 26.)
- [Chengyong *et al.* 1990] W. Chengyong, L. Peide, H. Rongsheng and S. Xiutang. Study of the fracture process zone in rock by laser speckle interferometry. *International Journal of Rock Mechanics and Mining Sciences & Geomechanics Abstracts*, vol. 27, no. 1, pages 65 – 69, 1990. (Cited on page 6.)

- [Chudnovsky 2014] A. Chudnovsky. Slow crack growth, its modeling and crack-layer approach: A review. *International Journal of Engineering Science*, vol. 83, pages 6–41, 2014. Special Issue in Honor of Alexander Chudnovsky. (Cited on page 14.)
- [Citarella & Buchholz 2008] R. Citarella and F.-G. Buchholz. Comparison of crack growth simulation by DBEM and FEM for SEN-specimens undergoing torsion or bending loading. *Engineering Fracture Mechanics*, vol. 75, no. 3-4, pages 489–509, 2008. (Cited on page 27.)
- [Cormier *et al.* 2011] Laurent Cormier, Georges Calas and Brigitte Beuneu. Structural changes between soda-lime silicate glass and melt. *Journal of Non-Crystalline Solids*, vol. 357, no. 3, pages 926–931, 2011. (Cited on page 37.)
- [Cornetti *et al.* 2013] P. Cornetti, A. Sapora and A. Carpinteri. Mode mixity and size effect in V-notched structures. *Int. J. Sol. Struct.*, vol. 50(10), pages 1562–1582, 2013. (Cited on page 7.)
- [Corre *et al.* 2021] T. Corre, M. Coret, E. Verron and B. Leblé. Non steady-state intersonic cracks in elastomer membranes under large static strain. *Journal of Theoretical, Computational and Applied Mechanics*, 2021. (Cited on page 31.)
- [Cortet *et al.* 2005] P.-P. Cortet, S. Santucci, L. Vanel and S. Ciliberto. Slow crack growth in polycarbonate films. *Europhysics Letters*, vol. 71, no. 2, page 242, 2005. (Cited on page 6.)
- [Cosserat & Cosserat 1909] E. Cosserat and F. Cosserat. *Théorie des corps déformables*. Librairie Scientifique A. Hermann et Fils, 1909. (Cited on page 54.)
- [Cotterell 2002] B. Cotterell. The past, present, and future of fracture mechanics. *Engineering fracture mechanics*, vol. 69, no. 5, pages 533–553, 2002. (Cited on page 6.)
- [Cox & Scholz 1988] S. J. D. Cox and C. H. Scholz. On the formation and growth of faults: an experimental study. *Journal of Structural Geology*, vol. 10, no. 4, pages 413–430, 1988. (Cited on page 26.)
- [da Vinci 1504] L. da Vinci. *Codex atlanticus*. Biblioteca Ambrosiana, 1504. (Cited on page 4.)
- [Dasgupta *et al.* 2012] R. Dasgupta, H. G. E. Hentschel and I. Procaccia. Microscopic mechanism of shear bands in amorphous solids. *Physical Review Letters*, vol. 109, page 255502, 2012. (Cited on page 43.)
- [de Borst *et al.* 1996] R. de Borst, A. Benallal and O. M. Heeres. A gradient-enhanced damage approach to fracture. *Le Journal de Physique IV*, vol. 6, no. C6, pages 491–502, 1996. (Cited on page 8.)
- [de Borst 2002] R. de Borst. Fracture in quasi-brittle materials: a review of continuum damage-based approaches. *Engineering fracture mechanics*, vol. 69, no. 2, pages 95–112, 2002. (Cited on page 8.)
- [Dempsey *et al.* 1999] J. P. Dempsey, R. M. Adamson and S. V. Mulmule. Scale effects on the in-situ tensile strength and fracture of ice. Part II: First-year sea ice at Resolute, NWT. *International Journal of Fracture*, vol. 95, no. 1, pages 347–366, 1999. (Cited on page 5.)

- [Denarie *et al.* 2001] E. Denarie, V. E. Saouma, A. Iocco and D. Varelas. Concrete fracture process zone characterization with fiber optics. *Journal of engineering mechanics*, vol. 127, no. 5, pages 494–502, 2001. (Cited on page 6.)
- [der Waals 1873] J. D. Van der Waals. On the Continuity of the Gaseous and Liquid States. PhD thesis, Leiden, 1873. (Cited on page 3.)
- [Deschamps *et al.* 2011] T. Deschamps, C. Martinet, J. L. Bruneel and B. Champagnon. Soda-lime silicate glass under hydrostatic pressure and indentation: a micro-Raman study. *Journal of Physics: Condensed Matter*, vol. 23, no. 3, page 035402, 2011. (Cited on pages 36 and 39.)
- [Deschamps *et al.* 2013] T. Deschamps, A. Kassir-Bodon, C. Sonnevile nad J. Margueritat nad C. Martinet, D. de Ligny, A. Mermet and B. Champagnon. Permanent densification of compressed silica glass: a Raman-density calibration curve. *Journal of Physics: Condensed Matter*, vol. 25, no. 2, page 025402, 2013. (Cited on pages 36 and 37.)
- [Deschamps *et al.* 2014] T. Deschamps, J. Margueritat, C. Martinet, A. Mermet and B. Champagnon. Elastic Moduli of Permanently Densified Silica Glasses. *Scientific Reports*, vol. 4, 2014. (Cited on page 38.)
- [Deschamps *et al.* 2022] T. Deschamps, C. Martinet, B. Champagnon, G. Molnár and E. Barthel. Memory effect in the plasticity of a silicate glass densified at room temperature. *Physical Review B*, vol. 105, no. 22, page 224206, 2022. (Cited on pages iv and 100.)
- [Dietrich & Newsam 1997] C. R. Dietrich and G. N. Newsam. Fast and Exact Simulation of Stationary Gaussian Processes through Circulant Embedding of the Covariance Matrix. *SIAM Journal on Scientific Computing*, vol. 18, no. 4, pages 1088–1107, 1997. (Cited on page 28.)
- [Djeumen *et al.* 2022] E. Djeumen, G. Molnár, N. Tardif, M. Coret, J. Desquines, T. Taurines and M.-C. Baietto. Modeling diffusive phase transformation and fracture in viscoplastic materials. *International Journal of Solids and Structures*, vol. 252, page 111757, 2022. (Cited on pages iii, 32 and 100.)
- [Djeumen 2022] E. Djeumen. Étude du comportement au fluage des gaines en alliage de zirconium pré-oxydées sous sollicitations thermomécaniques représentatives d'un accident de perte de réfrigérant primaire. PhD thesis, Université de Lyon, 2022. (Cited on page 32.)
- [Doitrand & Leguillon 2018a] A. Doitrand and D. Leguillon. 3D application of the coupled criterion to crack initiation prediction in epoxy/aluminum specimens under four point bending. *Int. J. Sol. Struct.*, vol. 143, pages 175–182, 2018. (Cited on page 7.)
- [Doitrand & Leguillon 2018b] A. Doitrand and D. Leguillon. 3D application of the coupled criterion to crack initiation prediction in epoxy/aluminum specimens under four point bending. *International Journal of Solids and Structures*, vol. 143, pages 175–182, 2018. (Cited on page 27.)
- [Doitrand & Leguillon 2018c] A. Doitrand and D. Leguillon. Comparison between 2D and 3D applications of the coupled criterion to crack initiation prediction in scarf adhesive joints. *Int. J. Adh. Adh.*, vol. 85, pages 69–76, 2018. (Cited on page 7.)

- [Doitrand & Leguillon 2018d] A. Doitrand and D. Leguillon. Numerical modeling of the nucleation of facets ahead of a primary crack under mode I+III. *Int. J. Fract.*, vol. 123(1), pages 37–50, 2018. (Cited on page 7.)
- [Doitrand & Sapora 2020] A. Doitrand and A. Sapora. Nonlinear implementation of Finite Fracture Mechanics: A case study on notched Brazilian disk samples. *Int. J. Non-Linear Mech.*, vol. 119, page 103245, 2020. (Cited on pages 5 and 7.)
- [Doitrand *et al.* 2017] A. Doitrand, C. Fagiano, N. Carrère, V. Chiaruttini and M. Hirsekorn. Damage onset modeling in woven composites based on a coupled stress and energy criterion. *Engng. Fract. Mech.*, vol. 169, pages 189–200, 2017. (Cited on page 7.)
- [Doitrand *et al.* 2022] A. Doitrand, G. Molnár, D. Leguillon, E. Martin and N. Carrère. Dynamic crack initiation assessment with the coupled criterion. *European Journal of Mechanics - A/Solids*, vol. 93, page 104483, 2022. (Cited on pages iii, 30 and 100.)
- [Doitrand *et al.* 2023a] A. Doitrand, D. Leguillon, G. Molnár and V. Lazarus. Revisiting facet nucleation under mixed mode I+ III loading with T-stress and mode-dependent fracture properties. *International Journal of Fracture*, vol. 242, no. 1, pages 85–106, 2023. (Cited on pages iii and 99.)
- [Doitrand *et al.* 2023b] A. Doitrand, G. Molnár, R. Estevez and A. Gravouil. Strength-based regularization length in phase field fracture. *Theoretical and Applied Fracture Mechanics*, vol. 124, page 103728, 2023. (Cited on pages iii and 99.)
- [Doitrand *et al.* 2024] A. Doitrand, T. Duminy, H. Girard and X. Chen. A review of the coupled criterion. *Journal of Theoretical, Computational and Applied Mechanics*, 2024. (Cited on page 16.)
- [Drucker 1959] D. C. Drucker. A definition of a stable inelastic material. *ASME Journal of Applied Mechanics*, vol. 26, page 101–195, 1959. (Cited on page 41.)
- [Du *et al.* 1990] J. J. Du, A. S. Kobayashi and N. M. Hawkins. An experimental-numerical analysis of fracture process zone in concrete fracture specimens. *Engineering Fracture Mechanics*, vol. 35, no. 1-3, pages 15–27, 1990. (Cited on page 6.)
- [Du *et al.* 2021] T. Du, M. Blum, C. Chen, M. G. Muraleedharan, A. C. T. van Duin and P. Newell. Nanomechanical investigation of the interplay between pore morphology and crack orientation of amorphous silica. *Engineering Fracture Mechanics*, vol. 250, page 107749, 2021. (Cited on page 47.)
- [Dugdale 1960] D. S. Dugdale. Yielding of steel sheets containing slits. *Journal of the Mechanics and Physics of Solids*, vol. 8, no. 2, pages 100–104, 1960. (Cited on pages 6 and 7.)
- [Eid *et al.* 2023] E. Eid, A. Gravouil and G. Molnár. Influence of rate-dependent damage phase-field on the limiting crack-tip velocity in dynamic fracture. *Engineering Fracture Mechanics*, vol. 292, page 109620, 2023. (Cited on pages iii, 31 and 99.)
- [Elingaard *et al.* 2022] M. O. Elingaard, N. Aage, J. A. Bærentzen and O. Sigmund. De-homogenization using convolutional neural networks. *Computer Methods in Applied Mechanics and Engineering*, vol. 388, page 114197, 2022. (Cited on page 74.)

- [Emerson *et al.* 1989] J. F. Emerson, P. E. Stallworth and P. J. Bray. High-field ^{29}Si NMR studies of alkali silicate glasses. *Journal of Non-Crystalline Solids*, vol. 113, no. 2–3, pages 253–259, 1989. (Cited on pages 37, 83 and 84.)
- [Erdogan & Sih 1963] F. Erdogan and G. C. Sih. On the crack extension in plates under plane loading and transverse shear. *Journal of Basic Engineering*, vol. 85, pages 519–525, 1963. (Cited on pages 22, 23 and 25.)
- [Eshelby 1957] J. D. Eshelby. The Determination of the Elastic Field of an Ellipsoidal Inclusion, and Related Problems. *Proceedings of the Royal Society of London*, vol. 241, page 376, 1957. (Cited on page 43.)
- [Evans 1978] A. G. Evans. A general approach for the statistical analysis of multiaxial fracture. *Journal of the American Ceramic Society*, vol. 61, no. 7-8, pages 302–308, 1978. (Cited on page 5.)
- [Fábián *et al.* 2007] M. Fábián, P. Jóvári, E. Sváb, Gy. Mészáros, T. Proffen and E. Veress. Network structure of $0.7\text{SiO}_2\text{-}0.3\text{Na}_2\text{O}$ glass from neutron and X-ray diffraction and RMC modelling. *Journal of Physics: Condensed Matter*, vol. 19, no. 33, page 335209, 2007. (Cited on pages 37 and 83.)
- [Fakhimi & Wan 2016] A. Fakhimi and F. Wan. Discrete element modeling of the process zone shape in mode I fracture at peak load and in post-peak regime. *International Journal of Rock Mechanics and Mining Sciences*, vol. 85, pages 119–128, 2016. (Cited on page 7.)
- [Falk & Langer 1998] M. L. Falk and J.-S. Langer. Dynamics of viscoplastic deformation in amorphous solids. *Physical Review E*, vol. 57, pages 7192–7205, 1998. (Cited on page 43.)
- [Falk & Maloney 2010] M. L. Falk and C. E. Maloney. Simulating the mechanical response of amorphous solids using atomistic methods. *The European Physical Journal B*, vol. 75, no. 4, pages 405–413, 2010. (Cited on page 41.)
- [Faria Ricardo *et al.* 2020] L. F. Faria Ricardo, D. Leguillon, G. Parry and A. Doitrand. Modeling the thermal shock induced cracking in ceramics. *Journal of the European Ceramic Society*, vol. 40, no. 4, pages 1513–1521, 2020. (Cited on page 15.)
- [Feldmann *et al.* 2023] M. Feldmann, M. Laurs, J. Belis, N. Buljan, A. Criaud, E. Dupont, M. Eliasova, L. Galuppi, P. Hassinen, R. Kasper, C. Louter, G. Manara, A. Minne, T. Morgan, G. Pisano, M. Overend, G. Royer-Carfagni, J. Schneider, G. Schwind, C. Schuler, G. Siebert and A. Sikynova. The new CEN/TS 19100: Design of glass structures. *Glass Structures & Engineering*, vol. 8, no. 3, pages 317–337, 2023. (Cited on page ii.)
- [Field *et al.* 2003] J. S. Field, M. V. Swain and R. D. Dukino. Determination of fracture toughness from the extra penetration produced by indentation-induced pop-in. *Journal of Materials Research*, vol. 18, pages 1412–1419, 2003. (Cited on page 39.)
- [Fleck *et al.* 2010] N. A. Fleck, V. S. Deshpande and M. F. Ashby. Micro-architected materials: past, present and future. *Proceedings of the Royal Society A: Mathematical, Physical and Engineering Sciences*, vol. 466, no. 2121, pages 2495–2516, 2010. (Cited on page 10.)

- [Forest & Sab 1998] S. Forest and K. Sab. Cosserat overall modeling of heterogeneous materials. *Mechanics research communications*, vol. 25, no. 4, pages 449–454, 1998. (Cited on page 56.)
- [Forest *et al.* 2001] S. Forest, F. Pradel and K. Sab. Asymptotic analysis of heterogeneous Cosserat media. *International Journal of Solids and Structures*, vol. 38, no. 26-27, pages 4585–4608, 2001. (Cited on pages 55 and 56.)
- [Forest 1998] S. Forest. Mechanics of generalized continua: construction by homogenization. *Le Journal de Physique IV*, vol. 8, no. PR4, pages Pr4–39, 1998. (Cited on page 56.)
- [Forest 2002] S. Forest. Homogenization methods and mechanics of generalized continua—Part 2. Theoretical and applied mechanics, no. 28-29, pages 113–144, 2002. (Cited on page 56.)
- [Francfort & Marigo 1998] G.A. Francfort and J.-J. Marigo. Revisiting brittle fracture as an energy minimization problem. *Journal of the Mechanics and Physics of Solids*, vol. 46, no. 8, pages 1319 – 1342, 1998. (Cited on pages 8 and 16.)
- [Freddi & Royer-Carfagni 2010] F. Freddi and G. Royer-Carfagni. Regularized variational theories of fracture: A unified approach. *Journal of the Mechanics and Physics of Solids*, vol. 58, no. 8, pages 1154 – 1174, 2010. (Cited on page 14.)
- [Frenkel & Smit 2002] D. Frenkel and B. Smit. *Understanding molecular simulations*. Academic Press, London, 2002. (Cited on page 82.)
- [Freudenthal 1946] A. M. Freudenthal. The statistical aspect of fatigue of materials. *Proceedings of the Royal Society of London. Series A. Mathematical and Physical Sciences*, vol. 187, no. 1011, pages 416–429, 1946. (Cited on page 5.)
- [Freund & Freud 1998] L. B. Freund and L. B. Freund. *Dynamic fracture mechanics*. Cambridge university press, 1998. (Cited on page 29.)
- [Fusco *et al.* 2010] C. Fusco, T. Albaret and A. Tanguy. Role of local order in the small-scale plasticity of model amorphous materials. *Physical Review E*, vol. 82, page 066116, 2010. (Cited on page 43.)
- [Fusco *et al.* 2014] C. Fusco, T. Albaret and A. Tanguy. Rheological properties vs. local dynamics in model disordered materials at low temperature. *The European Physical Journal E*, vol. 37, no. 5, 2014. (Cited on page 43.)
- [Galilei 1638] G. Galilei. *Discourses and mathematical demonstrations relating to two new sciences*. Leiden: Louis Elsevier, 1638. (Cited on page 4.)
- [García *et al.* 2016] I. G. García, B. J. Carter, A. R. Ingraffea and V. Mantič. A numerical study of transverse cracking in cross-ply laminates by 3D finite fracture mechanics. *Compos. Part B*, vol. 95, pages 475–487, 2016. (Cited on page 7.)
- [García *et al.* 2018] I. G. García, V. Mantič and A. Blázquez. The effect of residual thermal stresses on transverse cracking in cross-ply laminates: an application of the coupled criterion of the finite fracture mechanics. *Int. J. Fract.*, vol. 211, pages 61–74, 2018. (Cited on page 7.)
- [Geelen *et al.* 2019] R. J. M. Geelen, Y. Liu, T. Hu, M. R. Tupek and J. E. Dolbow. A phase-field formulation for dynamic cohesive fracture. *Computer Methods in Applied Mechanics and Engineering*, vol. 348, pages 680–711, 2019. (Cited on page 20.)

- [Geers *et al.* 1998] M. G. D. Geers, R. de Borst, W. A. M. Brekelmans and R. H. J. Peerlings. Strain-based transient-gradient damage model for failure analyses. *Computer methods in applied mechanics and engineering*, vol. 160, no. 1-2, pages 133–153, 1998. (Cited on page 8.)
- [Geers *et al.* 2001] M. G. D. Geers, V. Kouznetsova and W. A. M. Brekelmans. Gradient-enhanced computational homogenization for the micro-macro scale transition. *Le Journal de Physique IV*, vol. 11, pages 145–152, 2001. (Cited on page 57.)
- [Geoffroy-Donders 2018] P. Geoffroy-Donders. Homogenization method for topology optimization of structures built with lattice materials. PhD thesis, Ecole Polytechnique, 2018. (Cited on page 74.)
- [Gerasimov & De Lorenzis 2016] T. Gerasimov and L. De Lorenzis. A line search assisted monolithic approach for phase-field computing of brittle fracture. *Computer Methods in Applied Mechanics and Engineering*, vol. 312, pages 276–303, 2016. (Cited on page 19.)
- [Ginzburg & Landau 1950] V. L. Ginzburg and L. D. Landau. Theory of superconductivity. *Zh. Eksp. Teor. Fiz.:(USSR)*, vol. 20, no. 12, 1950. (Cited on page 16.)
- [Goldenberg *et al.* 2007] C. Goldenberg, A. Tanguy and J.-L. Barrat. Particle displacements in the elastic deformation of amorphous materials: Local fluctuations vs. non-affine field. *Europhysics Letters*, vol. 80, no. 1, page 16003, 2007. (Cited on pages 37 and 43.)
- [Goldhirsch & Goldenberg 2002] I. Goldhirsch and C. Goldenberg. On the microscopic foundations of elasticity. *The European Physics Journal E*, vol. 9, no. 3, pages 245–251, 2002. (Cited on pages 37 and 85.)
- [Goldstein & Osipenko 2012] R. V. Goldstein and N. M. Osipenko. Fracture structure near a longitudinal shear macrorupture. *Mechanics of Solids*, vol. 47, pages 505–516, 2012. (Cited on page 26.)
- [Gravouil *et al.* 2002] A. Gravouil, N. Moës and T. Belytschko. Non-planar 3D crack growth by the extended finite element and level sets—Part II: Level set update. *International journal for numerical methods in engineering*, vol. 53, no. 11, pages 2569–2586, 2002. (Cited on page 27.)
- [Griffith 1921] A. A. Griffith. The Phenomena of Rupture and Flow in Solids. *Philosophical Transactions of the Royal Society of London A: Mathematical, Physical and Engineering Sciences*, vol. 221, no. 582-593, pages 163–198, 1921. (Cited on pages 4, 5, 8, 16, 17 and 47.)
- [Griffith 1924] A. Griffith. The theory of rupture. In *First Int. Cong. Appl. Mech*, pages 55–63, 1924. (Cited on pages 8 and 16.)
- [Gross & Tomozawa 2008] T. M. Gross and M. Tomozawa. Fictive temperature-independent density and minimum indentation size effect in calcium aluminosilicate glass. *Journal of Applied Physics*, vol. 104, no. 6, 2008. (Cited on page 44.)

- [Guo *et al.* 1993] Z. K. Guo, A. S. Kobayashi and N. M. Hawkins. Further studies on fracture process zone for mode I concrete fracture. *Engineering fracture mechanics*, vol. 46, no. 6, pages 1041–1049, 1993. (Cited on page 6.)
- [Haidar *et al.* 2005] K. Haidar, G. Pijaudier-Cabot, J.-F. Dubé and A. Loukili. Correlation between the internal length, the fracture process zone and size effect in model materials. *Materials and structures*, vol. 38, no. 2, page 201, 2005. (Cited on page 6.)
- [Hao & Hossain 2019] T. Hao and Z. M. Hossain. Atomistic mechanisms of crack nucleation and propagation in amorphous silica. *Phys. Rev. B*, vol. 100, page 014204, 2019. (Cited on page 47.)
- [Hardy 1982] R. J. Hardy. Formulas for determining local properties in molecular-dynamics simulations: Shock waves. *The Journal of Chemical Physics*, vol. 76, no. 1, pages 622–628, 1982. (Cited on page 37.)
- [Hayashi & Nemat-Nasser 1981] K. Hayashi and S. Nemat-Nasser. Energy-Release Rate and Crack Kinking Under Combined Loading. *Journal of Applied Mechanics*, vol. 48, no. 3, pages 520–524, 1981. (Cited on page 25.)
- [Hilber *et al.* 1977] H. M. Hilber, T. J. R. Hughes and R. L. Taylor. Improved numerical dissipation for time integration algorithms in structural dynamics. *Earthquake Engineering & Structural Dynamics*, vol. 5, no. 3, pages 283–292, 1977. (Cited on page 30.)
- [Hillerborg *et al.* 1976] A. Hillerborg, M. Mordéer and P. E. Petersson. Analysis of crack formation and crack growth in concrete by means of fracture mechanics and finite elements. *Cement Concrete Res*, vol. 6, pages 773–782, 1976. (Cited on page 8.)
- [Hockney & Eastwood 2021] R. W. Hockney and J. W. Eastwood. *Computer simulation using particles*. crc Press, 2021. (Cited on page 36.)
- [Holzapfel 2001] G. A. Holzapfel. *Nonlinear solid mechanics*. Wiley, 2001. (Cited on page 37.)
- [Hull 1994] D. Hull. The effect of mixed mode I/III on crack evolution in brittle solids. *International journal of fracture*, vol. 70, pages 59–79, 1994. (Cited on page 26.)
- [Irwin 1948] G. R. Irwin. Fracture dynamics, 1948. (Cited on page 6.)
- [Irwin 1957] G. R. Irwin. Relation of stresses near a crack to the crack extension force. 9th Cong. App. Mech., Brussels, 1957. (Cited on page 6.)
- [Irwin 1958] R. G. Irwin. *Fracture*, pages 551–590. Springer Berlin Heidelberg, Berlin, Heidelberg, 1958. (Cited on pages 4, 5, 6, 9, 14, 16, 21, 22 and 23.)
- [Issa *et al.* 2000] M. A. Issa, M. A. Issa, M. S. Islam and A. Chudnovsky. Size effects in concrete fracture: Part I, experimental setup and observations. *International Journal of Fracture*, vol. 102, no. 1, pages 1–24, 2000. (Cited on page 14.)
- [Jacon *et al.* 2023] A. Jacon, B. Prabel, G. Molnár, J. Bluthé and A. Gravouil. Adaptive mesh refinement and cycle jumps for phase-field fatigue fracture modeling. *Finite Elements in Analysis and Design*, vol. 224, page 104004, 2023. (Cited on pages 19 and 99.)

- [Jackowska-Strumillo *et al.* 1999] L. Jackowska-Strumillo, J. Sokolowski and A. Zochowski. The topological derivative method in shape optimization. In Proceedings of the 38th IEEE Conference on Decision and Control (Cat. No.99CH36304), volume 1, pages 674–679 vol.1, 1999. (Cited on page 66.)
- [Jan 2016] Y. Jan. Modélisation de la propagation de fissure sur des structures minces, soumises à des sollicitations intenses et rapides, par la méthode X-FEM. PhD thesis, Ecole doctorale MEGA, 2016. (Cited on page 7.)
- [Jang *et al.* 2013] D. Jang, L. R. Meza, F. Greer and J. R. Greer. Fabrication and deformation of three-dimensional hollow ceramic nanostructures. *Nature materials*, vol. 12, no. 10, pages 893–898, 2013. (Cited on page 54.)
- [Janssen *et al.* 2004] M. Janssen, J. Zuidema and R. Wanhill. *Fracture mechanics: fundamentals and applications*. CRC Press, 2004. (Cited on page 3.)
- [Ji *et al.* 2006] H. Ji, V. Keryvin, T. Rouxel and T. Hammouda. Densification of window glass under very high pressure and its relevance to Vickers indentation. *Scripta Materialia*, vol. 55, no. 12, pages 1159–1162, 2006. (Cited on pages 36 and 39.)
- [Ji *et al.* 2022] J. Ji, M. Zhang, J. Zeng and F. Tian. Uncovering the intrinsic deficiencies of phase-field modeling for dynamic fracture. *International Journal of Solids and Structures*, vol. 256, page 111961, 2022. (Cited on pages 30 and 31.)
- [Jirásek & Rolshoven 2009] M. Jirásek and S. Rolshoven. Localization properties of strain-softening gradient plasticity models. Part II: Theories with gradients of internal variables. *International Journal of Solids and Structures*, vol. 46, no. 11-12, pages 2239–2254, 2009. (Cited on page 47.)
- [K. Ammar & Forest 2009] G. Cailletaud K. Ammar B. Appolaire and S. Forest. Combining phase field approach and homogenization methods for modelling phase transformation in elastoplastic media. *European Journal of Computational Mechanics*, vol. 18, no. 5-6, pages 485–523, 2009. (Cited on page 32.)
- [Kachanov 1958] L. M. Kachanov. Rupture time under creep conditions. 1958. (Cited on pages 8 and 16.)
- [Kalthoff & Winkler 1988] J. F. Kalthoff and S. Winkler. Failure mode transition at high rates of shear loading. DGM Informationsgesellschaft mbH, *Impact Loading and Dynamic Behavior of Materials*, vol. 1, pages 185–195, 1988. (Cited on page 30.)
- [Karlsson *et al.* 2005] C. Karlsson, E. Zanghellini, J. Swenson, B. Roling, D. Bowron and L. Börjesson. Structure of mixed alkali/alkaline-earth silicate glasses from neutron diffraction and vibrational spectroscopy. *Physical Review B*, vol. 72, page 064206, 2005. (Cited on page 37.)
- [Karmakar *et al.* 2010] S. Karmakar, A. Lemaître, E. Lerner and I. Procaccia. Predicting Plastic Flow Events in Athermal Shear-Strained Amorphous Solids. *Physical Review Letters*, vol. 104, page 215502, 2010. (Cited on page 37.)
- [Kermouche *et al.* 2008] G. Kermouche, E. Barthel, D. Vandembroucq and P. Dubujet. Mechanical modelling of indentation-induced densification in amorphous silica. *Acta Materialia*, vol. 56, no. 13, pages 3222 – 3228, 2008. (Cited on pages 10 and 42.)

- [Kermouche *et al.* 2016] G. Kermouche, G. Guillonneau, J. Michler, J. Teisseire and E. Barthel. Perfectly plastic flow in silica glass. *Acta Materialia*, vol. 114, pages 146–153, 2016. (Cited on page 39.)
- [Kerrache *et al.* 2006] A. Kerrache, V. Teboul and A. Monteil. Screening dependence of the dynamical and structural properties of BKS silica. *Chemical Physics*, vol. 321, no. 1–2, pages 69–74, 2006. (Cited on page 82.)
- [Keryvin *et al.* 2014] V. Keryvin, J.-X. Meng, S. Gicquel, J.-P. Guin, L. Charleux, J.-C. Sangleboeuf, P. Pilvin, T. Rouxel and G. Le Quilliec. Constitutive modeling of the densification process in silica glass under hydrostatic compression. *Acta Materialia*, vol. 62, pages 250–257, 2014. (Cited on pages 38 and 42.)
- [Kim *et al.* 1998] S. G. Kim, W. T. Kim and T. Suzuki. Interfacial compositions of solid and liquid in a phase-field model with finite interface thickness for isothermal solidification in binary alloys. *Phys. Rev. E*, vol. 58, pages 3316–3323, 1998. (Cited on page 32.)
- [Kimoto *et al.* 1985] H. Kimoto, S. Usami and H. Miyata. Flaw Size Dependence in Fracture Stress of Glass and Polycrystalline Ceramics. *Transactions of the Japan Society of Mechanical Engineers Series A*, vol. 51, no. 471, pages 2482–2488, 1985. (Cited on page 5.)
- [Kimura *et al.* 2015] H. Kimura, K. Wada, H. Senshu and H. Kobayashi. Cohesion of amorphous silica spheres: Toward a better understanding of the coagulation growth of silicate dust aggregates. *The Astrophysical Journal*, vol. 812, no. 1, page 67, 2015. (Cited on page 50.)
- [Kirkaldy 1864] D. Kirkaldy. Results of an experimental inquiry into the tensile strength and other properties of various kinds of wrought-iron and steel. Private publication, 1864. (Cited on page 4.)
- [Kittl & Díaz 1990] P. Kittl and G. Díaz. Size effect on fracture strength in the probabilistic strength of materials. *Reliability Engineering & System Safety*, vol. 28, no. 1, pages 9–21, 1990. (Cited on page 5.)
- [Klinsmann *et al.* 2015] M. Klinsmann, D. Rosato, M. Kamlah and R.-M. McMeeking. An assessment of the phase field formulation for crack growth. *Computer Methods in Applied Mechanics and Engineering*, vol. 294, pages 313–330, 2015. (Cited on page 24.)
- [Knauss 1970] W. G. Knauss. An observation of crack propagation in anti-plane shear. *International Journal of Fracture Mechanics*, vol. 6, no. 2, pages 183–187, 1970. (Cited on pages 26 and 28.)
- [Kolpakov & Rakin 2020] AG Kolpakov and SI Rakin. Homogenized strength criterion for composite reinforced with orthogonal systems of fibers. *Mechanics of Materials*, vol. 148, page 103489, 2020. (Cited on page 58.)
- [Kouznetsova *et al.* 2002] V. Kouznetsova, M. G. D. Geers and W. A. M. Brekelmans. Multi-scale constitutive modelling of heterogeneous materials with a gradient-enhanced computational homogenization scheme. *International journal for numerical methods in engineering*, vol. 54, no. 8, pages 1235–1260, 2002. (Cited on page 57.)

- [Kumar & Lopez-Pamies 2020] A. Kumar and O. Lopez-Pamies. The phase-field approach to self-healable fracture of elastomers: A model accounting for fracture nucleation at large, with application to a class of conspicuous experiments. *Theoretical and Applied Fracture Mechanics*, vol. 107, page 102550, 2020. (Cited on page 14.)
- [Kumar *et al.* 2020] A. Kumar, B. Bourdin, G. A. Francfort and O. Lopez-Pamies. Revisiting nucleation in the phase-field approach to brittle fracture. *Journal of the Mechanics and Physics of Solids*, vol. 142, page 104027, 2020. (Cited on page 14.)
- [Labuz *et al.* 1983] J. F. Labuz, S. P. Shah and C. H. Dowding. Post peak tensile load-displacement response and the fracture process zone in rock. In *The 24th US Symposium on Rock Mechanics (USRMS)*. American Rock Mechanics Association, 1983. (Cited on page 6.)
- [Labuz *et al.* 1987] J. F. Labuz, S. P. Shah and C. H. Dowding. The fracture process zone in granite: evidence and effect. In *International Journal of Rock Mechanics and Mining Sciences & Geomechanics Abstracts*, volume 24, pages 235–246, 1987. (Cited on page 6.)
- [Lakes & Saha 1979] R. Lakes and S. Saha. Cement line motion in bone. *Science*, vol. 204, no. 4392, pages 501–503, 1979. (Cited on page 54.)
- [Lakes 1991] R. Lakes. Experimental Micro Mechanics Methods for Conventional and Negative Poisson's Ratio Cellular Solids as Cosserat Continua. *Journal of Engineering Materials and Technology*, vol. 113, no. 1, pages 148–155, 1991. (Cited on page 54.)
- [Lakes 1993] R. Lakes. Materials with structural hierarchy. *Nature*, vol. 361, no. 6412, pages 511–515, 1993. (Cited on page 54.)
- [Lambropoulos *et al.* 1996] J. C. Lambropoulos, S. Xu and T. Fang. Constitutive Law for the Densification of Fused Silica, with Applications in Polishing and Microgrinding. *Journal of the American Ceramic Society*, vol. 79, no. 6, pages 1441–1452, 1996. (Cited on page 42.)
- [Lang & Potthoff 2011] A. Lang and J. Potthoff. Fast simulation of Gaussian random fields. 2011. (Cited on page 28.)
- [Lazarus *et al.* 2008] V. Lazarus, F.-G. Buchholz, M. Fulland and J. Wiebesiek. Comparison of predictions by mode II or mode III criteria on crack front twisting in three or four point bending experiments. *International journal of fracture*, vol. 153, no. 2, pages 141–151, 2008. (Cited on page 26.)
- [Lebihain *et al.* 2021] Mathias Lebihain, Laurent Ponson, Djimédo Kondo and Jean-Baptiste Leblond. Effective toughness of disordered brittle solids: A homogenization framework. *Journal of the Mechanics and Physics of Solids*, vol. 153, page 104463, 2021. (Cited on page 59.)
- [Leblond *et al.* 2011] J.-B. Leblond, A. Karma and V. Lazarus. Theoretical analysis of crack front instability in mode I+III. *Journal of the Mechanics and Physics of Solids*, vol. 59, no. 9, pages 1872–1887, 2011. (Cited on page 28.)
- [Leblond 1989] J. B. Leblond. Crack paths in plane situations—I. General form of the expansion of the stress intensity factors. *International Journal of Solids and Structures*, vol. 25, no. 11, pages 1311–1325, 1989. (Cited on page 25.)

- [Leguillon & Yosibash 2003] D. Leguillon and Z. Yosibash. Crack onset at a V-notch. Influence of the notch tip radius. International journal of fracture, vol. 122, pages 1–21, 2003. (Cited on page 16.)
- [Leguillon & Yosibash 2017] D. Leguillon and Z. Yosibash. Failure initiation at V-notch tips in quasi-brittle materials. Int. J. Solids Struct., vol. 122–123, page 1–13, 2017. (Cited on page 7.)
- [Leguillon *et al.* 2007] D. Leguillon, D. Quesada, C. Putot and E. Martin. Size effects for crack initiation at blunt notches or cavities. Engng. Fract. Mech., vol. 74, page 2420–2436, 2007. (Cited on page 7.)
- [Leguillon *et al.* 2018] D. Leguillon, E. Martin, O. Seveček and R. Bermejo. What is the tensile strength of a ceramic to be used in numerical models for predicting crack initiation? Int. J. Fract., vol. 212(1), pages 89–103, 2018. (Cited on pages 5 and 7.)
- [Leguillon 2002] D. Leguillon. Strength or toughness? A criterion for crack onset at a notch. Eur. J. Mech. - A/Solids, vol. 21(1), pages 61–72, 2002. (Cited on pages 6, 9, 14, 15 and 16.)
- [Leguillon 2014] D. Leguillon. An attempt to extend the 2D coupled criterion for crack nucleation in brittle materials to the 3D case. Theoretical and Applied Fracture Mechanics, vol. 74, pages 7–17, 2014. (Cited on page 27.)
- [Lei *et al.* 1998] Y. Lei, N. P. O’Dowd, E. P. Busso and G. A. Webster. Weibull stress solutions for 2-D cracks in elastic and elastic-plastic materials. International Journal of Fracture, vol. 89, pages 245–268, 1998. (Cited on page 5.)
- [Leistikow & Schanz 1987] S. Leistikow and G. Schanz. Oxidation kinetics and related phenomena of zircaloy-4 fuel cladding exposed to high temperature steam and hydrogen-steam mixtures under PWR accident conditions. Nuclear Engineering and Design, vol. 103, no. 1, pages 65–84, 1987. (Cited on page 32.)
- [Lemaître & Chaboche 2004] A. Lemaître and J.-L. Chaboche. Mécanique des matériaux solides. Dunod, 2004. (Cited on page 37.)
- [Lemaitre 1984] J. Lemaitre. How to use damage mechanics. Nuclear engineering and design, vol. 80, no. 2, pages 233–245, 1984. (Cited on page 8.)
- [Léonforte *et al.* 2005] F. Léonforte, R. Boissière, A. Tanguy, J. Wittmer and J. L. Barlat. Continuum limit of amorphous elastic bodies. III. Three-dimensional systems. Physical Review B, vol. 72, page 224206, 2005. (Cited on page 84.)
- [Li *et al.* 2010] X. Li, Q. Liu and J. Zhang. A micro–macro homogenization approach for discrete particle assembly–Cosserat continuum modeling of granular materials. International Journal of Solids and Structures, vol. 47, no. 2, pages 291–303, 2010. (Cited on page 54.)
- [Li *et al.* 2019] J. Li, D. Leguillon, E. Martin and X.-B. Zhang. Numerical implementation of the coupled criterion for damaged materials. International Journal of Solids and Structures, vol. 165, pages 93–103, 2019. (Cited on page 7.)
- [Li *et al.* 2022] Z. Li, X. Hou, Y. Ke and M. Tao. Topology optimization with a genetic algorithm for the structural design of composite porous acoustic materials. Applied Acoustics, vol. 197, page 108917, 2022. (Cited on page 74.)

- [Liebenstein & Zaiser 2018] S. Liebenstein and M. Zaiser. Determining Cosserat constants of 2D cellular solids from beam models. *Materials Theory*, vol. 2, no. 1, pages 1–20, 2018. (Cited on page 56.)
- [Lin *et al.* 2010] B. Lin, M. E. Mear and K. Ravi-Chandar. Criterion for initiation of cracks under mixed-mode I+III loading. *International journal of fracture*, vol. 165, pages 175–188, 2010. (Cited on page 26.)
- [Liu *et al.* 2020] Y. Liu, C. Deng and B. Gong. Discussion on equivalence of the theory of critical distances and the coupled stress and energy criterion for fatigue limit prediction of notched specimens. *Int. J. Fat.*, vol. 131, page 105236, 2020. (Cited on page 7.)
- [Lorentz & Benallal 2005] E. Lorentz and A. Benallal. Gradient constitutive relations: numerical aspects and application to gradient damage. *Computer methods in applied mechanics and engineering*, vol. 194, no. 50-52, pages 5191–5220, 2005. (Cited on page 19.)
- [Lorentz & Godard 2011] E. Lorentz and V. Godard. Gradient damage models: Toward full-scale computations. *Computer Methods in Applied Mechanics and Engineering*, vol. 200, no. 21, pages 1927–1944, 2011. (Cited on page 62.)
- [Lu *et al.* 2020] Y. Lu, T. Helfer, B. Bary and O. Fandeur. An efficient and robust staggered algorithm applied to the quasi-static description of brittle fracture by a phase-field approach. *Computer Methods in Applied Mechanics and Engineering*, vol. 370, page 113218, 2020. (Cited on page 20.)
- [Lund & Schuh 2003] A. C. Lund and C. A. Schuh. Yield surface of a simulated metallic glass. *Acta Materialia*, vol. 51, no. 18, pages 5399 – 5411, 2003. (Cited on page 40.)
- [Lund & Schuh 2004] A. C. Lund and C. A. Schuh. The Mohr-Coulomb criterion from unit shear processes in metallic glass. *Intermetallics*, vol. 12, no. 10–11, pages 1159 – 1165, 2004. (Cited on page 40.)
- [Lund & Schuh 2005] A. C. Lund and C. A. Schuh. Strength asymmetry in nanocrystalline metals under multiaxial loading. *Acta Materialia*, vol. 53, no. 11, pages 3193 – 3205, 2005. (Cited on page 40.)
- [Lund *et al.* 2004] A. C. Lund, T. G. Nieh and C. A. Schuh. Tension/compression strength asymmetry in a simulated nanocrystalline metal. *Physical Review B*, vol. 69, page 012101, 2004. (Cited on page 40.)
- [Luo *et al.* 2016] J. Luo, J. Wang, E. Bitzek, J.Y. Huang, H. Zheng, L. Tong, Q. Yang, J. Li and S.X. Mao. Size-Dependent Brittle-to-Ductile Transition in Silica Glass Nanofibers. *Nano Letters*, vol. 16, no. 1, pages 105–113, 2016. (Cited on pages 5 and 42.)
- [Luo *et al.* 2020] H. Luo, A. Gravouil, N. M. Giordano, W. Schirmacher and A. Tanguy. Continuum constitutive laws to describe acoustic attenuation in glasses. *Phys. Rev. E*, vol. 102, page 033003, 2020. (Cited on page 31.)
- [Mackenzie 1963] J. D. Mackenzie. High-Pressure Effects on Oxide Glasses: I. Densification in Rigid State. *Journal of the American Ceramic Society*, vol. 46, no. 10, pages 461–470, 1963. (Cited on page 36.)

- [Maekawa *et al.* 1991] H. Maekawa, T. Maekawa, K. Kawamura and T. Yokokawa. The structural groups of alkali silicate glasses determined from ^{29}Si MAS-NMR. *Journal of Non-Crystalline Solids*, vol. 127, no. 1, pages 53–64, 1991. (Cited on pages 37, 83 and 84.)
- [Maloney & Lemaître 2004] C. Maloney and A. Lemaître. Subextensive Scaling in the Athermal, Quasistatic Limit of Amorphous Matter in Plastic Shear Flow. *Physical Review Letters*, vol. 93, page 016001, 2004. (Cited on page 43.)
- [Mangasarian 1977] O. L. Mangasarian. Solution of symmetric linear complementarity problems by iterative methods. *Journal of Optimization Theory and Applications*, vol. 22, no. 4, pages 465–485, 1977. (Cited on page 20.)
- [Mantisi *et al.* 2012] B. Mantisi, A. Tanguy, G. Kermouche and E. Barthel. Atomistic response of a model silica glass under shear and pressure. *The European Physical Journal B*, vol. 85, no. 9, pages 1–14, 2012. (Cited on pages 37, 82 and 84.)
- [Mantič 2009] V. Mantič. Interface crack onset at a circular cylindrical inclusion under a remote transverse tension. Application of a coupled stress and energy criterion. *Int. J. Sol. Struct.*, vol. 46, pages 1287–1304, 2009. (Cited on page 7.)
- [Marengo *et al.* 2021] A. Marengo, A. Patton, M. Negri, U. Perego and A. Reali. A rigorous and efficient explicit algorithm for irreversibility enforcement in phase-field finite element modeling of brittle crack propagation. *Computer Methods in Applied Mechanics and Engineering*, vol. 387, page 114137, 2021. (Cited on page 20.)
- [Mariotte 1886] E. Mariotte. *Traité du mouvement des eaux et des autres corps fluides.* 1886. (Cited on page 4.)
- [Marsh & Cottrell 1964] D. M. Marsh and A. H. Cottrell. Plastic flow in glass. *Proceedings of the Royal Society of London. Series A. Mathematical and Physical Sciences*, vol. 279, no. 1378, pages 420–435, 1964. (Cited on pages 36 and 39.)
- [Martin *et al.* 2012] E. Martin, D. Leguillon and N. Carrère. A coupled strength and toughness criterion for the prediction of the open hole tensile strength of a composite plate. *Int. J. Sol. Struct.*, vol. 49(26), pages 3915–3922, 2012. (Cited on page 7.)
- [Martin *et al.* 2018] E. Martin, D. Leguillon, O. Seveček and R. Bermejo. Understanding the tensile strength of ceramics in the presence of small critical flaws. *Engng. Fract. Mech.*, vol. 201, pages 167–175, 2018. (Cited on pages 5, 7 and 16.)
- [Martinet *et al.* 2020] C. Martinet, M. Heili, V. Martinez, G. Kermouche, G. Molnar, N. Shechblanov, E. Barthel and A. Tanguy. Highlighting the impact of shear strain on the SiO_2 glass structure: From experiments to atomistic simulations. *Journal of Non-Crystalline Solids*, vol. 533, page 119898, 2020. (Cited on pages 40 and 100.)
- [McClintock & Irwin 1965] F. A. McClintock and G. R. Irwin. Plasticity aspects of fracture mechanics. In Committee E24, editor, *Fracture Toughness Testing and its Applications*, pages 84–113. ASTM International West Conshohocken, 1965. (Cited on pages 14 and 22.)
- [Miehe *et al.* 2010a] C. Miehe, F. Welschinger and M. Hofacker. Thermodynamically consistent phase-field models of fracture: Variational principles and multi-field FE implementations. *International Journal for Numerical Methods in Engineering*, vol. 83, no. 10, pages 1273–1311, 2010. (Cited on pages 8, 17 and 19.)

- [Miehe *et al.* 2010b] Christian Miehe, Martina Hofacker and Fabian Welschinger. A phase field model for rate-independent crack propagation: Robust algorithmic implementation based on operator splits. *Computer Methods in Applied Mechanics and Engineering*, vol. 199, no. 45–48, pages 2765 – 2778, 2010. (Cited on page 19.)
- [Mindlin 1963] R. D. Mindlin. Microstructure in linear elasticity. Technical report, Columbia Univ New York Dept of Civil Engineering and Engineering Mechanics, 1963. (Cited on page 54.)
- [Moës *et al.* 2011] N. Moës, C. Stolz, P.-E. Bernard and N. Chevaugeon. A level set based model for damage growth: The thick level set approach. *International Journal for Numerical Methods in Engineering*, vol. 86, no. 3, pages 358–380, 2011. (Cited on page 8.)
- [Molnár & Blal 2023] G. Molnár and N. Blal. Topology optimization of periodic beam lattices using Cosserat elasticity. *Computers & Structures*, vol. 281, page 107037, 2023. (Cited on pages iv, 59, 67, 68 and 99.)
- [Molnár & Bojtár 2012] G. Molnár and I. Bojtár. Solution of 1D Finite Element Problems With Explicit Time Integration. *Architectonics and Architecture*, vol. 40, no. 1, pages 5–32, 2012. (Cited on page 101.)
- [Molnár & Bojtár 2013] G. Molnár and I. Bojtár. Effects of manufacturing inhomogeneities on strength properties of float glass. *Mechanics of Materials*, vol. 59, pages 1–13, 2013. (Cited on page 101.)
- [Molnár & Doitrand 2025] G. Molnár and A. Doitrand. Understanding regularized crack initiation through the lens of Finite Fracture Mechanics. *International Journal of Fracture*, vol. 249, 2025. (Cited on page 99.)
- [Molnár & Gravouil 2017] G. Molnár and A. Gravouil. 2D and 3D Abaqus implementation of a robust staggered phase-field solution for modeling brittle fracture. *Finite Elements in Analysis and Design*, vol. 130, pages 27 – 38, 2017. (Cited on pages iii, 19, 20 and 100.)
- [Molnár & Réthoré 2024] G. Molnár and J. Réthoré. Fracture Toughness of Periodic Beam Lattices. *Journal of Theoretical, Computational and Applied Mechanics*, 2024. hal-04793587. (Cited on page 61.)
- [Molnár *et al.* 2012a] G. Molnár, L. M. Molnár and I. Bojtár. Multi-Scale Analysis of Structural Glass, Imaging of The Mesostructure. *Journal of Material Testers*, vol. 21, no. 3-4, pages 1–14, 2012. (Cited on page 101.)
- [Molnár *et al.* 2012b] G. Molnár, L. M. Molnár and I. Bojtár. Preparing a comprehensive analysis of the mechanical classification of structural glass. *Mater. Eng.: Materiálové inžinierstvo*, vol. 19, pages 71–81, 2012. (Cited on page 101.)
- [Molnár *et al.* 2012c] G. Molnár, L. G. Vigh and G. Stocker. Load bearing capacity of laminated glass. *Magyar Építőipar*, vol. 62, no. 1, pages 17–23, 2012. (Cited on page 101.)
- [Molnár *et al.* 2012d] G. Molnár, L. G. Vigh, G. Stocker and L. Dunai. Finite element analysis of laminated structural glass plates with polyvinyl butyral (PVB) interlayer. *Periodica Polytechnica Civil Engineering*, vol. 56, no. 1, pages 35–42, 2012. (Cited on page 101.)

- [Molnár *et al.* 2016a] G. Molnár, M. Ferentzi, Z. Weltsch, G. Szabényi, L. Borbás and I. Bojtár. Fragmentation of wedge loaded tempered structural glass. *Glass Structures & Engineering*, vol. 1, page 385–394, 2016. (Cited on pages 30 and 101.)
- [Molnár *et al.* 2016b] G. Molnár, P. Ganster, A. Tanguy, E. Barthel and G. Kermouche. Densification dependent yield criteria for sodium silicate glasses – An atomistic simulation approach. *Acta Materialia*, vol. 111, pages 129 – 137, 2016. (Cited on pages iii, 21, 45 and 101.)
- [Molnár *et al.* 2016c] G. Molnár, P. Ganster, A. Tanguy, J. Török and G. Kermouche. Transition from ductile to brittle failure of sodium silicate glasses: a numerical study. *MRS Advances*, vol. 1, no. 24, pages 1797–1802, 2016. (Cited on page 101.)
- [Molnár *et al.* 2016d] G. Molnár, P. Ganster, J. Török and A. Tanguy. Sodium effect on static mechanical behavior of MD-modeled sodium silicate glasses. *Journal of Non-Crystalline Solids*, vol. 440, pages 12 – 25, 2016. (Cited on pages iii, 36, 85 and 101.)
- [Molnár *et al.* 2017a] G. Molnár, P. Ganster and A. Tanguy. Effect of composition and pressure on the shear strength of sodium silicate glasses: An atomic scale simulation study. *Phys. Rev. E*, vol. 95, page 043001, 2017. (Cited on pages iii, iv, 43, 85 and 100.)
- [Molnár *et al.* 2017b] G. Molnár, G. Kermouche and E. Barthel. Plastic response of amorphous silicates, from atomistic simulations to experiments—A general constitutive relation. *Mechanics of Materials*, vol. 114, pages 1–8, 2017. (Cited on pages 41 and 100.)
- [Molnár *et al.* 2018] G. Molnár, D. Rodney, F. Martoia, P. J. .J. Dumont, Y. Nishiyama, K. Mazeau and L. Orgéas. Cellulose crystals plastify by localized shear. *Proceedings of the National Academy of Sciences*, vol. 115, no. 28, pages 7260–7265, 2018. (Cited on pages 85 and 100.)
- [Molnár *et al.* 2020a] G. Molnár, A. Doitrand, R. Estevez and A. Gravouil. Toughness or strength? Regularization in phase-field fracture explained by the coupled criterion. *Theoretical and Applied Fracture Mechanics*, vol. 109, page 102736, 2020. (Cited on pages iii, 21, 22, 61 and 100.)
- [Molnár *et al.* 2020b] G. Molnár, A. Gravouil, R. Seghir and J. Réthoré. An open-source Abaqus implementation of the phase-field method to study the effect of plasticity on the instantaneous fracture toughness in dynamic crack propagation. *Computer Methods in Applied Mechanics and Engineering*, vol. 365, page 113004, 2020. (Cited on pages iii, 19, 20, 30 and 100.)
- [Molnár *et al.* 2022] G. Molnár, A. Doitrand, A. Jaccon, B. Prabel and A. Gravouil. Thermodynamically consistent linear-gradient damage model in Abaqus. *Engineering Fracture Mechanics*, vol. 266, page 108390, 2022. (Cited on pages iii, 19, 20, 21, 24, 27, 30, 48 and 100.)
- [Molnár *et al.* 2024] G. Molnár, A. Doitrand and V. Lazarus. Phase-field simulation and coupled criterion link echelon cracks to internal length in antiplane shear. *Journal of the Mechanics and Physics of Solids*, vol. 188, page 105675, 2024. (Cited on pages iii, 16, 22, 61 and 99.)

- [Molnár *et al.* 2025] G. Molnár, A. Doitrand, R. Estevez and A. Gravouil. A review of characteristic lengths in the coupled criterion framework and advanced fracture models. *Comptes Rendus. Mécanique*, vol. 353, pages 91–111, 2025. (Cited on pages 1, 8 and 99.)
- [Molnár 2024] G. Molnár. Challenges in Phase-Field Modeling of Glass Fracture. In *Challenging Glass Conference Proceedings*, volume 9, 2024. (Cited on pages 30 and 101.)
- [Mott *et al.* 1993] P. H. Mott, A. S. Argon and U. W. Suter. Atomistic modelling of plastic deformation of glassy polymers. *Philosophical Magazine A*, vol. 67, no. 4, pages 931–978, 1993. (Cited on page 40.)
- [Mousanezhad *et al.* 2015] D. Mousanezhad, S. Babaei, H. Ebrahimi, R. Ghosh, A. S. Hamouda, K. Bertoldi and A. Vaziri. Hierarchical honeycomb auxetic metamaterials. *Scientific reports*, vol. 5, no. 1, pages 1–8, 2015. (Cited on page 54.)
- [Mumford & Shah 1989] David Mumford and Jayant Shah. Optimal approximations by piecewise smooth functions and associated variational problems. *Communications on pure and applied mathematics*, vol. 42, no. 5, pages 577–685, 1989. (Cited on pages 8 and 16.)
- [Naji *et al.* 2015] M. Naji, D. De Sousa-Meneses, G. Guimbretière and Y. P. Vaills. In situ High Temperature Probing of the Local Order of a Silicate Glass and Melt during Structural Relaxation. *The Journal of Physical Chemistry C*, 2015. accepted. (Cited on page 37.)
- [Needleman 1987] A. Needleman. Continuum model for void nucleation by decohesion debonding. *J. Appl. Mech.*, vol. 54, pages 525–531, 1987. (Cited on page 8.)
- [Needleman 1990] A. Needleman. An analysis of tensile decohesion along an interface. *J. Mech. Phys. Sol.*, vol. 38, pages 289–324, 1990. (Cited on page 8.)
- [Neimitz & Aifantis 1987] A. Neimitz and E. C. Aifantis. On the size and shape of the process zone. *Engineering fracture mechanics*, vol. 26, no. 4, pages 491–503, 1987. (Cited on page 6.)
- [Nepal *et al.* 2023] Dhriti Nepal, Saewon Kang, Katarina M Adstedt, Krishan Kanhaiya, Michael R Bockstaller, L Catherine Brinson, Markus J Buehler, Peter V Coveney, Kaushik Dayal, Jaafar A El-Awady *et al.* Hierarchically structured bioinspired nanocomposites. *Nature materials*, vol. 22, no. 1, pages 18–35, 2023. (Cited on page 54.)
- [Nguyen *et al.* 2016a] T.-T. Nguyen, J. Yvonnet, M. Bornert and C. Chateau. Initiation and propagation of complex 3D networks of cracks in heterogeneous quasi-brittle materials: Direct comparison between in situ testing-microCT experiments and phase field simulations. *Journal of the Mechanics and Physics of Solids*, vol. 95, pages 320–350, 2016. (Cited on page 14.)
- [Nguyen *et al.* 2016b] T.-T. Nguyen, J. Yvonnet, Q.-Z. Zhu, M. Bornert and C. Chateau. A phase-field method for computational modeling of interfacial damage interacting with crack propagation in realistic microstructures obtained by microtomography. *Computer Methods in Applied Mechanics and Engineering*, vol. 312, pages 567–595, 2016. (Cited on page 14.)

- [Nguyen *et al.* 2016c] T.-T. Nguyen, Y. Yvonnet, M. Bornert, C. Chateau, K. Sab, R. Romani and R. Le Roy. On the choice of parameters in the phase field method for simulating crack initiation with experimental validation. *International Journal of Fracture*, vol. 197, no. 2, pages 213–226, 2016. (Cited on page 14.)
- [Nguyen *et al.* 2017] T. T. Nguyen, J. Réthoré and M.-C. Baietto. Phase field modelling of anisotropic crack propagation. *European Journal of Mechanics-A/Solids*, vol. 65, pages 279–288, 2017. (Cited on page 61.)
- [Nicolas *et al.* 2015] A. Nicolas, F. Puosi, H. Mizuno and J.-L. Barrat. Elastic consequences of a single plastic event: Towards a realistic account of structural disorder and shear wave propagation in models of flowing amorphous solids. *Journal of the Mechanics and Physics of Solids*, vol. 78, pages 333 – 351, 2015. (Cited on page 43.)
- [Orowan 1949] E. Orowan. Fracture and strength of solids. *Reports on Progress in Physics*, vol. 12, pages 185–232, 1949. (Cited on page 6.)
- [Ortiz & Pandolfi 1999] M. Ortiz and A. Pandolfi. Finite-deformation irreversible cohesive elements for three-dimensional crack-propagation analysis. *International journal for numerical methods in engineering*, vol. 44, no. 9, pages 1267–1282, 1999. (Cited on page 8.)
- [Otsuka & Date 2000] K. Otsuka and H. Date. Fracture process zone in concrete tension specimen. *Engineering fracture mechanics*, vol. 65, no. 2-3, pages 111–131, 2000. (Cited on page 6.)
- [Palaniswamy & Knauss 1978] K. Palaniswamy and W.G. Knauss. II - On the Problem of Crack Extension in Brittle Solids Under General Loading. In *Mechanics Today*, pages 87–148. 1978. (Cited on page 26.)
- [Park & Lakes 1986] H. C. Park and R. S. Lakes. Cosserat micromechanics of human bone: strain redistribution by a hydration sensitive constituent. *Journal of biomechanics*, vol. 19, no. 5, pages 385–397, 1986. (Cited on page 54.)
- [Parrinello & Rahman 1982] M Parrinello and A Rahman. Strain fluctuations and elastic constants. *The Journal of Chemical Physics*, vol. 76, no. 5, pages 2662–2666, 1982. (Cited on page 37.)
- [Patinet *et al.* 2016] S. Patinet, D. Vandembroucq and M. L. Falk. Connecting local yield stresses with plastic activity in amorphous solids. *Physical review letters*, vol. 117, no. 4, page 045501, 2016. (Cited on page 45.)
- [Pedone *et al.* 2006] A. Pedone, G. Malavasi, M. C. Menziani, A. N. Cormack and U. Segre. A New Self-Consistent Empirical Interatomic Potential Model for Oxides, Silicates, and Silica-Based Glasses. *The Journal of Physical Chemistry B*, vol. 110, no. 24, pages 11780–11795, 2006. (Cited on pages 36 and 82.)
- [Pedone *et al.* 2007] A. Pedone, G. Malavasi, A. N. Cormack, U. Segre and M. C. Menziani. Insight into Elastic Properties of Binary Alkali Silicate Glasses; Prediction and Interpretation through Atomistic Simulation Techniques. *Chemistry of Materials*, vol. 19, pages 3144–3154, 2007. (Cited on pages 36 and 82.)
- [Peerlings *et al.* 1996] R. H. J. Peerlings, R. de Borst, W. A. M. Brekelmans and J. H. P. de Vree. Gradient enhanced damage for quasi-brittle materials. *International Journal for numerical methods in engineering*, vol. 39, no. 19, pages 3391–3403, 1996. (Cited on page 8.)

- [Peerlings *et al.* 1998] R. H. J. Peerlings, R. de Borst, W. A. M. Brekelmans and M. G. D. Geers. Gradient-enhanced damage modelling of concrete fracture. *Mechanics of Cohesive-frictional Materials: An International Journal on Experiments, Modelling and Computation of Materials and Structures*, vol. 3, no. 4, pages 323–342, 1998. (Cited on page 8.)
- [Peirce 1926] F. T. Peirce. Theorems on the Strength of Long and of Composite Specimens. *Journal of the Textile Institute Transactions*, vol. 17, no. 7, pages T355–T368, 1926. (Cited on page 5.)
- [Pham & Marigo 2010a] K. Pham and J.-J. Marigo. Approche variationnelle de l'endommagement : I. Les concepts fondamentaux. *Comptes Rendus Mécanique*, vol. 338, no. 4, pages 191 – 198, 2010. (Cited on page 14.)
- [Pham & Marigo 2010b] K. Pham and J.-J. Marigo. Approche variationnelle de l'endommagement : II. Les modèles à gradient. *Comptes Rendus Mécanique*, vol. 338, no. 4, pages 199 – 206, 2010. (Cited on page 14.)
- [Pham & Ravi-Chandar 2014] K. H. Pham and K. Ravi-Chandar. Further examination of the criterion for crack initiation under mixed-mode I+III loading. *International Journal of Fracture*, vol. 189, no. 2, pages 121–138, 2014. (Cited on page 26.)
- [Pham & Ravi-Chandar 2016] K. H. Pham and K. Ravi-Chandar. On the growth of cracks under mixed-mode I+III loading. *International Journal of Fracture*, vol. 199, no. 1, pages 105–134, 2016. (Cited on page 27.)
- [Pham & Ravi-Chandar 2017] K. H. Pham and K. Ravi-Chandar. The formation and growth of echelon cracks in brittle materials. *International Journal of Fracture*, vol. 206, no. 2, pages 229–244, 2017. (Cited on page 28.)
- [Pham *et al.* 2011] K. Pham, H. Amor, J.-J. Marigo and C. Maurini. Gradient damage models and their use to approximate brittle fracture. *International Journal of Damage Mechanics*, vol. 20, no. 4, pages 618–652, 2011. (Cited on pages 14 and 17.)
- [Pichler & Hellmich 2011] Bernhard Pichler and Christian Hellmich. Upscaling quasi-brittle strength of cement paste and mortar: A multi-scale engineering mechanics model. *Cement and Concrete Research*, vol. 41, no. 5, pages 467–476, 2011. (Cited on page 58.)
- [Piero 2013] G. Del Piero. A variational approach to fracture and other inelastic phenomena. *Journal of Elasticity*, vol. 112, no. 1, pages 3–77, 2013. (Cited on page 14.)
- [Pijaudier-Cabot & Bažant 1987] G. Pijaudier-Cabot and Z. P. Bažant. Nonlocal damage theory. *Journal of engineering mechanics*, vol. 113, no. 10, pages 1512–1533, 1987. (Cited on page 8.)
- [Plimpton 1995] S. Plimpton. Fast Parallel Algorithms for Short-Range Molecular Dynamics. *Journal of Computational Physics*, vol. 117, pages 1–19, 1995. (Cited on page 36.)
- [Pollard *et al.* 1982] D. D. Pollard, P. Segall and P. T. Delaney. Formation and interpretation of dilatant echelon cracks. *Geological Society of America Bulletin*, vol. 93, no. 12, pages 1291–1303, 1982. (Cited on page 26.)

- [Pradel & Sab 1998] F. Pradel and K. Sab. Cosserat modelling of elastic periodic lattice structures. *Comptes Rendus de l'Académie des Sciences-Series IIB-Mechanics-Physics-Astronomy*, vol. 326, no. 11, pages 699–704, 1998. (Cited on pages 56, 58 and 61.)
- [Prescher *et al.* 2017] C. Prescher, V. B. Prakapenka, J. Stefanski, S. Jahn, L. B. Skinner and Y. Wang. Beyond sixfold coordinated Si in SiO₂ glass at ultrahigh pressures. *Proceedings of the National Academy of Sciences*, vol. 114, no. 38, pages 10041–10046, 2017. (Cited on page 38.)
- [Puosi *et al.* 2014] F. Puosi, J. Rottler and J-L. Barrat. Time-dependent elastic response to a local shear transformation in amorphous solids. *Phys. Rev. E*, vol. 89, page 042302, 2014. (Cited on page 43.)
- [Quintana-Alonso *et al.* 2010] Ignacio Quintana-Alonso, SP Mai, NA Fleck, DCH Oakes and MV Twigg. The fracture toughness of a cordierite square lattice. *Acta materialia*, vol. 58, no. 1, pages 201–207, 2010. (Cited on page 63.)
- [Raabe *et al.* 2004] Dierk Raabe, Franz Roters, Frédéric Barlat and Long-Qing Chen. *Continuum scale simulation of engineering materials: fundamentals-microstructures-process applications*. John Wiley & Sons, 2004. (Cited on page 32.)
- [Rankine 1857] W. J. M. Rankine. II. On the stability of loose earth. *Philosophical transactions of the Royal Society of London*, no. 147, pages 9–27, 1857. (Cited on page 21.)
- [Reis & Ganghoffer 2012] F. Dos Reis and J. F. Ganghoffer. Construction of micropolar continua from the asymptotic homogenization of beam lattices. *Computers & Structures*, vol. 112, pages 354–363, 2012. (Cited on page 56.)
- [Remmers *et al.* 2003] J. J. C. Remmers, R. de Borst and A. Needleman. A cohesive segments method for the simulation of crack growth. *Comp. Mech.*, vol. 31, pages 69–77, 2003. (Cited on page 8.)
- [Réthoré & Estevez 2013] J. Réthoré and R. Estevez. Identification of a cohesive zone model from digital images at the micron-scale. *Journal of the Mechanics and Physics of Solids*, vol. 61, no. 6, pages 1407–1420, 2013. (Cited on pages 6 and 9.)
- [Richard *et al.* 2014] H. A. Richard, B. Schramm and N.-H. Schirmeisen. Cracks on mixed mode loading—theories, experiments, simulations. *International Journal of Fatigue*, vol. 62, pages 93–103, 2014. (Cited on pages 22 and 25.)
- [Rimsza *et al.* 2017] J. M. Rimsza, R. E. Jones and L. J. Criscenti. Surface structure and stability of partially hydroxylated silica surfaces. *Langmuir*, vol. 33, no. 15, pages 3882–3891, 2017. (Cited on pages 47 and 50.)
- [Rimsza *et al.* 2018] J. M. Rimsza, R. E. Jones and L. J. Criscenti. Crack propagation in silica from reactive classical molecular dynamics simulations. *Journal of the American Ceramic Society*, vol. 101, no. 4, pages 1488–1499, 2018. (Cited on pages 47 and 50.)
- [Ritchie *et al.* 2009] R. O. Ritchie, M. J. Buehler and P. Hansma. Plasticity and toughness in bone. *Physics today*, vol. 62, no. 6, pages 41–47, 2009. (Cited on page 54.)
- [Ritchie 2011] R. O. Ritchie. The conflicts between strength and toughness. *Nature Materials*, vol. 10, no. 11, pages 817–822, 2011. (Cited on page 54.)

- [Rodney *et al.* 2011] D. Rodney, A. Tanguy and D. Vandembroucq. Modeling the mechanics of amorphous solids at different length scale and time scale. *Modelling and Simulation in Materials Science and Engineering*, vol. 19, no. 8, page 083001, 2011. (Cited on page 41.)
- [Rodney *et al.* 2024] D. Rodney, P.-A. Geslin, S. Patinet, V. Démary and A. Rosso. Does the Larkin length exist? *Modelling and Simulation in Materials Science and Engineering*, vol. 32, no. 3, page 035007, 2024. (Cited on page 44.)
- [Romeis *et al.* 2015] S. Romeis, J. Paul, P. Herre, D. de Ligny, J. Schmidt and W. Peukert. Local densification of a single micron sized silica sphere by uniaxial compression. *Scripta Materialia*, vol. 108, pages 84 – 87, 2015. (Cited on page 39.)
- [Ronsin *et al.* 2014] O. Ronsin, C. Caroli and T. Baumberger. Crack front échelon instability in mixed mode fracture of a strongly nonlinear elastic solid. *Europhysics Letters*, vol. 105, no. 3, page 34001, 2014. (Cited on page 26.)
- [Rorato *et al.* 2023] L. Rorato, Y. Shang, S. Yang, M. Hubert, K. Couturier, L. Zhang, J. Vulliet, M. Chen and J. Laurencin. Understanding the Ni Migration in Solid Oxide Cell: A Coupled Experimental and Modeling Approach. *Journal of The Electrochemical Society*, vol. 170, no. 3, page 034504, 2023. (Cited on page 33.)
- [Rosendahl *et al.* 2019] P. L. Rosendahl, Y. Staudt, A. P. Schneider, J. Schneider and W. Becker. Nonlinear elastic finite fracture mechanics: modeling mixed-mode crack nucleation in structural glazing silicone sealants. *Materials and Design*, vol. 182, page 108057, 2019. (Cited on page 7.)
- [Rottler & Robbins 2001] J. Rottler and M. O. Robbins. Yield conditions for deformation of amorphous polymer glasses. *Physical Review E*, vol. 642, page 051801, 2001. (Cited on page 40.)
- [Rountree *et al.* 2007] C. L. Rountree, S. Prades, D. Bonamy, E. Bouchaud, R. Kalia and C. Guillot. A unified study of crack propagation in amorphous silica: Using experiments and simulations. *Journal of alloys and compounds*, vol. 434, pages 60–63, 2007. (Cited on page 47.)
- [Rountree *et al.* 2010] C. L. Rountree, D. Bonamy, D. Dalmas, S. Prades, R. K. Kalia, C. Guillot and E. Bouchaud. Fracture in glass via molecular dynamics simulations and atomic force microscopy experiments. *Physics and Chemistry of Glasses-European Journal of Glass Science and Technology Part B*, vol. 51, no. 2, pages 127–132, 2010. (Cited on pages 6 and 7.)
- [Roux & Hild 2008] Stéphane Roux and François Hild. Self-consistent scheme for toughness homogenization. *International journal of fracture*, vol. 154, no. 1, pages 159–166, 2008. (Cited on page 59.)
- [Roux *et al.* 2009] S. Roux, J. Réthoré and F. Hild. Digital image correlation and fracture: an advanced technique for estimating stress intensity factors of 2D and 3D cracks. *Journal of Physics D: Applied Physics*, vol. 42, no. 21, page 214004, 2009. (Cited on page 50.)
- [Rouxel *et al.* 2010] T. Rouxel, H. Ji, J. P. Guin, F. Augereau and B. Rufflé. Indentation deformation mechanism in glass: Densification versus shear flow. *Journal of Applied Physics*, vol. 107, no. 9, page 094903, 2010. (Cited on page 37.)

- [Rouxel 2015] T. Rouxel. Driving force for indentation cracking in glass: composition, pressure and temperature dependence. *Philosophical Transactions of the Royal Society of London A: Mathematical, Physical and Engineering Sciences*, vol. 373, 2015. (Cited on page 36.)
- [Rueger & Lakes 2016] Z. Rueger and R. S. Lakes. Experimental Cosserat elasticity in open-cell polymer foam. *Philosophical Magazine*, vol. 96, no. 2, pages 93–111, 2016. (Cited on page 55.)
- [Sab & Pradel 2009] K. Sab and F. Pradel. Homogenisation of periodic Cosserat media. *International journal of computer applications in technology*, vol. 34, no. 1, page 60, 2009. (Cited on pages 56, 58 and 61.)
- [Saidi *et al.* 2023] A. Saidi, A. Tanguy, M. Fourmeau, G. Molnár, A. Boucherif and D. Machon. Coupling between mechanical stresses and lithium penetration in a lithium ion battery. *Mechanics of Materials*, vol. 177, page 104532, 2023. (Cited on pages iv, 74 and 100.)
- [Sapora *et al.* 2018] A. Sapora, A. R. Torabi, S. Etesam and P. Cornetti. Finite Fracture Mechanics crack initiation from a circular hole. *Fatigue & Fracture of Engineering Materials & Structures*, vol. 41, no. 7, pages 1627–1636, 2018. (Cited on page 5.)
- [Sargado *et al.* 2018] J. M. Sargado, E. Keilegavlen, I. Berre and J. M. Nordbotten. High-accuracy phase-field models for brittle fracture based on a new family of degradation functions. *Journal of the Mechanics and Physics of Solids*, vol. 111, pages 458–489, 2018. (Cited on page 24.)
- [Schaedler *et al.* 2011] T. A. Schaedler, A. J. Jacobsen, A. Torrents, A. E. Sorensen, J. Lian, J. R. Greer, L. Valdevit and W. B. Carter. Ultralight Metallic Microlattices. *Science*, vol. 334, no. 6058, pages 962–965, 2011. (Cited on page 6.)
- [Scherer *et al.* 2022] J.-M. Scherer, S. Brach and J. Bleyer. An assessment of anisotropic phase-field models of brittle fracture. *Computer Methods in Applied Mechanics and Engineering*, vol. 395, page 115036, 2022. (Cited on page 61.)
- [Schuh & Lund 2003] C. A. Schuh and A. C. Lund. Atomistic basis for the plastic yield criterion of metallic glass. *Nature Materials*, vol. 2, pages 449 – 452, 2003. (Cited on pages 9, 40 and 42.)
- [Seghir & Pierron 2018] Rian Seghir and Fabrice Pierron. A novel image-based ultrasonic test to map material mechanical properties at high strain-rates. *Experimental Mechanics*, vol. 58, pages 183–206, 2018. (Cited on page 31.)
- [Sepulveda-Macias *et al.* 2024] M. Sepulveda-Macias, G. Molnár and A. Tanguy. Thermomechanical dissipative behaviour of CuZr metallic glasses. *Journal of Non-Crystalline Solids*, vol. 636, page 123028, 2024. (Cited on page 99.)
- [Sethian 1996] James A Sethian. Level set methods, Evolving interfaces in geometry, fluid mechanics computer vision, and materials sciences. *Cambridge Monographs on Applied and Computational Mathematics*, 3, 1996. (Cited on page 66.)
- [Shah & Swartz 1987] S. P. Shah and S. E. Swartz. Fracture of concrete and rock. In *SEM-RILEM International Conference*, 1987. (Cited on page 5.)

- [Shimizu *et al.* 2006] F. Shimizu, S. Ogata and J. Li. Yield point of metallic glass. *Acta Materialia*, vol. 54, no. 16, pages 4293 – 4298, 2006. (Cited on page 40.)
- [Sigmund 1997] O. Sigmund. On the design of compliant mechanisms using topology optimization. *Journal of Structural Mechanics*, vol. 25, no. 4, pages 493–524, 1997. (Cited on page 67.)
- [Sigmund 2001] O. Sigmund. A 99 line topology optimization code written in Matlab. *Structural and multidisciplinary optimization*, vol. 21, no. 2, pages 120–127, 2001. (Cited on page 67.)
- [Sih 1974] G. C. Sih. Strain-energy-density factor applied to mixed mode crack problems. *International Journal of fracture*, vol. 10, no. 3, pages 305–321, 1974. (Cited on page 25.)
- [Silva *et al.* 2016] P. E. S. Silva, J. L. Trigueiros, A. C. Trindade, R. Simoes, R. G. Dias, M. H. Godinho and F. V. De Abreu. Perversions with a twist. *Scientific reports*, vol. 6, no. 1, page 23413, 2016. (Cited on page 90.)
- [Sommer 1969] E. Sommer. Formation of fracture ‘lances’ in glass. *Engineering Fracture Mechanics*, vol. 1, no. 3, pages 539–546, 1969. (Cited on page 26.)
- [Spaepen 1977] F. Spaepen. A microscopic mechanism for steady state inhomogeneous flow in metallic glasses. *Acta Metallurgica*, vol. 25, no. 4, pages 407 – 415, 1977. (Cited on pages 37 and 42.)
- [Stein *et al.* 2015] N. Stein, P. Weißgraeber and W. Becker. A model for brittle failure in adhesive lap joints of arbitrary joint configuration. *Composite Structures*, vol. 133, pages 707–718, 2015. (Cited on page 7.)
- [Sun & Jin 2012] C.-T. Sun and Z.-H. Jin. The elastic stress field around a crack tip. *Fracture Mechanics*, pages 25–75, 2012. (Cited on pages 22 and 25.)
- [Tanguy *et al.* 2002] A. Tanguy, J.P.Wittmer, F. Leonforte and J.-L. Barrat. Continuum limit of amorphous elastic bodies: a finite-size study of low-frequency harmonic vibrations. *Physical Review B*, vol. 66, page 174205, 2002. (Cited on page 43.)
- [Tanguy *et al.* 2006] A. Tanguy, F. Léonforte and J. L. Barrat. Plastic response of a 2D Lennard-Jones amorphous solid: detailed analyses of the local rearrangements at very slow strain rate. *The European Physics Journal E*, vol. 20, pages 355–364, 2006. (Cited on pages 37 and 43.)
- [Tanné *et al.* 2018] E. Tanné, T. Li, B. Bourdin, J.-J. Marigo and C. Maurini. Crack nucleation in variational phase-field models of brittle fracture. *Journal of the Mechanics and Physics of Solids*, vol. 110, pages 80–99, 2018. (Cited on pages 14 and 24.)
- [Taylor 1949] E. W. Taylor. Plastic deformation of optical glass. *Nature*, vol. 163, no. 4139, pages 323–323, 1949. (Cited on page 39.)
- [Taylor 2008] D. Taylor. The theory of critical distances. *Engineering Fracture Mechanics*, vol. 75, no. 7, pages 1696–1705, 2008. (Cited on page 6.)

- [Thompson *et al.* 2009] A. P. Thompson, S. J. Plimpton and W. Mattson. General formulation of pressure and stress tensor for arbitrary many-body interaction potentials under periodic boundary conditions. *The Journal of chemical physics*, vol. 131, no. 15, 2009. (Cited on page 37.)
- [Tippett 1925] L. C. H. Tippett. On the extreme individuals and the range of samples taken from a normal population. *Biometrika*, pages 364–387, 1925. (Cited on page 5.)
- [Toupin 1962] R. Toupin. Elastic materials with couple-stresses. *Archive for rational mechanics and analysis*, vol. 11, no. 1, pages 385–414, 1962. (Cited on page 54.)
- [Tsamados *et al.* 2009] M. Tsamados, A. Tanguy and C. Goldenberg and J. L. Barrat. Local elasticity map and plasticity in a model Lennard-Jones glass. *Physical Review E*, vol. 80, page 026112, 2009. (Cited on page 43.)
- [Tsuneyuki *et al.* 1989] S. Tsuneyuki, Y. Matsui, H. Aoki and M. Tsukada. New pressure-induced structural transformations in silica obtained by computer simulation. *Nature*, vol. 339, pages 209–211, 1989. (Cited on pages 36 and 82.)
- [Usami *et al.* 1986] S. Usami, H. Kimoto, I. Takahashi and S. Shida. Strength of ceramic materials containing small flaws. *Engineering Fracture Mechanics*, vol. 23, no. 4, pages 745–761, 1986. (Cited on page 5.)
- [van Beest *et al.* 1990] B. W. H. van Beest, G. J. Kramer and R. A. van Santen. Force fields for silicas and aluminophosphates based on ab initio calculations. *Physical Review Letters*, vol. 64, pages 1955–1958, 1990. (Cited on pages 36 and 82.)
- [van Swygenhoven *et al.* 1999] H. van Swygenhoven, M. Spaczer, A. Caro and D. Farkas. Competing plastic deformation mechanisms in nanophase metals. *Physical Review B*, vol. 60, pages 22–25, 1999. (Cited on page 40.)
- [Vandembroucq *et al.* 2008] D. Vandembroucq, T. Deschamps, C. Coussa, A. Perriot, E. Barthel, B. Champagnon and C. Martinet. Density hardening plasticity and mechanical ageing of silica glass under pressure: a Raman spectroscopic study. *Journal of Physics: Condensed Matter*, vol. 20, no. 48, page 485221, 2008. (Cited on page 36.)
- [Vasoya *et al.* 2016] Manish Vasoya, Véronique Lazarus and Laurent Ponson. Bridging micro to macroscale fracture properties in highly heterogeneous brittle solids: weak pinning versus fingering. *Journal of the Mechanics and Physics of Solids*, vol. 95, pages 755–773, 2016. (Cited on page 59.)
- [Vermilye & Scholz 1998] J. M. Vermilye and C. H. Scholz. The process zone: A microstructural view of fault growth. *Journal of Geophysical Research: Solid Earth*, vol. 103, no. B6, pages 12223–12237, 1998. (Cited on page 6.)
- [Vollmayr *et al.* 1996] K. Vollmayr, W. Kob and K. Binder. Cooling-rate effects in amorphous silica: A computer-simulation study. *Physical Review B*, vol. 54, no. 22, pages 15808–15827, 1996. (Cited on page 82.)
- [Wang & Tai 2005] S. Y. Wang and K. Tai. Structural topology design optimization using genetic algorithms with a bit-array representation. *Computer methods in applied mechanics and engineering*, vol. 194, no. 36–38, pages 3749–3770, 2005. (Cited on page 74.)

- [Wang *et al.* 1993] S.-L. Wang, R. F. Sekerka, A. A. Wheeler, B. T. Murray, S. R. Coriell, R. J. Braun and G. B. McFadden. Thermodynamically-consistent phase-field models for solidification. *Physica D: Nonlinear Phenomena*, vol. 69, no. 1-2, pages 189–200, 1993. (Cited on page 32.)
- [Watts *et al.* 2019] Seth Watts, William Arrighi, Jun Kudo, Daniel A. Tortorelli and Daniel A. White. Simple, accurate surrogate models of the elastic response of three-dimensional open truss micro-architectures with applications to multiscale topology design. *Struct Multidisc Optim*, vol. 60, no. 4, pages 1887–1920, 2019. (Cited on pages 10 and 67.)
- [Weaire & Kermode 1984] D. Weaire and J.P. Kermode. Computer simulation of a two-dimensional soap froth II. Analysis of the results. *Philosophical Magazine B: Physics of Condensed Matter*, vol. 50, pages 379–395, 1984. (Cited on page 43.)
- [Weibull 1939a] W. Weibull. The phenomenon of rupture in solids. *IVA Handlingar*, vol. 153, 1939. (Cited on page 5.)
- [Weibull 1939b] W. Weibull. Statistical theory of the Strength of materials. *Proc. Royal Academy Engrg Science*, vol. 15, no. 1, page 1, 1939. (Cited on page 5.)
- [Weißgraeber *et al.* 2016] P. Weißgraeber, D. Leguillon and W. Becker. A review of Finite Fracture Mechanics: crack initiation at singular and non-singular stress raisers. *Archive Appl. Mech.*, vol. 86(1-2), page 375–401, 2016. (Cited on page 7.)
- [Westergaard 1939] H. M. Westergaard. Bearing pressures and cracks: Bearing pressures through a slightly waved surface or through a nearly flat part of a cylinder, and related problems of cracks. 1939. (Cited on page 27.)
- [Wheeler *et al.* 2014] M. F. Wheeler, T. Wick and W. Wollner. An augmented-Lagrangian method for the phase-field approach for pressurized fractures. *Computer Methods in Applied Mechanics and Engineering*, vol. 271, pages 69–85, 2014. (Cited on page 20.)
- [Wick 2017] T. Wick. Modified Newton methods for solving fully monolithic phase-field quasi-static brittle fracture propagation. *Computer Methods in Applied Mechanics and Engineering*, vol. 325, pages 577–611, 2017. (Cited on page 19.)
- [Williams 1957] E. Williams. Some observations of Leonardo, Galileo, Mariotte and others relative to size effect. *Annals of Science*, vol. 13, no. 1, pages 23–29, 1957. (Cited on page 4.)
- [Wolf *et al.* 1999] D. Wolf, P. Keblinski, S. R. Phillpot and J. Eggebrecht. Exact method for the simulation of Coulombic systems by spherically truncated, pairwise r^{-1} summation. *The Journal of chemical physics*, vol. 110, no. 17, pages 8254–8282, 1999. (Cited on page 36.)
- [Wu & Huang 2020] J.-Y. Wu and Y. Huang. Comprehensive implementations of phase-field damage models in Abaqus. *Theoretical and Applied Fracture Mechanics*, vol. 106, page 102440, 2020. (Cited on pages 19 and 27.)
- [Wu 1978] C.-H. Wu. Fracture Under Combined Loads by Maximum-Energy-Release-Rate Criterion. *Journal of Applied Mechanics*, vol. 45, no. 3, pages 553–558, 1978. (Cited on page 25.)

- [Wu 2018] J.-Y. Wu. Robust numerical implementation of non-standard phase-field damage models for failure in solids. *Computer Methods in Applied Mechanics and Engineering*, vol. 340, pages 767 – 797, 2018. (Cited on page 17.)
- [Xu & Leguillon. 2019] R. Xu and D. Leguillon. Dual-Notch Void Model to Explain the Anisotropic Strengths of 3D Printed Polymers. *J of Engng Mat. Tech.*, vol. 142(1), pages 1–4, 2019. (Cited on page 7.)
- [Xu *et al.* 2014] Y. Xu, J. Chen and H. Li. Finite hyperelastic–plastic constitutive equations for atomistic simulation of dynamic ductile fracture. *International Journal of Plasticity*, vol. 59, pages 15 – 29, 2014. (Cited on page 41.)
- [Yosibash & Mittelman 2016] Z. Yosibash and B. Mittelman. A 3-D failure initiation criterion from a sharp V-notch edge in elastic brittle structures. *Eur. J. Mech. A/Sol.*, vol. 60, pages 70–94, 2016. (Cited on page 7.)
- [Younes & Engelder 1999] A. I. Younes and T. Engelder. Fringe cracks: key structures for the interpretation of the progressive Alleghanian deformation of the Appalachian plateau. *Geological Society of America Bulletin*, vol. 111, no. 2, pages 219–239, 1999. (Cited on page 26.)
- [Yu & Kobayashi 1994] C.-T. Yu and A.-S. Kobayashi. Fracture process zone associated with mixed mode fracture of SiCw/Al₂O₃. *Journal of non-crystalline solids*, vol. 177, pages 26–35, 1994. (Cited on page 6.)
- [Yu *et al.* 2019] Y. Yu, W. Zeng, W. Liu, H. Zhang and X. Wang. Crack Propagation and Fracture Process Zone (FPZ) of Wood in the Longitudinal Direction Determined Using Digital Image Correlation (DIC) Technique. *Remote Sensing*, vol. 11, no. 13, page 1562, 2019. (Cited on page 6.)
- [Yuan & Cormack 2001] X. Yuan and A. N. Cormack. Local structures of MD-modeled vitreous silica and sodium silicate glasses. *Journal of Non-Crystalline Solids*, vol. 283, no. 1–3, pages 69–87, 2001. (Cited on pages 36, 82 and 83.)
- [Zang *et al.* 2000] A. Zang, F. C. Wagner, S. Stanchits, C. Janssen and G. Dresen. Fracture process zone in granite. *Journal of Geophysical Research: Solid Earth*, vol. 105, no. B10, pages 23651–23661, 2000. (Cited on page 6.)
- [Zhang & Qiao 2018] H. Zhang and P. Qiao. A coupled peridynamic strength and fracture criterion for openhole failure analysis of plates under tensile load. *Engng. Fract. Mech.*, vol. 204, pages 103–118, 2018. (Cited on page 7.)
- [Zhang *et al.* 2008] H. W. Zhang, H. Wang, B. S. Chen and Z. Q. Xie. Analysis of Cosserat materials with Voronoi cell finite element method and parametric variational principle. *Computer methods in applied mechanics and engineering*, vol. 197, no. 6-8, pages 741–755, 2008. (Cited on page 55.)
- [Zhang *et al.* 2017] X. Zhang, C. Vignes, S. W. Sloan and D. Sheng. Numerical evaluation of the phase-field model for brittle fracture with emphasis on the length scale. *Computational Mechanics*, vol. 59, no. 5, pages 737–752, 2017. (Cited on page 14.)
- [Zheng *et al.* 2016] X. Zheng, W. Smith, J. Jackson, B. Moran, H. Cui, D. Chen, J. Ye, N. Fang, N. Rodriguez, T. Weisgraber and C. M. Spadaccini. Multiscale metallic metamaterials. *Nature materials*, vol. 15, no. 10, pages 1100–1106, 2016. (Cited on page 54.)

-
- [Zietlow & Labuz 1998] W. K. Zietlow and J. F. Labuz. Measurement of the intrinsic process zone in rock using acoustic emission. *International Journal of Rock Mechanics and Mining Sciences*, vol. 35, no. 3, pages 291–299, 1998. (Cited on page 6.)
- [Zotov & Keppler 1998] N. Zotov and H. Keppler. The structure of sodium tetrasilicate glass from neutron diffraction, reverse Monte Carlo simulations and Raman spectroscopy. *Physics and Chemistry of Minerals*, vol. 25, no. 4, pages 259–267, 1998. (Cited on page 37.)

The role of length scales in material failure

Abstract: Most materials exhibit markedly different behaviors at the micro-scale compared to the macro-scale, particularly when it comes to failure. At very small scales, solids tend to be significantly stronger than at the structural level. This difference is typically attributed to the presence of defects. While fracture mechanics provides an adequate framework for describing structural resistance in the presence of large defects, structures are rarely designed with intentional cracks. Most defects, whether introduced during manufacturing or as a result of wear over the material's lifetime, are relatively small and fall within a transitional scale. At this length scale, neither stress-based analysis nor traditional fracture mechanics are fully applicable.

The manuscript explores the critical role of length scales in material failure, offering new insights into the mechanical behavior of solids across different scales. The primary objective is to bridge the gap between theoretical fracture models and practical applications through the use of advanced computational techniques such as phase-field methods and atomic-scale simulations. By integrating multi-scale modeling approaches with experimental analysis, the study focuses on understanding fracture processes in brittle materials.

The manuscript presents several key findings that advance the understanding of fracture mechanics and material behavior across multiple scales. It establishes correlations between fracture toughness and other material properties, such as tensile strength in various fracture modes. It also reveals that material length scales differ from the size of instabilities observed in complex geometries. Furthermore, the study shows that the limiting velocities of cracks in dynamic fractures are linked to the average stiffness around the crack tip, where the finite-sized, regularized stress zone helps align simulations with experimental observations. The research demonstrates how different length scales in atomic structures manifest in elasticity, plasticity, and fracture, providing new insights into material behavior. Additionally, the study introduces failure criteria inspired by atomic-scale processes in silicate glasses, which are crucial for accurately predicting both their fracture and ductile responses. The critical role of diffuse damage in differentiating between free surface energy and fracture surface energy is also emphasized. Finally, the study shows that periodic beam lattices possess a unique fracture toughness determined by their elementary structure and tensile strength, while establishing that Cosserat theory is both necessary and sufficient for optimizing the mechanical performance of these structures.

The implications of these findings are profound, offering new pathways for optimizing fracture-resistant materials. The research suggests that local toughness can be homogenized. By applying advanced optimization techniques, the global resistance of materials can be significantly enhanced, paving the way for the development of customized, fracture-resistant mechanical metamaterials tailored to specific applications.

Keywords: Regularization length, Toughness, Phase-field fracture, Atomic scale simulations, Silicate glass, Beam lattice

Le rôle des échelles de longueur dans la ruine des matériaux

Résumé: Les matériaux se comportent souvent de manière très différente à l'échelle microscopique par rapport à l'échelle macroscopique, particulièrement en ce qui concerne la ruine. À de petites échelles, les solides sont bien plus résistants que lorsqu'ils sont évalués à l'échelle structurelle. Cette différence est généralement attribuée à la présence de défauts. Si la mécanique de la rupture offre un cadre adéquat pour comprendre la résistance en présence de grands défauts, les structures ne sont presque jamais conçues volontairement avec des fissures. La plupart des défauts, qu'ils résultent de la fabrication ou de l'usure au fil du temps, sont relativement petits et se trouvent dans une échelle de longueur transitoire où ni l'analyse des contraintes ni la mécanique classique de la rupture ne s'appliquent pleinement.

Le manuscrit explore l'importance des échelles de longueur dans la ruine des matériaux et offre de nouvelles perspectives sur le comportement mécanique des solides. Il cherche à combler l'écart entre les modèles théoriques de rupture et leurs applications pratiques en s'appuyant sur des techniques de calcul avancées comme les méthodes de champ de phase et les simulations atomiques. L'approche intègre modélisation multi-échelles et analyses expérimentales pour mieux comprendre la rupture dans les matériaux fragiles.

Le manuscrit présente plusieurs résultats clés sur la mécanique de la rupture et le comportement des matériaux à différentes échelles. Il montre des corrélations entre la ténacité à la rupture et des propriétés telles que la résistance à la traction dans divers modes de fracture. Il révèle que les échelles de longueur des matériaux diffèrent des tailles d'instabilités observées dans des géométries complexes. De plus, il met en évidence que les vitesses limites des fissures dynamiques sont liées à la rigidité moyenne autour de la pointe de la fissure, où la zone de contrainte régularisée permet d'aligner simulations et observations expérimentales. La recherche montre également comment les échelles de longueur atomiques influencent l'élasticité, la plasticité et la rupture, offrant ainsi de nouvelles perspectives sur le comportement des matériaux. L'étude développe des critères de ruine basés sur les processus atomiques dans les verres de silicate, essentiels pour prévoir avec précision leurs comportements en rupture et en plasticité. Le rôle crucial des endommagements diffus dans la distinction entre l'énergie de surface libre et l'énergie de surface de rupture est également souligné. Enfin, l'étude démontre que les réseaux périodiques de poutres possèdent une ténacité unique, déterminée par leur structure élémentaire et leur résistance à la traction, et prouve que la théorie de Cosserat est à la fois nécessaire et suffisante pour optimiser les performances mécaniques de ces structures. Ces résultats offrent de nombreuses perspectives pour l'optimisation de matériaux résistants à la rupture. Ils suggèrent que la ténacité locale peut être homogénéisée. Grâce à des techniques avancées d'optimisation, la résistance globale des matériaux peut être augmentée, permettant ainsi le développement de métamatériaux mécaniques sur mesure, adaptés à des applications spécifiques.

Mots-clés: Longueur de régularisation, Ténacité, Rupture par champ de phase, Simulations atomiques, Verre de silicate, Treillis de poutres
